SEARCH FOR NEW CATHODE COMPOSITIONS FOR MILDLY ACIDIC Zn-MnO_2 BATTERIES

A THESIS SUBMITTED TO
THE GRADUATE SCHOOL OF NATURAL AND APPLIED SCIENCES
OF
MIDDLE EAST TECHNICAL UNIVERSITY

BY

YİĞİT AKBAŞ

IN PARTIAL FULFILLMENT OF THE REQUIREMENTS
FOR
THE DEGREE OF MASTER OF SCIENCE
IN
METALLURGICAL AND MATERIALS ENGINEERING

March 2022

Approval of the thesis:

SEARCH FOR NEW CATHODE COMPOSITIONS FOR MILDLY ACIDIC Zn-MnO$_2$ BATTERIES

submitted by **YİĞİT AKBAŞ** in partial fulfillment of the requirements for the degree of **Master of Science** in **Metallurgical and Materials Engineering, Middle East Technical University** by,

Prof. Dr. Halil Kalıpçılar
Dean, Graduate School of **Natural and Applied Sciences**

Prof. Dr. C. Hakan Gür
Head of the Department, **Met. And Mat. Eng., METU**

Prof. Dr. Y. Eren Kalay
Supervisor, **Met. And Mat. Eng., METU**

Prof. Dr. Tayfur Öztürk
Co-Supervisor, **Met. And Mat. Eng., METU**

Examining Committee Members:

Prof. Dr. Kadri Aydınol
Metallurgical and Materials Eng., METU

Prof. Dr. Y. Eren Kalay
Metallurgical and Materials Eng., METU

Prof. Dr. Tayfur Öztürk
Metallurgical and Materials Eng., METU

Prof. Dr. Şaban Patat
Chemistry, ERU

Assist. Prof. Dr. Çiğdem Toparlı
Metallurgical and Materials Eng., METU

Date: 25.03.2022

I hereby declare that all information in this document has been obtained and presented in accordance with academic rules and ethical conduct. I also declare that, as required by these rules and conduct, I have fully cited and referenced all material and results that are not original to this work.

Name Last name : Yiğit Akbaş

Signature :

ABSTRACT

SEARCH FOR NEW CATHODE COMPOSITIONS FOR MILDLY ACIDIC Zn-MnO$_2$ BATTERIES

Akbaş, Yiğit
Master of Science, Metallurgical and Materials Engineering
Supervisor: Prof. Dr. Y. Eren Kalay
Co-Supervisor: Prof. Dr. Tayfur Öztürk

March 2022, 128 pages

This thesis focuses on finding a new MnO$_2$-based cathode composition(s) for Zn-ion batteries. For this purpose combinatorial approach was employed using thick film cathodes deposited via magnetron sputtering. The system under study was MnO$_2$ alloyed with NaMnO$_2$, Bi$_2$O$_3$, NiO. For this purpose, four sputter targets were prepared. MnO$_2$ target was in 3-inch diameter placed in the central position and the other oxides were 2-inch in diameter placed 120° to one another forming a triangle. Substrates were 12.7 mm in diameter placed in a substrate magazine with a triangular geometry mimicking the targets underneath. A total of 36 cathode could be deposited in a single sputtering experiment each with a different composition.

A total of six experiments were carried yielding 216 cathodes. Cathodes were deposited on Ni foil used as a current collector. They were typically 3 μm thick with a mass varying from 0.23 to 2.38 mg. Cells used was of Swagelok type, anode was 300 μm thick Zn foil electrolyte was 2M ZnSO$_4$ + 0.1 M MnSO$_4$ aqueous solution.

The preliminary results indicated favorable results in Mn rich cathodes. As a result, out of six sets three set of cathodes were selected for detailed study.

Cyclic voltammetry as well as galvanostatic tests were carried for each cathode. Mn rich corner of the Bi-Mn-Ni ternary diagram where Na varied from 11 to 78% were mapped in terms of capacities, cyclic stability, and discharge plateau potential. Based on maps, three candidate compositions were selected with discharge capacities above 400 mAh/g. These are $Bi_{0.04}Na_{0.55}Ni_{0.04}Mn_{0.36}O_x$, $Bi_{0.04}Na_{0.37}Ni_{0.06}Mn_{0.53}O_x$ and $Bi_{0.02}Na_{0.63}Ni_{0.02}Mn_{0.33}O_x$. Further work is needed to check the full potential of the selected cathodes.

Keywords: MnO_2 cathodes, Zinc-ion battery, Combinatorial deposition, Magnetron sputtering

ÖZ

HAFİF ASİDİK Zn-MnO_2 PİLLER İÇİN YENİ KATOT BİLEŞİMLERİNİN ARAŞTIRILMASI

Akbaş, Yiğit
Yüksek Lisans, Metalurji ve Malzeme Mühendisliği
Tez Yöneticisi: Prof. Dr. Y. Eren Kalay
Ortak Tez Yöneticisi: Prof. Dr. Tayfur Öztürk

Mart 2022, 128 sayfa

Bu tez, Zn-iyon piller için yeni bir MnO_2 bazlı katot bileşimleri bulmaya odaklanmaktadır. Bu amaçla magnetron sıçratma yoluyla biriktirilen kalın film katotları kullanılarak eşzamanlı üretim yaklaşımı kullanıldı. İncelenen sistem, $NaMnO_2$, Bi_2O_3, NiO ile alaşımlanmış MnO_2'dir. Bu amaçla dört sıçratma diski hazırlanmıştır. MnO_2 diski 3 inç çapında merkezi konuma yerleştirilmiş ve diğer oksitler 2 inç çapında ve birbirine 120°'lik açılarla üçgen oluşturacak şekilde yerleştirilmiştir. 12,7 mm çapındaki altlıklar, üçgen geometriye sahip bir altlık tutucu haznesine yerleştirilmiştir. Her biri farklı bir bileşime sahip tek bir sıçratma deneyinde toplam 36 katot biriktirilmiştir.

Altı deney yapılarak 216 katot elde edilmiştir. Katotlar, akım toplayıcı olarak kullanılan Ni folyo üzerine kaplanmıştır. Kaplamalar tipik olarak 0,23 ila 2,38 mg arasında değişen bir kütle ile 3 μm kalınlığındadır. Kullanılan hücreler Swagelok tipindedir. Anot olarak 300 μm kalınlığında Zn folyo ve elektrolit olarak 2M $ZnSO_4$ + 0.1 M $MnSO_4$ sulu çözeltisi kullanılmıştır.

Ön sonuçlara göre Mn bakımından zengin katotlar olumlu sonuçlar verdiği gözlemlenmiştir. Sonuç olarak, detaylı çalışma için altı setten üç set katot seçilmiştir.

Her katot için döngüsel voltametri ve galvanostatik testler gerçekleştirilmiştir. Na'nın %11 ila %78 arasında değiştiği Bi-Mn-Ni üçlü diyagramının Mn açısından zengin köşesi, kapasiteler, döngüsel kararlılık ve deşarj plato potansiyelleri açısından haritalanmıştır. Haritalara dayalı olarak, 400 mAh/g'ın üzerinde deşarj kapasitelerine sahip üç aday kompozisyon seçilmiştir. Bunlar $Bi_{0.04}Na_{0.55}Ni_{0.04}Mn_{0.36}O_x$, $Bi_{0.04}Na_{0.37}Ni_{0.06}Mn_{0.53}O_x$ ve $Bi_{0.02}Na_{0.63}Ni_{0.02}Mn_{0.33}O_x$’dir. Seçilen katotların tam potansiyelini kontrol etmek için daha fazla çalışmaya ihtiyaç duyulmaktadır.

Anahtar Kelimeler: MnO_2 katot, Çinko-iyon pil, Eşzamanlı üretimli çöktürme, Magnetron sıçratmalı çöktürme

Dedicated to a sustainable future on the planet Earth

ACKNOWLEDGMENTS

The author wishes to express his deepest gratitude to his supervisor Prof. Dr. Y. Eren Kalay and his co-supervisor Prof. Dr. Tayfur Öztürk for their guidance, advice, criticism, encouragements, and insight throughout the research.

The author would also like to thank lab-mates Havva Eda Aysal, Hilal Aybike Can, Necdet Özgür Darıcıoğlu, Ramin Babazadeh Dizaj, Aylin Elçi, Fahrettin Kılıç, and Mehmet Mert Köse for their suggestions, comments and having a great time together.

OriginLab assistance of Hilal Aybike Can is gratefully acknowledged.

The technical assistance of Necmi Avcı, Eren Şimşek, Nilüfer Özel and Serkan Yılmaz are gratefully acknowledged.

I am grateful to my parents Yavuz Akbaş and Hediye Akbaş and, my sister Zeynep Beyza Akbaş who support me in every second of my life.

This work is funded by Scientific and Technological Research Council of Turkey under grant number TUBİTAK 118M076.

I wish a sustainable future to my country Republic of Turkey.

TABLE OF CONTENTS

CHAPTERS

APPENDICES

LIST OF TABLES

TABLES

LIST OF FIGURES

FIGURES

CHAPTER 1

INTRODUCTION

Energy demand of the world has been increasing. Oil, coal, and natural gas have been the primary energy sources for decades. Fossil fuels have met the energy demands very well for long time. However, those energy sources are carbon-based fuels. This leads air pollution by carbon emission. To meet extreme energy demand by fossil fuels creates excessive carbon emission. Renewable energy sources are quite vital for the sustainable, clean, and environmentally friendly future. However, they are available for limited time during a day. For instance, solar energy can be stored only sun is available during the day. The energy must be stored while they are available to use later when energy is needed. Energy storage systems are important to store energy from renewable sources.

There are several types of energy storage systems. Magnetic storage systems have very low storage time between 1 and 60 seconds. Dams are the mechanic energy storage systems. They can store energy about 2700 MW. However, it requires an area that geographically available. Besides, this method is not suitable for mobile devices. Batteries are most suitable for both mobile and grid storage.

Manganese oxide has been widely used since the first batteries were invented. Structurally modified MnO_2 is a quite attractive material to make primary Zn-MnO_2 batteries not just rechargable but also improve the voltage profile. In addition, Mn and Zn are appealing materials with their abundancy and low cost. Zn/MnO_2 batteries will be a good fit for grid energy storage systems to make them widespread in use. For this aim, modifiying of MnO_2 cathode is quite vital.

In this study, MnO_2 cathodes were modified by doping agents. For this purpose, combinatorial approach with RF magnetron sputtering were used to find a new MnO_2

composition. Targets were home-made. They were prepared from several metal oxides. First, manganese oxide, nickel oxide and bismuth oxide powders were solid-state synthesized. Then, home-made sputter targets were shaped from those powders by sintering process. The synthesized pure powders were pelletized in deformable PTFE rings. Sintered were made at several different temperatures and durations to find the best sintering condition. Homogenous grain size distribution is important to have a stable deposition rate during sputtering. The optimum internal structure with good sintering manner was investigated by scanning electron microscopy. X-ray diffraction phase analysis is made for both precursor oxides and targets to investigate existing phases. Maud software is used for Rietveld quantitative analyses.

Home-made targets were in the RF magnetron sputter device with proper angles and substrate to target distance. Manganese oxide-based cathode materials were grown on nickel substrates as thick films (1000 to 3000 nm). Manganese based cathodes with several range of compositions were formed by altering wattage (rate) of the targets. Active material weight was kept over 0.5 mg by coating for 15 hours or more.

Batteries were assembled as as-sputtered cathodes, zinc anode, PP separator and Zn/Mn sulfate electrolyte. Electrochemical characterizations were performed for each composition. Cyclic voltammetry was used to identify both electrochemical reactions and voltage range. Capacity and cycling performance of the batteries were also investigated to define the high-performance cathode with the best electrochemically active composition.

CHAPTER 2

LITERATURE REVIEW

Development of sustainable energy has attracted considerable attention due to environmental concerns caused by fossil fuels. Thus, we have seen a rapid rise of renewable energy, namely solar and wind energy. However, renewable energy sources are intermittent in its nature and require storage. From this perspective, secondary batteries such as Li-ion, and similar are suitable as storage devices. Lithium-ion batteries have good cycle stability and high energy density, but they are quite expensive. In addition, the lack of lithium sources and safety problems limit their use especially for large scale storage applications.

Zn-MnO_2 are known for a long time as primary battery. An advantage of this battery is their low cost which is just a fraction of that of Li-ion batteries. Active materials Zn and MnO_2 are abundant and low cost, and they are environmentally friendly.

In 1968, Kang et al. [1] first showed reduction of MnO_2 to Mn (III) oxide and afterwards to Mn (II) oxide in KOH electrolyte with Zn anode. Mn (II) oxide rechargeable to an inactive phase of Mn (III) oxide. They also found that only MnOOH is reversible to MnO_2 while Mn_2O_3 is partially oxidases to MnO_2 back[1]. In 1981, Kordesch et al. [2] showed second step reaction that MnOOH to $Mn(OH)_2$ occurs at low voltage under 0.9 V. They also indicated second step reaction is irreversible and it is increased when KOH concentration is higher.

Zn has low cost, non-toxicity and theoretically is capable of yielding a capacity of 820 mAh/g and 5854 mAh/cm^3[3]. For cathode, MnO_2, the theoretical capacity of 308 mAh/g for one electron exchange which doubles the capacity if two electrons exchange were taking place.

Because of the attractive properties of Zn-MnO_2, recent effort has concentrated on ways of making Zn-MnO_2 rechargeable. There are two approaches in these efforts. One concentrates on the traditional battery, i.e., using alkaline electrolyte and try to make the battery rechargeable. The alternative approach makes use of mildly acidic electrolyte and try to impart rechargeability with as high capacity as possible. The current thesis adopts the second approach and tries to develop new cathode chemistries for mildly acidic Zn-MnO_2 batteries.

2.1 Zn/MnO_2 Batteries

Zn-MnO_2 batteries are still in mass production as primary batteries. Electrolytic manganese dioxide (EMD) which is γ-MnO_2 is the primary battery cathode active material, and the electrolyte is aqueous KOH. Reaction mechanisms of both anode and cathode are shown on Equations [1-3]. As shown on Equation 1, upon discharge MnO_2 is reduced to MnOOH involving 1 electron exchange.

Reactions in KOH aqueous electrolyte:

$2MnO_2 + 2H_2O + 2e^- \rightarrow 2MnOOH + 2OH^-$ Cathode Equation 1

$Zn + 2OH^- \rightarrow ZnO + H_2O + 2e^-$ Anode Equation 2

$Zn + 2MnO_2 + H_2O \rightarrow ZnO + 2MnOOH$ Overall Equation 3

If reduction continues to 2 electrons exchange, MnOOH is further reduced to spinel Mn_3O_4 phase as shown on Equation 4. This second reaction is not reversible and thus, hinders the rechargeability.

$3MnOOH + e^- \rightarrow Mn_3O_4 + OH + H_2O$ 2nd e Reaction Equation 4

A number of studies [4][5] were conducted in recent years to make the alkaline batteries rechargeable by modifying cathode[4]. Yadav et al. [4], improved rechargeability and reached 2 electrons exchange by making $Mn(OH)_2$ reversible with the addition of Cu^{2+} and Bi_2O_3. Hertzberg et al. [5] studied with alkaline electrolyte KOH and LiOH mixing. 1M KOH + 3M LiOH aqueous solution was the best electrolyte for Bi_2O_3 added β-MnO_2/Zn foil cell. LiOH addition prevents the formation of $ZnMn_2O_4$ phase.

Due to problems faced in alkaline batteries, in 1987, Shoji et al. [6] was the first who pointed out that Zn-MnO_2 batteries could be made rechargeable using mildly acidic electrolyte. Discharge capacity of the galvanic cell increases with increase in the concentration of $ZnSO_4$. Cell was made with γ-MnO_2 cathode. They found cell is rechargeable more than 30 times. When cell cycle between 0.9 V and 1.7 V, it showed 100% coulombic efficiency with average discharge voltage of about 1.3 V[6].

Xu et al. [7] were first time discovered Zn^{2+} ions move in the mildly acidic aqueous electrolyte Zn-MnO_2 battery and named it as zinc-ion battery due to Zn^{2+} ion move between electrodes.

According to Sun et al. [8] in mildly acidic conditions showed H^+ and Zn^{2+} co-insertion mechanism when mildly acidic electrolyte is used. XRD study showed H^+ insertion is the main reaction during discharge to 1.3 V, MnOOH phase forms, while discharging to 1.0 V results as $ZnMn_2O_4$ which shows the Zn insertion[8]. Reaction mechanisms of both anode and cathode in mildly acidic electrolyte are shown on Equations [5-8].

Reactions in mildly acidic aqueous electrolyte:

Cathode:

$2MnO_2 + 2H_2O + 2e^- \rightarrow 2MnOOH + 2OH^-$	Discharge At 1.3 V	Equation 5
$MnOOH + Zn^{2+} \rightarrow ZnMn_2O_4/Zn_xMnO_2$	Discharge At 1.0 V	Equation 6

Anode:

$Zn^{2+} + 2e^{-} \leftarrow\rightarrow Zn$ Main Reaction Equation 7

$Zn^{2+} + OH^{-} + SO_4^{2-} \leftarrow\rightarrow [Zn(OH)_2]_3ZnSO_4 \cdot 5H_2O$ Side Reaction at 1.0 V Equation 8

2.1.1 Anode

McLarnon et al. [9] reported that the fundamental problem of Zn electrode are shape change and the formation of undesired morphologies such as dendrites, filamentary growths and nodules. They addressed those problems due to high solubility of Zn in common electrolytes and rapid electrochemical kinetics of Zn. Shin et al. [10] explained the dendritic growth in alkaline electrolyte. The oxidized Zn^{2+} ions form $Zn(OH)_4^{2-}$-based phases due to the abundance of hydroxide ions around anode material. These zincate ions diffuse away from anode surface due to concentration gradient that yields loss of active material. In addition, zincate ions principate as ZnO when the local solubility limit of zincate is reached. Those precipitates yield as dendritic growth and/or passivation, damaging the rechargeability of batteries that operate in alkaline aqueous electrolytes.

Zn anodes are used in the form of either Zn powder or foil. In case powders, the electrodes are prepared as composite of Zn and ZnO using Teflon as binder [4]. An anode using a gelling agent (Carbopol 940) with Zn powder, Indium-Acetate and KOH solution was also reported [11]. Powder form of Zn is used for alkaline media, while in the case of mildly acidic media the anode was mostly Zn foil.

According to Shin et al. [10] in mildly acidic media, pH 4-6 window permits Zn^{2+} ions to remain in their ionized form. Using salts such as $ZnSO_4$ or $Zn(CF_3SO_3)_2$, reversible Zn plating/stripping becomes possible to certain extent. in this fashion, recharging the battery becomes much easier by means of ionization of zinc metal.

When pH is lowered, the increases the potential for hydrogen evaluation reaction, as predicted by the Nernst equation and the resulting Pourbaix diagram. This implies that low pH solutions are more sensitive to the hydrogen evolution reaction during a cathodic step[10].

As reported by Shin et al. [10] Zn is relatively stable in aqueous media, and the spontaneous formation of a solid electrolyte interface (SEI) layer is insignificant. They further stated that the absence of a SEI layer crates its own problems. SEI layer is a passivation layer that hinders unwanted side reactions. Further Zn is sensitive to some degree of the HER in aqueous media that consumes electrolyte solvent and corrodes the metal surface.

A number of attempts were made so as to improve the anode performance [12]-[13]. They can be categorized as (i) electrolyte formulation[12], (ii) electrode modification [14]-[15], and (iii) host development[13]. For electrolyte formulation, Zhang et al. [12] have used a number of mildly acidic electrolytes using $ZnCl_2$, $Zn(NO_3)_2$, $ZnSO_4$, or $Zn(CF_3SO_3)_2$. They found that reversible reactions were possible sulfate-based and zinc triflate-based electrolytes, while nitrate-based and chloride-based electrolytes were unsuitable for reversible deposition/dissolution mechanism. They also found that 3M Zn-triflate electrolyte exhibited high stability. However, Zn-triflate salt was not enough on its own to meet the expectations in terms of performance and cycle life. In addition, its high cost compared to $ZnSO_4$ was detrimental as a choice[10].

In electrode modification, Li et al. [14] used carbon-zinc composites in place of Zn powder. Unmodified Zn anode were made up of Zn powder, acetylene-black and PVDF binder in weight ratio of 7:2:1, while modified Zn anode were prepared mixing Zn powder with activated carbon plus acetylene-black and PVDF binder in weight ratio of 5.8:1.2:2:1. Both modified and unmodified electrodes delivered initial capacity of 170 mAh/g (MnO_2). With unmodified Zn anode the capacity was reduced to 100 mAh/g after 60th cycle, while that of modified anode was significantly higher at 150 mAh/g. Li et al assigned this improvement to the suppression of the zinc hydroxide sulfate ($Zn_4SO_4(OH)_6.nH_2O$) (ZHS) formation brought about by activated carbon, which was an inactive phase. They further showed with XRD study that showed, deposition of zinc hydroxide sulfate preferentially occurs in the pores of activated carbon rather than on the surface of Zn particles.

Number of studies were conducted to coat Zn anode so as to improve its performance. Kang et al. [16] have tape casted nano-$CaCO_3$ slurry on Zn foil with PVDF binder as surface layer. The electrolyte was 3M $ZnSO_4$+0.1M $MnSO_4$ aqueous solution and the cathode was MnO_2. They reported a discharge capacity of 200 mAh/g after 1000 cycles which was better than the bare Zn anode which delivered an initial discharge capacity of 175 mAh/g but faded to 100 mAh/g after 1000 cycles.

Zhao et al. [17] used atomic layer deposition to apply ultra-thin (8 nm) amorphous TiO_2 coating on Zn anode. They found that the cell with pristine Zn delivered capacity around 75 mAh/g (MnO_2) for 350 cycles, while the cell with modified Zn delivered 150 mAh/g capacity for 1000 cycles. They explained that the coating suppresses the gas evolution, corrosion process and enhance the Zn^{2+} ion transportation. The electrolyte was 3M $Zn(SO_3CF_3)_2$ aqueous solution and MnO_2 were used as the cathode. Xie et al. [15] applied 3D-nanoporous ZnO coating on Zn foil. The coating accelerated the kinetic of Zn^{2+} ion rather than the hydrated zinc. Modified anode had a capacity of 212 mAh/g (MnO_2) and showed no capacity fading after 500 cycles at 500 mA/g.

Cui et al. [18] ion beam sputtered gold nanoparticles on Zn foil. The electrolyte was 3M $ZnSO_4$ aqueous solution. Cells with both bare Zn and gold coated delivered initial capacity of 200 mAh/g (MnO_2). However, cell with bare Zn failed after 500 cycles, while gold coated kept working over 2000 cycles. The improvement was explained based on gold nanoparticles acting as nucleation sides for ZHS-based phase.

Zhao et al. [19] studied polyamide coating on Zn anode. The electrolyte was 2M $ZnSO_4$ + 0.1M $MnSO_4$ aqueous solution. Cells with both bare Zn and polyamide coated delivered initial capacity of 175 mAh/g (MnO_2). However, cell with bare Zn had rapid capacity fading through 200 cycles, while polyamide coated kept capacity over 150 mAh/g for 1000 cycles.

Thus, it can be concluded that the coatings work as a protective layer on the Zn anode surface that prevents side reactions and dendritic growths.

In host development, the active material is loaded in a host. Li et al. [13] compared Cu foil, Cu foam or Ni foam as host material. Zn were electrodeposited on the host material. They assembled cells with β-MnO_2 cathode and 2M $ZnSO_4$ + 0.1M $MnSO_4$ aqueous electrolyte. Cell with Cu foam had a capacity of 206 mAh/g (MnO_2) showed the best cyclic stability after 500 cycles at 1000 mA/g. This is followed by Cu foil where the capacity faded to 100 mAh/g at 500th cycle. These compared with zinc flake anode where the fade in capacity was 50 mAh/g at 500th cycle. Ni foam anode was even worse than Zn flake in that it was subject to capacity fading down to 50 mAh/g at 300th cycle. The main advantage of using host is that it offers higher capacity and coulombic efficiency due to modification of surface area or physicochemical alteration of the pre-existing surfaces.

2.1.2 Electrolyte

For Zn-MnO_2 batteries, alkaline, mildly acidic, and non-aqueous ionic liquids are the main electrolytes that have been investigated. For alkaline electrolyte, KOH, LiOH and NaOH are commonly used. However, the use KOH common electrolyte for primary Zn-MnO_2 battery is quite problematic in the case of rechargeable Zn-MnO_2[20][21].

Hertzberg et al. [5] studied LiOH addition to KOH electrolyte. They found that 1M KOH + 3M LiOH aqueous solution was the best electrolyte. The cathode was Bi_2O_3 modified β-MnO_2 while anode was Zn foil. Battery delivered almost double specific capacity at C/3 rate compared to other mixing ratios. Capacity remained over 100 mAh/g at C/3 for 60 cycles. Hertzberg et al. claimed that LiOH addition prevented the formation of $ZnMn_2O_4$ phase.

Yuan et al. [22] studied 6M NaOH alkaline electrolyte where the cathode was $Na_{0.44}MnO_2$ and the anode was Zn foil. Cells were cycled between 1.1 V and 1.95 V which delivered a capacity of 79 mAh/g. When the same cell was cycled between 0.3 V and 1.95 V, the capacity was 345 mAh/g. $Na_{0.559}MnO_2$ had a phase transition below 1.1V to $Mn(OH)_2$ which was not reversible for this case and causes severe capacity fading.

Pan et al. [20] compared $ZnSO_4$+$MnSO_4$ aqueous electrolytes with that of KOH. $ZnSO_4$+$MnSO_4$ electrolyte had a better performance, lower polarization and stable behavior compared to KOH electrolyte. In this study, they found that Zn anode in KOH permanently transformed to ZnO after few cycles. In contrast, Zn in mildly acidic $ZnSO_4$ electrolyte survived over 400 hours without oxidation.

Pan et al. [20] stated that the addition of $MnSO_4$ helps prevent or minimize the dissolution of cathode active material MnO_2 during discharge. Chamoun et al. [23] reports that 0.1M $MnSO_4$ addition decreases the capacity decay quite significantly. Zhang et al. [24] tested $ZnSO_4$+$MnSO_4$ electrolytes in different mixing ratios. 2M $ZnSO_4$ + 0.1M $MnSO_4$ solution gives the better electrochemical behavior compared to other mixtures. There are more papers related with these electrolyte compositions. Huang et al. used $MnSO_4$ addition up to 0.5M with 2M $ZnSO_4$ [25]. They discovered that ZHS is also disappeared when reacts with the Mn^+ ions in electrolyte to form a new reversible phase $ZnMn_3O_7$.

Zhang et al. [21] compared a number of electrolytes in a cell where cathode was pyrolusite β-MnO_2 and the anode was Zn foil operated between 0.8 V and 1.9 V. The electrolytes were 45% KOH, 3M $ZnSO_4$, 3M $Zn(CF_3SO_3)_2$ and 3M $Zn(CF_3SO_3)_2$-0.1M $Mn(CF_3SO_3)_2$ aqueous electrolytes. Battery with KOH has severe capacity fading to 100 mAh/g after few cycles, meanwhile $ZnSO_4$ and $Zn(CF_3SO_3)_2$ faded down to 100 mAh/g after 60 cycles. The performance showed significant improvement with 3M $Zn(CF_3SO_3)_2$ - 0.1M $Mn(CF_3SO_3)_2$ where the capacity remained over 200 mAh/g for 100 cycles at 0.65C.

Table 2.1 Summary of capacities of Zn-MnO_2 cell with hybrid electrolyte

Cathode	**Electrolyte**	**Capacity (mAh/g)**	**Voltage Range (V)**	**Ref.**
α-MnO_2	Hybrid 1M NaOH and 0.01M $Zn(AC)_2$ 2M $ZnSO_4$ + 0.1M $MnSO_4$	282 @200	1.4-2.2	Fan et al. [26]
Electrodeposited ε-MnO_2	**Anode:** 6M KOH, 0.2M ZnO and 5mM vanillin solutions **Cathode:** 2.5M H_2SO_4 and 0.5M $MnSO_4$	600 @100	1-3	Zhong et al. [27]
Electrodeposited ε-MnO_2	**Anode:** 6M KOH, 0.2M ZnO and 5mM vanillin solutions **Cathode:** 2.5M H_2SO_4 and 0.5M $MnSO_4$	600 @1000	1-3	Zhong et al. [27]

Fan et al [26] used a hybrid electrolyte using a nafion membrane where the electrolyte was 1M NaOH and 0.01M $Zn(AC)_2$) for the anode and -mild (2M $ZnSO_4$ + 0.1M $MnSO_4$ for cathode . Cathode was α-MnO_2. The battery was cycled between 1.4 V and 2.2 V with an average discharge voltage of 1.7 V. The cell delivered an initial discharge capacity of 282 mAh/g at 200 mA/g which increased to 428 mAh/g after 80 cycles.

Zhong et al. [27] have used a decoupled electrolyte comprising three chambers. The chamber was for anode (Zn foil) with alkaline electrolyte made up of KOH, ZnO and vanillin solutions. The chamber for cathode was acidic with H_2SO_4 and $MnSO_4$ electrolyte. In-between the two chambers were K_2SO_4 electrolyte with selective ion membranes. The battery exhibits an open-circuit voltage of 2.83 V (the conventional Zn-MnO_2 batteries deliver 1.5 V). The capacity was 600 mAh/g.

Han et al. [28] studied non-aqueous acetonitrile-$Zn(TFSI)_2$ in δ-MnO_2/Zn foil cell. Cell delivered a capacity of 123 mAh/g at C/10 for 125 cycles. They showed that 0.2 mol of Zn^{2+} ions inserted per one mole of MnO_2 during discharge. Contact loss of active material, electrolyte decomposition and Mn dissolution were the main reason of capacity fading.

2.1.3 Cathode

Manganese is a transition metal that has several stable oxide phases (MnO, Mn_3O_4, Mn_2O_3 and MnO_2) and crystallizes in a wide range of crystal structures and multivalent phases due to different valance states of Mn: Mn^{2+}, Mn^{3+}, Mn^{4+}, and Mn^{7+}[29]. Diverse Mn-based cathode materials have been investigated for rechargeable zinc-ion batteries. This include α-MnO_2, β-MnO_2, γ-MnO_2, Akhtenskite-type MnO_2, as well as Mn_2O_3, Mn_3O_4, $ZnMn_2O_4$, $NaxMnO_2$.

The most common structures in the manganese dioxide system are the rutile-type β phase, hollandite-type α, ramsdellite-type R, birnessite-type δ, spinel-type λ, and γ, which is an intergrowth of β and R with various fractions of β/R domains and twinning[30]. Most manganese oxide mineral structures are frame of MnO_6 octahedra which shares edges and/or corners in many combinations, giving rise to a large number of polymorphs[36]. Among them 14 crystal structures having nominal composition MnO_2, natural or synthetic, have been cited in the literature[37]. The realization of each of these polymorphs is dependent on the type of linkage between the fundamental octahedral units in the crystallographic structure. Pyrolusite, β-MnO_2 having single chains of edge-linked octahedra share corners with neighboring chains to form a framework structure containing tunnels with square cross section that are one octahedron by one octahedron (1 x 1). Pyrolusite crystallizes in the tetragonal crystal system and the c axis is parallel to the chain and the tunnel direction[38]. Ramsdellite is a metastable form of MnO_2. The crystal structure is built of double chains of MnO_6 octahedra. The double chains consist of two adjacent single chains that shares edges. They link corners with each other to form a framework having rectangular-shaped tunnels that are 1 x 2 octahedra on a side[39]. Further, an α-MnO_2 (hollandite) cathode possessing 2 × 2 tunnels (size ~ 4.6 Å), while todorokite-type MnO_2 has larger tunnels 3 × 3 (size ~ 7.0 Å), the low temperature γ-MnO_2 has randomly arranged intergrowth 1 × 1 (size ~2.3 × 2.3 Å, pyrolusite) and 1 × 2 (size ~2.3 × 4.6 Å, ramsdellite) tunnel blocks[40]. MnO_6 octahedra which shares edges gives rise to a layered δ-MnO_2. Crystal structures of manganese oxides are shown in Figure 2.1.

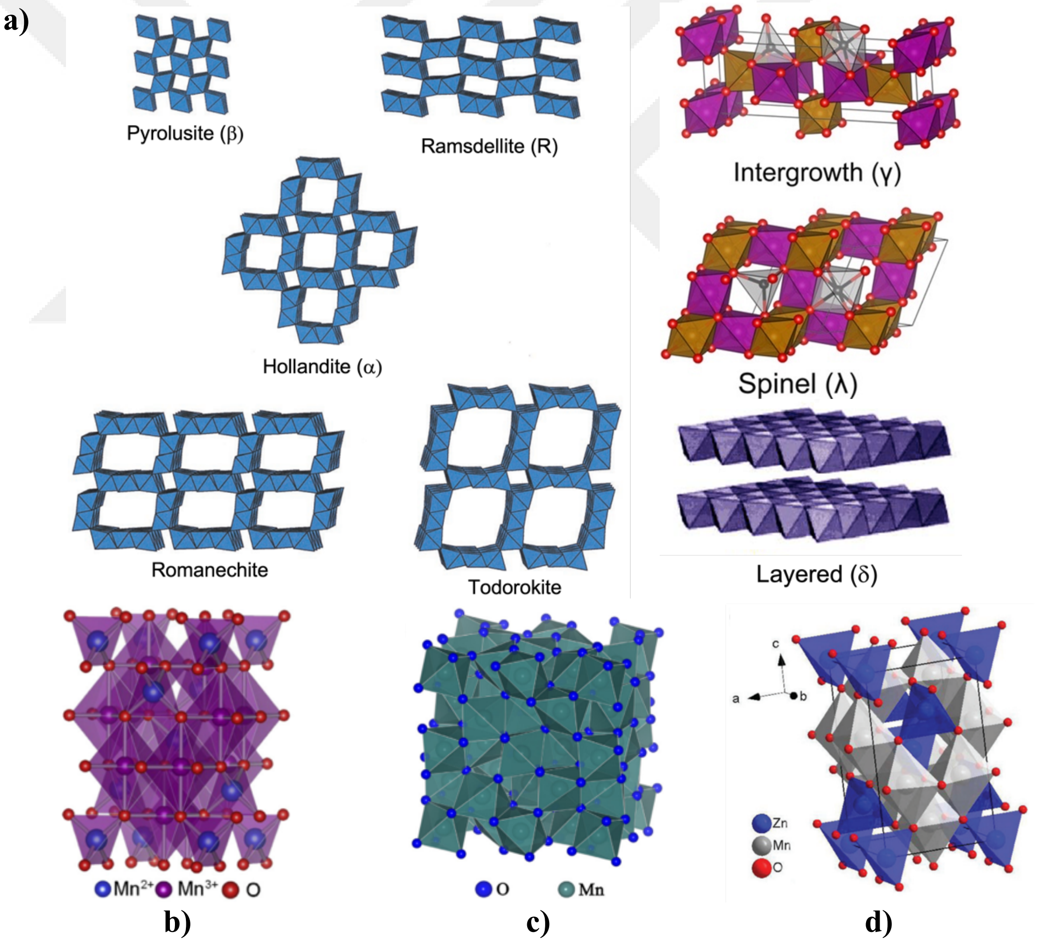

Figure 2.1 Crystal structures of **a)** MnO_2 polymorphs [30][31][32], **b)** tetragonal spinel-Mn_3O_4 [33], **c)** α-Mn_2O_3 [34], **d)** tetragonal spinel-$ZnMn_2O_4$ [35].

Table 2.2 Summary of capacities of α-MnO_2 cathodes with Zn foil anode

Cathode	**Electrolyte**	**Capacity (mAh/g)**	**Voltage Range (V)**	**Ref.**
α-MnO_2	1M $ZnSO_4$	210 @C/2 130 @6C	1-1.9	Xu et al. [7]
α-MnO_2 nanofiber	2M $ZnSO_4$ + 0.1M $MnSO_4$	285 @C/3 260 @C	1-1.8	Pan et al. [20]
α-MnO_2 nanorod CNT	2M $ZnSO_4$ + 0.1M $MnSO_4$	282 @C 100 @9C	0.85-1.9	Li et al. [41]
α-MnO_2 Fiber (+10% C)	2M $ZnSO_4$ + 0.2M $MnSO_4$	330 @500 mA/g	0.9-1.8	Gao et al. [42]
α-MnO_2 Fiber (+30% C)	2M $ZnSO_4$ + 0.2M $MnSO_4$	140 @500 mA/g	0.9-1.8	Gao et al. [42]

Studies making use of α-MnO_2 as cathode are collected in Table 2.2. Here the specific capacity ranges from 200 to 300 mAh/g (MnO_2). Xu et al. [7] used 1M $ZnSO_4$ electrolyte without additives and cycled the cell between 1.0 V and 1.9 V. The batteries delivered an initial capacity of 210 mAh/g at 0.5C which was reduced to 100 after 100 cycles.

Pan et al. [20] studied the effect of $MnSO_4$ addition to the electrolyte. The cathode was α-MnO_2 nanofiber which gave an initial capacity of 285 and 260 at C/3 and C respectively. The capacity at 5C was 161 mAh/g. The battery has yielded an impressive capacity retention of 92% after 5000 cycles. Authors attributed this to the beneficial effect of $MnSO_4$ addition to the electrolyte.

Gao et al. [42] used tetragonal α-MnO_2 fiber as cathode and so as to improve its conductivity they have added acetylene black from 10 up to 40 wt.%. The electrolyte was 2M $ZnSO_4$ + 0.2M $MnSO_4$. With 10% acetylene black, the battery delivers quite a high capacity, namely 330 mAh/g at 500 mA/g, but the performance was not stable as the capacity faded rapidly with cycling. In terms of cyclic stability 30% acetylene black was found to be the best where the capacity after 300 cycles was 140 mAh/g. They also showed that H^+ from the water is firstly inserted into α-MnO_2, resulting in the enrichment of OH^- and the formation of $[Zn(OH)_2]_3ZnSO_4 \cdot 5H_2O$. Then the Zn^{2+} is intercalated into α-MnO_2, resulting in the formation of $ZnMn_2O_4$. Zinc hydroxide sulfate (ZHS) were formed at 0.9 V during discharge.

Table 2.3 Summary of capacities of γ-MnO_2 cathodes with Zn foil anode

Cathode	Electrolyte	Capacity (mAh/g)	Voltage Range (V)	Ref.
γ-MnO_2	1M $ZnSO_4$	210 @C/2 130 @6C	1-1.9	Alfaruqi et al. [40]

γ-MnO_2 as cathode was investigated by Alfaruqi et al. [40]. The electrolyte was 1M $ZnSO_4$. The battery delivered an initial capacity of 285 mAh/g at 0.5 mA/cm^2. They showed via an in-stu XRD measurements that γ-MnO_2 undergoes phase transition during discharge and new phases form close to 1.0 V, i.e., γ-MnO_2 transforms to a spinel-type $ZnMn_2O_4$ and two new intermediary phases γ-Zn_xMnO_2 (tunnel-type), and layered Zn_yMnO_2 (layered- type). Parent γ-MnO_2 phase formed back when the battery charged to 1.8 V.

Table 2.4 Summary of capacities of β-MnO_2 cathodes with Zn foil anode

Cathode	Electrolyte	Capacity (mAh/g)	Voltage Range (V)	Ref.
β-MnO_2	2M $ZnSO_4$	~260 @200	1-1.9	Li et al. [43]
β-MnO_2	2M $ZnSO_4$ + 0.1M $MnSO_4$	~300 @200	1-1.9	Li et al. [43]
Commercial β-MnO_2	3M $ZnSO_4$ + 0.1M $MnSO_4$	200 @100 150 @500	0.8-1.8	Han et al. [44]
Oxygen defected β-MnO_2	3M $ZnSO_4$ + 0.1M $MnSO_4$	300 @100 200 @500	0.8-1.8	Han et al. [44]
β-MnO_2 nanorod	1M $ZnSO_4$ + 0.2M $MnSO_4$	275 @100 135 @200	1-1.8	Islam et al. [45]

Batteries making use of β-MnO_2 cathodes are reported in Table 2.4. Li et al. [43] used β-MnO_2 with 2M $ZnSO_4$ electrolyte. The initial capacity was close to 260 mAh/g at 200 mA/g which faded rapidly to below 50 mAh/g after 200 cycles. They explained that the fading occurs due to (i) the existence of the inert layer $Zn_4SO_4(OH)_6.H_2O$ and $ZnMn_2O_4$ hindering the electrochemical reaction, (ii) the dissolution of active material during discharge process leading to the capacity loss, (iii) release of gasses in the charging process resulting in poor contact and expansion of the battery. The battery performed significantly better with 2M $ZnSO_4$ + 0.1 M $MnSO_4$. The capacity increased with cycling to 400 mAh/g at 25th cycle and then then stabilizes to 300 mAh/g for 200 cycles. Lie et al further claimed that the addition of sodium trimetaphosphate (0.3 wt.%) to electrolyte hinders the formation of $Zn_4SO_4(OH)_6.H_2O$ and help, improve the cyclic stability.

Han et al. [44] examined oxygen defected β-MnO_2 as cathode. They reported an initial capacity of 302 mAh/g at 50 mA/g. The capacity at 500 mA/g was initially close to 200 mAh/g which was retained 94% after 300 cycles. These values compare with commercial β-MnO_2 where the capacity was 206 mAh/g at 50 mA/g with 78% capacity retention.

Table 2.5 Summary of capacities of δ-MnO_2 cathodes with Zn foil anode

Cathode	**Electrolyte**	**Capacity (mAh/g) Rate (mA/g)**	**Voltage Range (V)**	**Ref.**
nanoflake δ-MnO_2	1M $ZnSO_4$	4th cycle 252 @83 100th cycle 112 @83	1-1.8	Alfaruqi et al. [46]
nanosheet δ-MnO_2	1M $ZnSO_4$ + 0.1M $MnSO_4$	133 @100 86 @500	1-1.8	Guo et al. [47]
δ-MnO_2	2M $ZnSO_4$ + 0.2M $MnSO_4$	100 @100	1-1.8	Guo et al. [48]
Na intercalated δ-MnO_2	2M $ZnSO_4$ + 0.2M $MnSO_4$	278 @C 106 @20C	0.95-1.85	Wang et al. [49]
Hollow δ-MnO_2	1M $ZnSO_4$ + 0.2M $MnSO_4$	405 @C/2 305 @C	1-1.8	Guo et al. [50]

Batteries with δ-MnO_2 cathodes are reported in Table 2.5. Alfaruqi et al. [46] used δ-MnO_2 nanoflake cathode with 1M $ZnSO_4$ electrolyte. Cell delivered initial capacity of 112 mAh/g and reached 252 mAh/g at 4th cycle at 83 mA/g rate. The capacity then decreased down to 112 mAh/g at 100th cycle. During discharge they found that the layered δ-MnO_2 undergoes a structural transformation to spinel-type $ZnMn_2O_4$ with Mn(III) state and an intermediary Mn(II) phase of layered δ-Zn_xMnO_2.

Wang et al. [49] used δ-MnO_2 cathode pre-intercalated with Na and water molecules. The capacity was 278 mAh/g at 1C and 106 mAh/g at 20C. They reported an excellent capacity retention which was as high as 98% after 10000 cycles. This was attributed to smooth intercalation of Zn in the pre-intercalated layered structure. Guo et al. [48] compared unmodified δ-MnO_2 with β-MnO_2 and claim that β-MnO_2 electrode shows better cycling stability than δ-MnO_2, due to the stable 3D tunnel structure of the latter.

As seen in Table 2.5 highest capacity was obtained with a hollow δ-MnO_2 cathode [50] prepared with a special technique. The electrolyte was 1M $ZnSO_4$ + 0.2M $MnSO_4$. They reported a discharge capacity of 405 at C/2 and 305 at C. The cyclic stability of the battery was also quite acceptable preserving a capacity of ~300 mAh/g after 100 cycles.

Table 2.6 Summary of capacities of Mn_3O_4, Mn_2O_3 and $ZnMn_2O_4$ cathodes with Zn foil anode.

Cathode	**Electrolyte**	**Capacity (mAh/g)**	**Voltage Range (V)**	**Ref.**
Mn_3O_4	2M $ZnSO_4$	120 @500	0.9-1.9	Hao et al. [33]
Mn_3O_4	0.5M $Zn(CF_3SO_3)_2$	100@100	0.8-1.9	Stoševski et al. [34]
Mn_2O_3	2M $ZnSO_4$	148 @ 100	1-1.9	Jiang et al. [34]
Mesoporous Amorphous Manganese Oxide	2M $ZnSO_4$	225 @100 till 110th cycle 100 @100 after 200th cycle:	1-1.85	[51]
$ZnMn_2O_4$	1M $ZnSO_4$ + 0.1M $MnSO_4$	225 @100	1-1.8	[52]

Manganese oxides other than MnO_2 were also used as cathodes for the Zn batteries. Hao et al. [33] used Mn_3O_4 as cathode material for mildly acidic battery using 2M $ZnSO_4$ electrolyte. Mn_3O_4 transforms to Mn_5O_8 during charging and keeping the battery at 1.9 V converts Mn_5O_8 to Zn birnessite. The battery, cycled between 0.9 V and 1.9 V at 500 mA/g had an initial capacity of around 40 mAh/g increased up to

140 mAh/g till 50th cycle. The capacity was reduced to 120 mAh/g after 300 cycles. Stoševski et al. [53] in a similar study confirmed the phase transition of Mn_3O_4 to birnessite MnO_2. In addition, they found that for full activation of the battery with Mn_3O_4 50 cycles were required with $ZnSO_4$ electrolyte whereas with zinc triflate electrolyte 15 cycles were sufficient. Jiang et al. [34] used Mn_2O_3 cathode material, which also transformed to Zn birnessite.

Wu et al. [51] propose used amorphous manganese oxide as cathode . The battery delivered a capacity of 225 mAh/g till around 110th cycle, but thereafter the capacity was reduced to 100 mAh/g after 200 cycles. This was attributed to the formation of woodruffite phase ($ZnMn_3O_7{\cdot}2H_2O$) which hinders the reversibility. Soundharrajan et al. [52] used $ZnMn_2O_4$ microrods as cathode with 1M $ZnSO_4$ + 0.1M $MnSO_4$ electrolyte. The battery delivered 225 mAh/g at 100 mA/g for 200 cycles and the capacity retention was 80% after 1000 cycles.

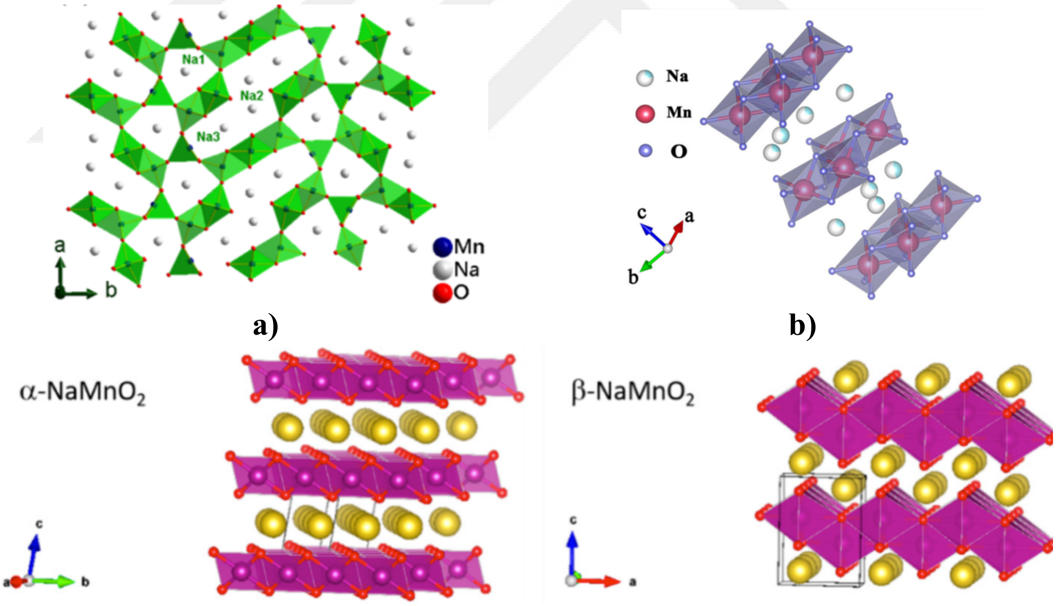

a) b)

c)

Figure 2.2 Crystal structure of Na_xMnO_y **a)** orthorhombic $Na_{0.44}MnO_2$ [54], **b)** hexagonal $Na_{0.7}MnO_{2.05}$ [55], **c)** monoclinic α-$NaMnO_2$ and orthorhombic β-MnO_2 [56].

Sauvage et al. [57] revealed that $Na_{0.44}MnO_2$, which is isostructural with $Na_4Mn_4Ti_5O_{18}$, crystallizes in an orthorhombic lattice cell (*Pbam* space group). The manganese ions are located in two different environments: all Mn^{IV+} ions and half of the Mn^{III+} ions are in octahedral sites (MnO_6), while the other Mn^{III+} ions are gathered in a square-pyramidal environment (MnO_5). The latter forms edge-linked chains linked to two double and one triple octahedral chain by the vertices, leading to the formation of two types of tunnels. Crystal structure of sodium manganese oxides are shown in Figure 2.2. Sun et al. [55] described the $Na_{0.7}MnO_{2.05}$ shows a layered structure composed of corner-sharing and edge-sharing MnO_6 octahedra which each oxygen atom belongs to three manganese-oxygen octahedra, while the interlayer is filled by Na^+. Manzi et al. [56] reported that $NaMnO_2$ crystallize in two different layered structure: (a) the low temperature α-$NaMnO_2$ one stable between 600 and 850°C, and (b) the high temperature polymorph β-$NaMnO_2$ that is thermodynamically stable above 850°C. As seen on Figure 2.2, The α-$NaMnO_2$ crystallizes in a monoclinic system (C2/m space group) with cell parameters $a = 5.53 \pm 0.01$, $b = 2.860 \pm 0.004$, $c = 5.77 \pm 0.01$ Å, and $\beta = 112°$ [58]. This crystal structure is a classified O3 type: sodium ions occupy octahedral sites and share edges between the MnO_6 octahedra, whereas Mn^{3+} ions are six-coordinated by oxygen atoms on planar triads with a stacking AB CA BC [59]. The β-$NaMnO_2$ crystallizes in an orthorhombic system with the space group Pmmn and cell parameters $a = 4.77 \pm 0.01$, $b = 2.852 \pm 0.003$, and $c = 6.31 \pm 0.02$ Å. In this structure, the MnO_6 sheets buckle forming a peculiar packed layered structure where sodium ions are hexa-coordinated in the zig-zag interlayers [58].

Table 2.7 Summary of capacities of Na_xMnO_y cathodes with Zn foil anode

Cathode	**Electrolyte**	**Capacity (mAh/g) Rate (mA/g)**	**Voltage Range (V)**	**Ref.**
$Na_{0.44}MnO_2$	0.5M $ZnSO_4$ + 1M Na_2SO_4	114 @4C	0.5-2	Wu et al. [60]
$Na_4Mn_9O_{18}$ CNT	0.5M $ZnSO_4$ + 1M Na_2SO_4	53 @4C	1-1.85	Yin et al. [61]
$Na_{0.44}MnO_2$	6M NaOH	345 @C/2 79 @C/2	0.3-1.95 and 1.1-1.95	Yuan et al. [22]
$Na_{0.55}Mn_2O_4$ and $Na_{0.7}MnO_{2.05}$	3M $n(CF_3SO_3)_2$	250 @100 150 @500	0.95-1.85	Wang et al. [62]

There are also number of sodium bearing manganese oxide compounds used as cathodes. These are tabulated in Table 2.8. Wu et al. [60] studied $Na_{0.44}MnO_2$ as cathode using 0.5M $ZnSO_4$ + 1M Na_2SO_4 as electrolyte. Cell delivered initial discharge capacity of 114 mAh/g at 4C, cycled between 0.5 V and 2.0 V. however rapid capacity fading occurs with cycling. Yuan et al. [22] studied 6M NaOH alkaline electrolyte with $Na_{0.44}MnO_2$/Zn foil cell. Cells were cycled between both 1.1-1.95 V and 0.3-1.95 V, and they delivered initial capacities of 79 mAh/g and 345 mAh/g, respectively. $Na_{0.559}MnO_2$ below 1.1 V transforms to $Mn(OH)_2$ which is not reversible and causes severe capacity fading. Thus, upon cycling between 0.35 to 1.95 V, the capacity reduced to 30 mAh/g after 4 cycles. However, between 1.1 V and 1.95 V, there was no capacity fading and the cell delivered 79 mAh/g at C/2 for 50 cycles.

Wang et al. [62] used $Na_{0.55}Mn_2O_4$ and $Na_{0.7}MnO_{2.05}$ as a mixture for cathode. The electrolyte was 3M $n(CF_3SO_3)_2$. The cell delivered a discharge capacity of 250 mAh/g at 100 mA/g. The cell tested at 1A/g had a capacity of 80 mAh/g an excellent cycling stability with a capacity retention of 83% after 800 cycles.

Number of compounds were used as additive during cathode preparation. Yu [63] claimed that incorporation of Bi into MnO_2 was beneficial during the synthesis. Yu further explained that Bi^{3+} ions are much larger than Mn^{2+} and Mn^{3+} which as a result prevents spinel Mn_3O_4 formation. Minakshi et al. [64] made a various levels of TiS_2 and Bi_2O_3 addition to γ-MnO_2 for an alkaline battery using LiOH electrolyte so as to prevent Mn_3O_4 formation. A mixture of Bi_2O_3 (3%) + TiS_2 (2%) was the best in terms of performance followed by Bi_2O_3 (5%), TiS_2 (5%), and the plain γ-MnO_2. Yadav et al. [4] investigated Cu addition during the synthesis of layered δ-MnO_2. Bi_2O_3 addition was made to the cathode slurry. The electrolyte was KOH (25 wt.%), the battery cycled. They report a capacity of 607 mAh/g for 90 cycles. They claim that Cu stabilizes the layered (birnessite) structure while the Bi_2O_3 prevents the formation of irreversible phase of Mn_3O_4. Ni and Co doping are investigated by Biswal et al. in Zn/MnO_2 battery [65]. With Co doped 2 wt.%, a capacity of 670 mAh/g was reported. With Ni doped 1 wt.% the initial capacity was 395 mAh/g. According to Sokolowski et al. [66] different dopants stabilize different MnO_2 polymorphs; Co^{2+} and Fe^{2+} stabilize γ-MnO_2, Cr^{3+} stabilizes layered δ-MnO_2 (birnessite).

To summarize, manganese oxides generally suffer from two major problems when used as the cathode materials for aqueous rechargeable zinc-ion batteries: 1) Phase transitions taking place during cycling leading to the formation of irreversible phases. 2) Mn dissolution into electrolyte affecting the chemistry of the cathode.

CHAPTER 3

PREPARATION OF SPUTTER TARGET FOR THICK FILM CATHODE DEPOSITION

In this chapter details with preparing to active material synthesis are given which are used in sputter target preparation. This involves the preparation of fine oxide powders which are then pressed and sintered to obtain sputter targets in 2-inch diameter.

3.1 Materials and Methods

3.1.1 Synthesis of metal oxide powders

Precursors used in active material synthesis were Mn, Bi and Ni nitrates. Pure oxides were synthesized via a calcination treatment. All calcination were carried out in a muffle furnace with a heating rate of 10°C/min. Where complex oxides were synthesized e.g., $Na_{0.7}MnO_2$. The precursors were mixed in stoichiometric proportions and then subjected to calcination treatment. Oxides and carbonates when processed were dried in a furnace at 100°C before they were ball milled. The ball milling was carried out with Retsch PM 400 Ma-Type at 120 rpm for 4 hours.

3.1.2 Preparation of sputter targets

A few drops of water were added to powders and mixed thoroughly before compaction (6 g powder 0.4 cc DI water). The compaction was carried out using a deformable die [67] made up of PTFE ring typically 65 mm inside diameter , 5 mm wall thickness, 5 mm high. The powders were filled into the ring and compacted under 100 MPa pressure. Green body was then removed from the ring and placed in a muffle furnace for sintering. Heating rate was 10°C/min Following sintering, the resulting disc which was slightly larger than 50 mm was grinded so as to reduce its diameter to 50 mm. MnO_2 target which was 3-inch in diameter were procured from Changsha Xinkang Advanced Materials Co., Ltd.

3.1.3 Structural Characterization

Phase analysis of synthesized powders and targets were investigated by Rigaku DMAX2200 or Bruker D8 Advance X-ray diffractometer. 20 mm pellets were used to investigate phase and microstructure after sintering process. Rigaku and Bruker X-ray diffractometer were used with Cu-K_α radiation (λ=1.5406Å) at 30 kV acceleration and 40 mA current. Diffraction patterns were scanned between 5° and 85° with scan speed of 1°/min and step size of 0.02°. Where necessary, the X-ray diffraction pattern were refined by Rietveld refinement technique using Maud software [68].

FEI Nova NanoSEM scanning electron microscopy (SEM) with SE and EDS detector were used to investigate microstructure. SE detector was used for imaging with 20 kV acceleration voltage. 30 kV acceleration voltage were used for EDS analysis.

3.2 Results and Discussions

3.2.1 $NaMnO_2$

So as to synthesize $NaMnO_2$, first Mn_2O_3 powder was synthesized. For this purpose manganese (II) nitrate tetrahydrate ($Mn(NO_3)_2.4H_2O$, Merck 98.5%) was calcined at various temperatures, 285°C, 325°C, 400°C, 450°C ve 600°C, in air. XRD pastern of calcined powders are given in Figure 3.1. As seen in the pattern MnO_2 phase co-exist with Mn_2O_3. When calcined at 600°C for a duration of 5 hours, the resulting powder was Mn_2O_3.

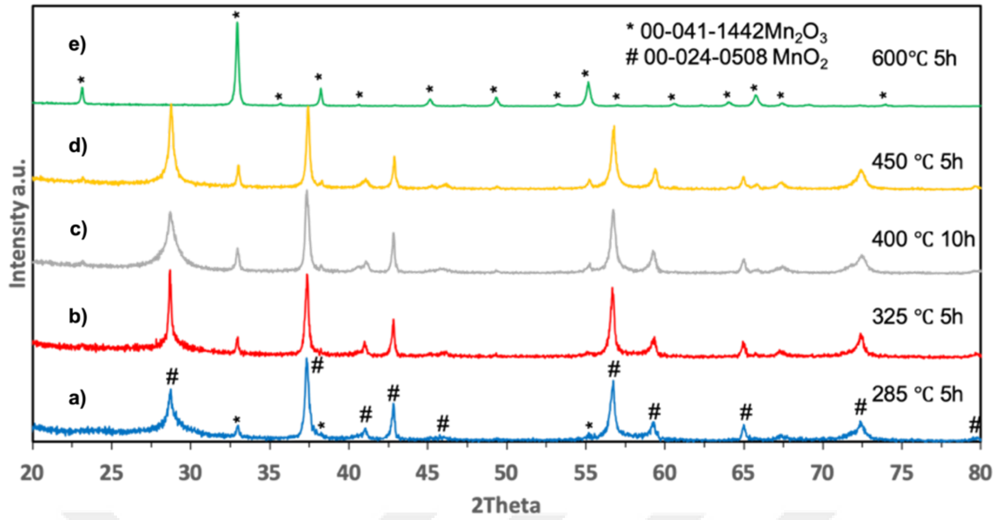

Figure 3.1 XRD pattern of calcined manganese nitrate at different temperatures **a)** 285°C, **b)** 325°C, **c)** 400 °C, **d)** 450 °C, **e)** 600°C

So as to synthesize $NaMnO_2$, Mn_2O_3 synthesized at 600°C for 5 hours are mixed with stoichiometric proportion of Na_2CO_3 (99.9% Merck) and ball milled for 4 hours. The mixture was then calcined at 850°C and 950°C for 9, 12 and 15 hours. XRD pattern of the powders synthesized at 850°C are given in Figure 3.2. It is seen that α-$NaMnO_2$ is the dominant phase after 9 hours calcination. As the duration is increased the relative proportion of β-$Na_{0.7}MnO_2$ increases. There are also minor phases as shown in Figure 3.2.

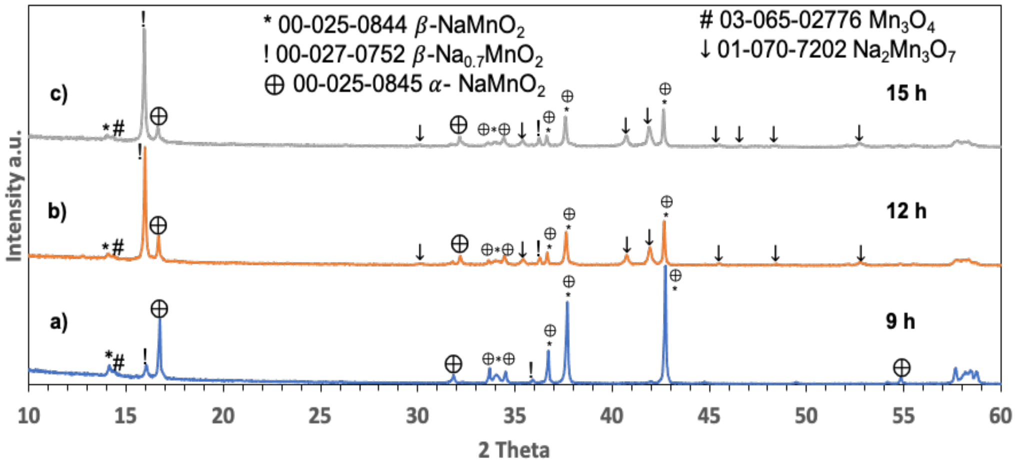

Figure 3.2 XRD pattern of powder synthesis of $NaMnO_2$ at 850°C for **a)** 9h, **b)** 12h, **c)** 15h.

In Figure 3.3, phases in the case of calcination at 950℃ are similar. After 9 hours of calcination, the relative amount of phases α-$NaMnO_2$ and β-$NaMnO_2$ were similar. With prolonged sintering β-$NaMnO_2$ transforms to β-$Na_{0.7}MnO_2$ and its fraction increases. So as to obtain β-$NaMnO_2$ instead of β-$Na_{0.7}MnO_2$ the experiment was repeated with excess Na_2CO_3. The patterns are given in Figure 3.4. It is seen that with 10% excess Na_2CO_3, the synthesized powder is made up of α-$NaMnO_2$ with some minor phases.

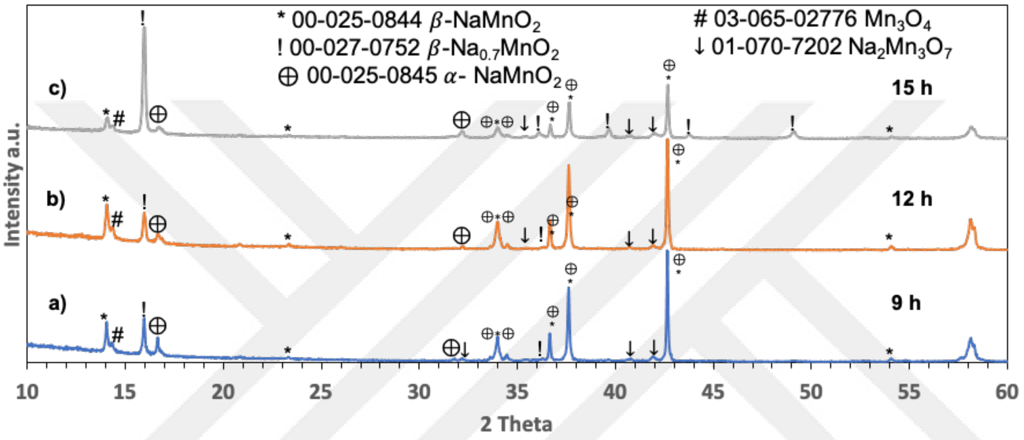

Figure 3.3 XRD pattern of powder synthesis of $NaMnO_2$ at 950°C for **a)** 9h, **b)** 12h, **c)** 15h

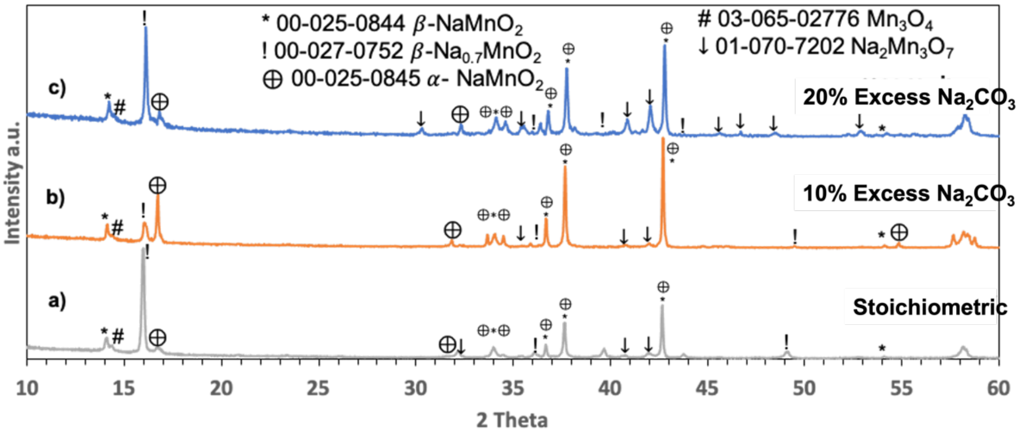

Figure 3.4 XRD pattern of powder synthesis of $NaMnO_2$ at 950°C **a)** stochiometric, **b)** 10% excess Na_2CO_3, **c)** 20% excess Na_2CO_3

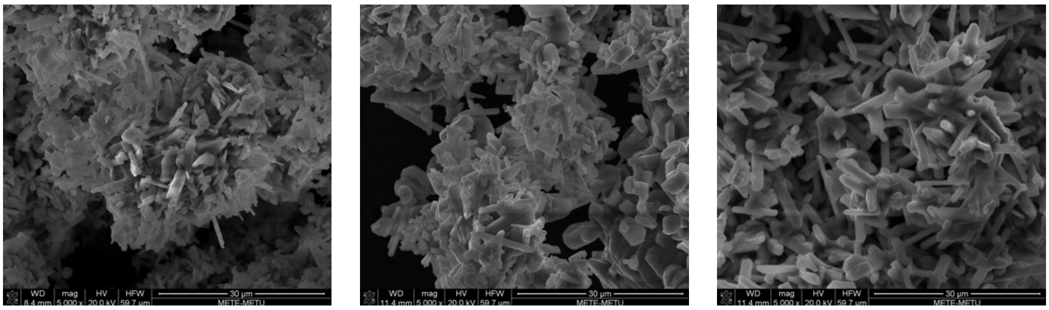

a) **b)** **c)**

Figure 3.5 SEM images of as-synthesized powders for 15 hours at **a)** 850°C, **b)** 950°C **c)** 950°C with 10% excess Na_2CO_3

Representative SEM images recorded from synthesized powders are given in Figure 3.5. It is seen that the powders are needle like and morphologically are all similar to one another. EDS analysis taken from Figure 3.5 (c) which refers to the sample with 10% Na_2CO_3 addition yield Na:Mn = 0.48:0.52 which is quite close to α-$NaMnO_2$ powder.

Powders with 10% Na_2CO_3 addition was synthesized at 950°C for 15 hours. A total of 10 gram of α-$NaMnO_2$ was synthesized. They were pressed to 20 mm diameter disc and sintered at 1350°C at 5, 10, 15 hours. XRD pattern of the resulting pellet are given in Figure 3.6. It is seen that after 5 hours of sintering there are two phases in the pellet; α-$NaMnO_2$ which was the starting phase of the powders and β-$NaMnO_2$ plus β-$Na_{0.7}MnO_2$. With prolonged sintering the latter phase becomes more dominant such that after 15 hours of sintering the pellet was totally made of β-$Na_{0.7}MnO_2$. SEM image of the sintered pellet is given in Figure 3.7 (a). It is seen that the structure is fully dense.

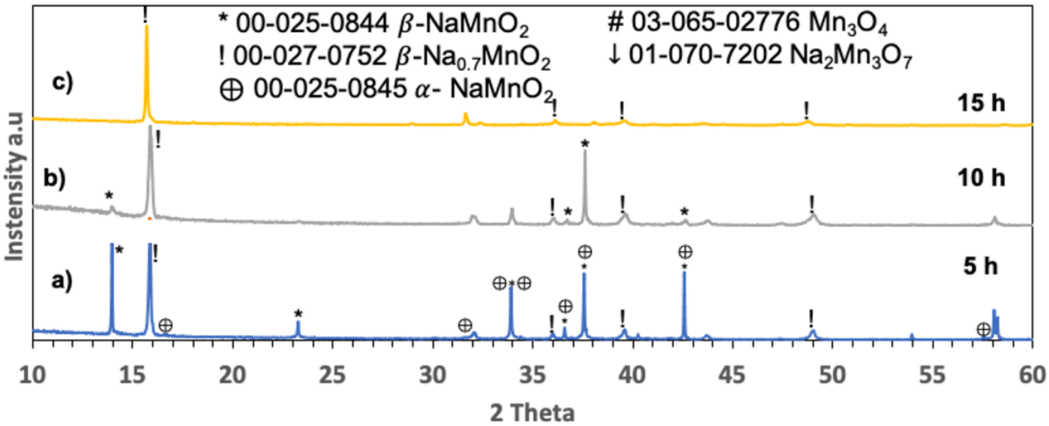

Figure 3.6 XRD pattern of sintered $NaMnO_2$ targets at 1350°C for **a)** 5h, **b)** 10h, **c)** 15h

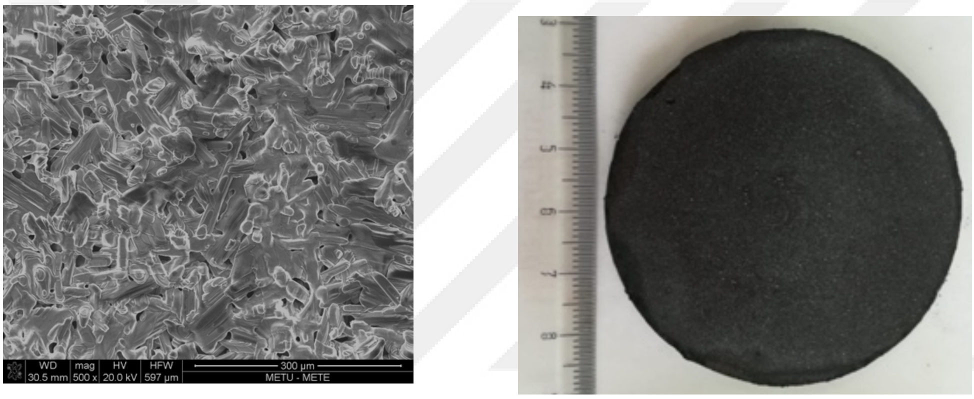

a) **b)**

Figure 3.7 $Na_{0.7}MnO_2$ sputter target sintered at 1350°C **a)** SEM micrograph **b)** sputter target

Having determined the conditions of sintering, noting that little shrinkage takes place in sintering, the powders were pressed into 55 mm diameter Teflon ring and sintered in the same conditions. The resulting pellet is shown in Figure 3.7 (b). This pellet was reduced in diameter to 50 mm by grinding its periphery.

3.2.2 Bi_2O_3

Bi_2O_3 was synthesized from Bismuth oxynitrate ($Bi_5O(OH)_9(NO_3)_4$, 71% Bi basis Merck). For this purpose, Bismuth oxynitrate powders were placed in a crucible and calcined in air. XRD pattern of the powder resulting from calcination at 600°C after 1.5 hours is given in Figure 3.8. The pattern was compatible with Bi_2O_3 (pdf card no. 00-027-0052). Cell parameters as derived from XRD pattern using a related CIF file via Rietvelt refinement were a=5.859Å, b=8.171 Å, c=7.517 Å. Representative SEM images recorded from synthesized powders are given in Figure 3.9.

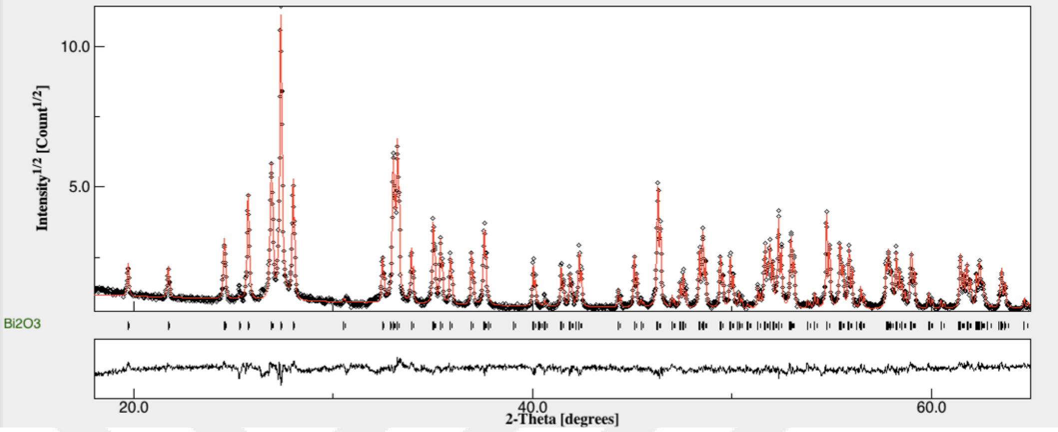

Figure 3.8 XRD pattern of as-synthesized Bi_2O_3 powder at 600°C

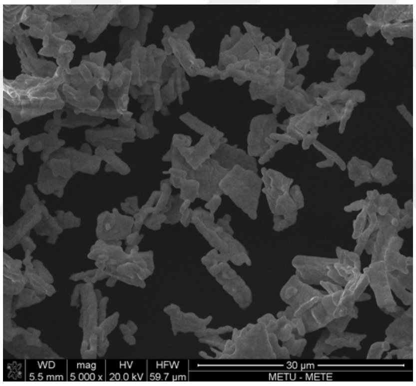

Figure 3.9 SEM image of synthesized Bi_2O_3 powder

For target making small pellets 20 mm in diameter were pressed and sintered at 600°C. XRD pattern was very similar to that given in Figure 3.8. SEM micrograph after sintering is given in Figure 3.10 (a) where the structure is almost fully dense.

Having determined the sintering conditions powders calcined at 600°C were pressed into a Teflon ring of 65 mm in diameter and the pellet was sintered at 600°C for 5 hours. The resulting pellet was ground at its periphery so that its diameter was 50 mm. A photograph of Bi_2O_3 sputter target produced in this way is shown in Figure 3.10 (b).

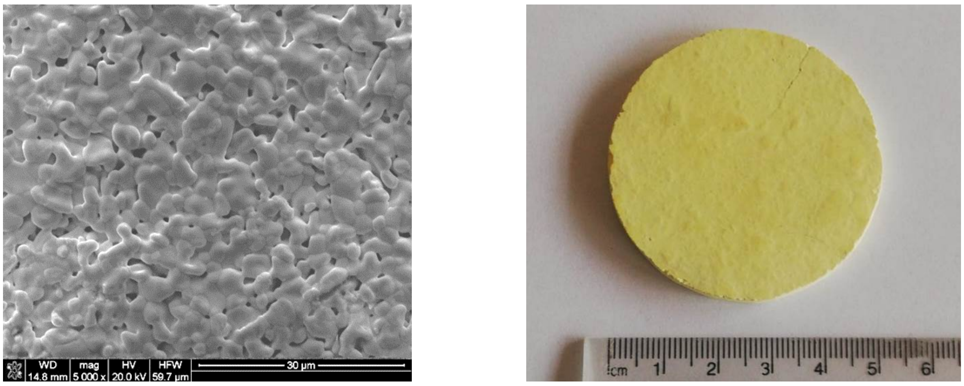

a) **b)**

Figure 3.10 Bi_2O_3 sputter target sintered at **a)** SEM image (20 mm pellet), **b)** sputter target

3.2.3 NiO

NiO was synthesized from nickel (II) nitrate hexahydrate ($(Ni(NO)_3.6H_2O$, Merck 99%). For this purpose, nickel nitrate powders were placed in a crucible and calcined in air. XRD pattern of the powder resulting from calcination at 800℃ after 1 hour is given in Figure 3.11. The pattern was compatible with cubic NiO (pdf card no. 04-001-9373). Cell parameters as derived from XRD pattern using a related CIF file via Rietvelt refinement were a=4.179Å. Representative SEM images recorded from synthesized powders are given in Figure 3.12.

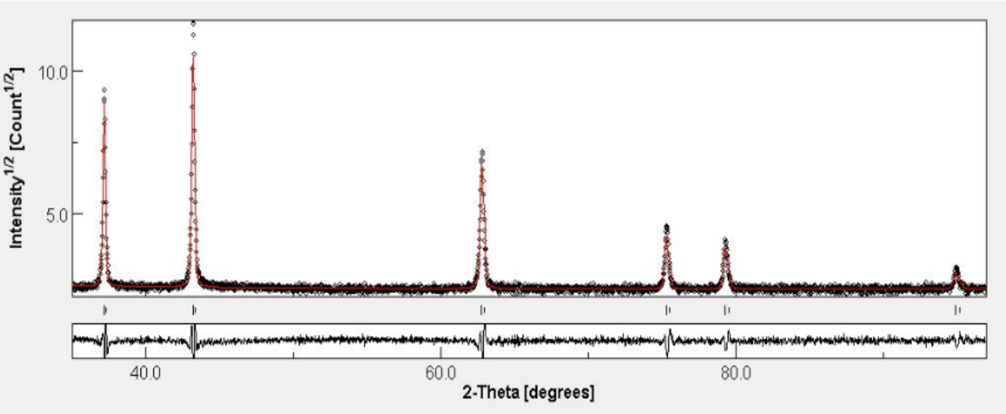

Figure 3.11 XRD pattern of as-synthesized NiO powder at 800℃

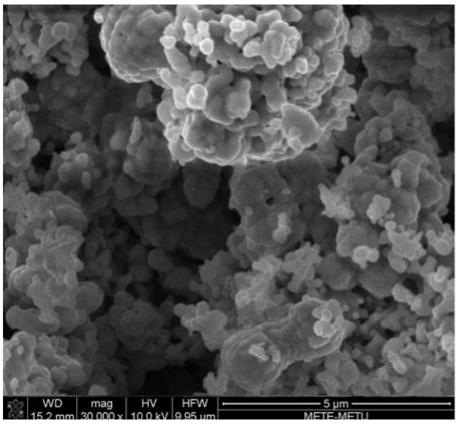

Figure 3.12 SEM image of synthesized NiO powder

For target making small pellets 20 mm in diameter were pressed and sintered at 1250℃. XRD pattern was very similar to that given in Figure 3.11. SEM micrograph after sintering is given in in Figure 3.13 (a) where the structure is almost fully dense. Having determined the sintering conditions, powders calcined at 800℃ were pressed into a Teflon ring of 65 mm in diameter and the pellet was sintered at 1250℃ for 7 hours. The resulting pellet was ground at its periphery so that its diameter was 50 mm. A photograph of NiO sputter target produced in this way is shown in Figure 3.13 (b).

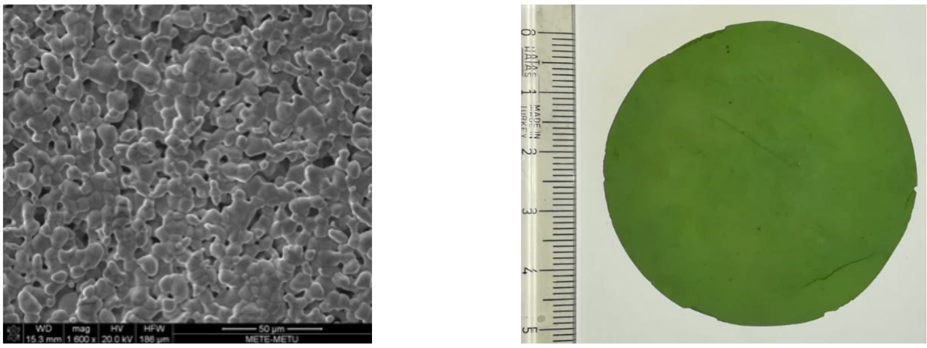

a) **b)**

Figure 3.13 **a)** SEM image of sintered NiO (20 mm pellet) in air, **b)** 2-inch NiO target

3.3 Summary

Active materials were synthesized successfully and discs of $Na_{0.7}MnO_2$, Bi_2O_3 and NiO in 2-inch diameter were successfully produced by sintering the pressed pellets at elevated temperature. In addition to these discs, the use was made of MnO_2 disc in 3-inch in diameter which was procured from Changsha Xinkang Advanced Materials Co., Ltd.

CHAPTER 4

COMBINATORIAL DEVELOPMENT OF MnO_2-BASED CATHODES FOR Zn-MnO_2 BATTERIES

4.1 Introduction

Batteries are normally prepared by slurry method, i.e., anode and cathodes were prepared as slurry and applied to current collectors. Solid state batteries are somewhat different as a certain fraction of them are prepared via PVD methods [69]. Zhou et al. [69] reported that battery components of anode, cathode and electrolyte can be deposited layer by layer to make all-solid-state battery with thickness less than 20 μm. Thus, energy dense batteries can be produced without using conductive additive or binders. Lobe at al. [70] summarized the PVD process in which material is deposited from the gas phase. Its main advantage is the creation of dense solid layers with a tunable thickness, adjustable and controlled composition, crystallinity, and crystal orientation. Further, the contamination is minimal due to the absence of organic reactants, and there is the option to sequentially deposition of several materials.

Combinatorial approach based on sputter deposition were investigated for Li-ion batteries [71]-[72]. Exploring the different methods of film deposition, Bouwman et al. [71] stated that for $LiCoO_2$ films deposited by radiofrequency (RF) sputtering exhibited an *a*-axis orientation while those deposited by PLD showed a *c*-axis orientation. Whitacre et al. [73] combinatorial sputter deposited cathode, anode, and electrolyte with different compositions. This simultaneous approach allowed many solid-state micro-batteries that had $Li_yMn_xNi_{2-x}O_4$ cathodes, where x varied from 0.2 to 1.8 and y varied from 2.7 to 3.7 in the as-deposited films. Meanwhile lithium phosphorus oxynitride was used as electrolyte and evaporated Li metal was the anode. Cathode with composition of $LiMn_{1.4}Ni_{0.6}O_4$ had both the highest specific capacity and longest high-potential discharge plateau. Finally, conventionally made cathode with same composition aggreged with similar result. Fleischauer et al. [72] combinatorial sputtered Si anodes for Li-ion batteries. They deposited Si on a lead patterned circuit having 64 channels of 5 mm diameter of contact pads. Depending on the distance, capacity per unit area of the electrode changed. The near to target, higher areal capacity obtained. They showed that combinatorial deposited 64 cells assembly in 10 min which equals to assembly of two conventionally made coin cell.

Hanak [74] studied combinatorial sputtering with very interesting targets. They made a twofold circular target half is material A and other half is material B or threefold circular target with three portions of material. Another target was made as circular target that include smaller circular target in it with different material. Hatchard et al. [75] studied combinatorial sputtering with multiple sputter target.

For MnO_2, changing sputtering parameters different microstructures and/or different phases can be made. Borysiewicz et al. [76] studied relationship between process conditions and structural properties for MnO_2. For 0, 1 and 5 sccm oxygen flow, when chamber pressure increased deposition rate decreases for all conditions. MnO_2 target were used. A composition of λ-MnO_2/γ-MnO_2 was found for no oxygen content. Meanwhile, the composition changed to β-MnO_2/γ-MnO_2 for intermediate oxygen content, and γ-MnO_2 phase was dominating when largest oxygen content was present. LIN et al. [77] studied sputtering of MnO_2 thin film by using Mn target. Increasing oxygen content was yielded as Mn_2O_3 formation and increasing sputtering time was yielded as needle shape of grains.

In our lab, Pişkin et al. and Sarı et al. have used combinatorial approach to determine compositions suitable for hydrogen separation membranes [78][79][80] and cathodes for intermediate temperature solid oxide fuel cells [67].

In this chapter cathodes for Zn-MnO_2 batteries were sputter deposited in Bi_2O_3-$Na_{0.7}MnO_2$-NiO ternary system. The aim was to identify cathode compositions with superior electrochemical performance.

4.2 Experimental Procedure

4.2.1 Sputter deposition of cathodes

Vacuum chamber used for sputter deposition was 500x500x500 mm, Figure 4.1. The chamber incorporates a total three peripheral sputter guns in 2-inch diameter placed at a circle of 350 mm and 120° apart. The chamber also incorporates a central gun in 3-inch in diameter.

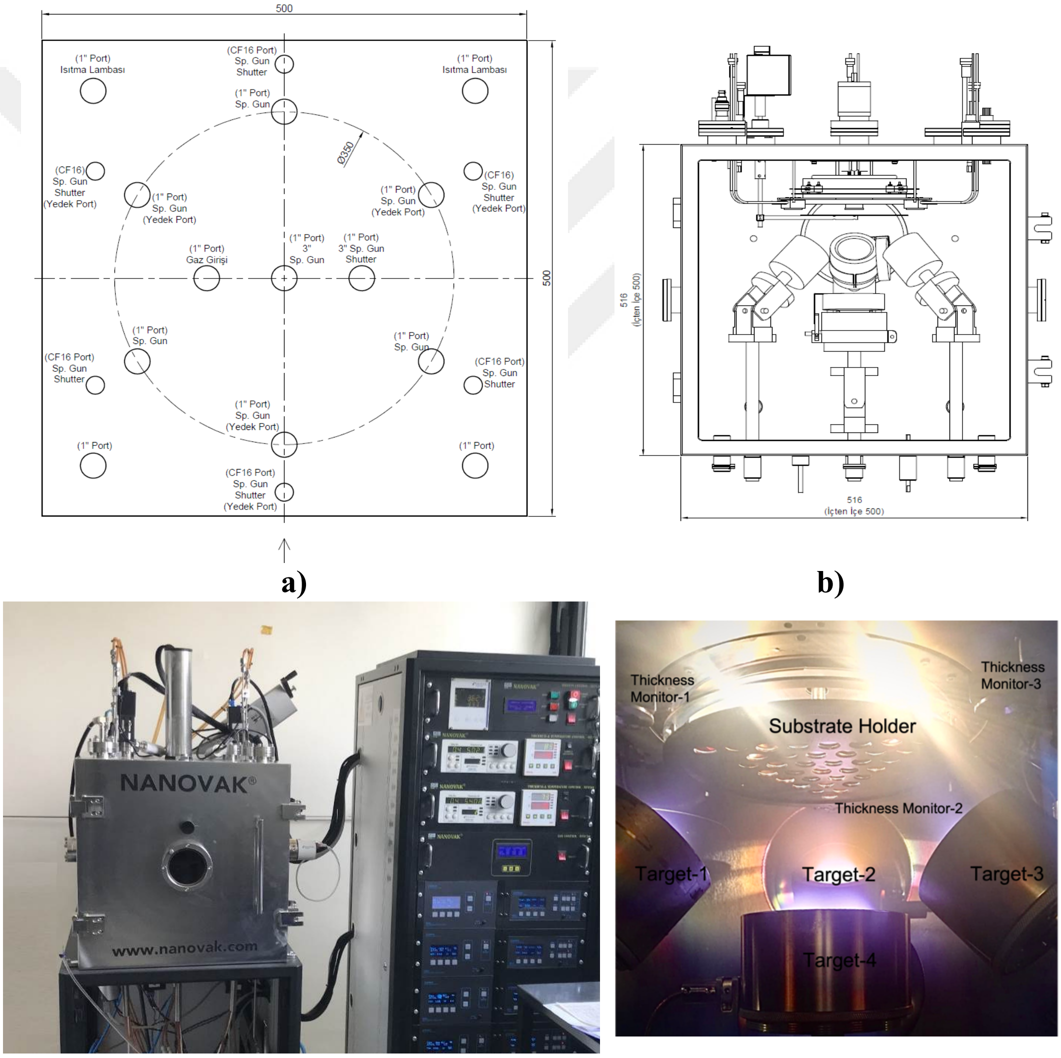

a) **b)**

c) **d)**

Figure 4.1 Technical drawing of Nanovak magnetron sputtering **a)** top view, **b)** side view and photograph of the machine **c)** outside, **d)** inside view

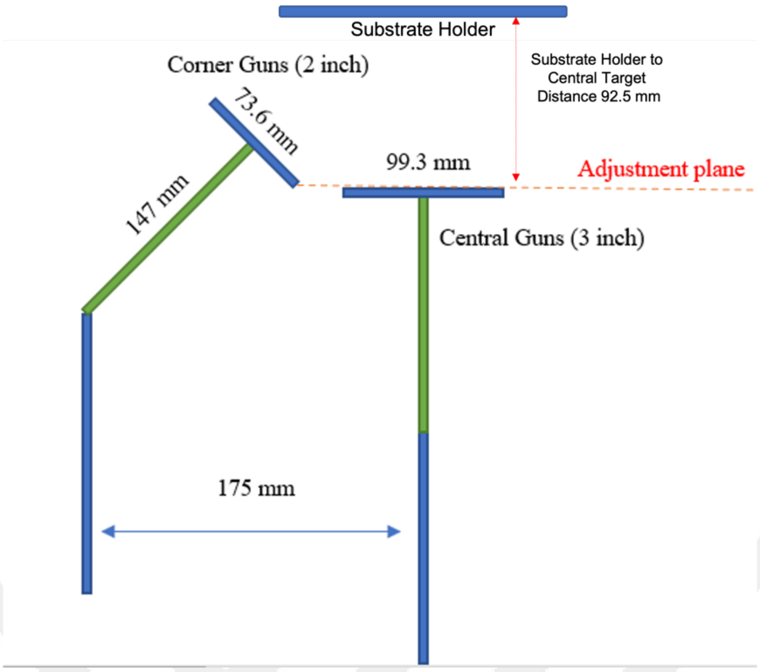

Figure 4.2 Gun positions

The guns were aligned in the following manner. First the height of the central gun was adjusted such that the distance to the substrate plane was 92.5 mm. Then peripheral guns were tilted as shown in Figure 4.2 i.e., the lower edge of the peripheral target holder was just touching the central target plane. In this position the tilt angle was 45°. Samples were placed in a substrate magazine at the substrate plane, Figure 4.3. As seen in Figure 4.3, the substrates were 12.7 mm in diameter in a triangular geometry. A total 36 substrates could be loaded on the substrate magazine. The alignment of the peripheral guns was also checked with sensors placed closed to the corners of the triangle: The rotation of the gun was made such that two sensors away from the gun reads the same deposition rate.

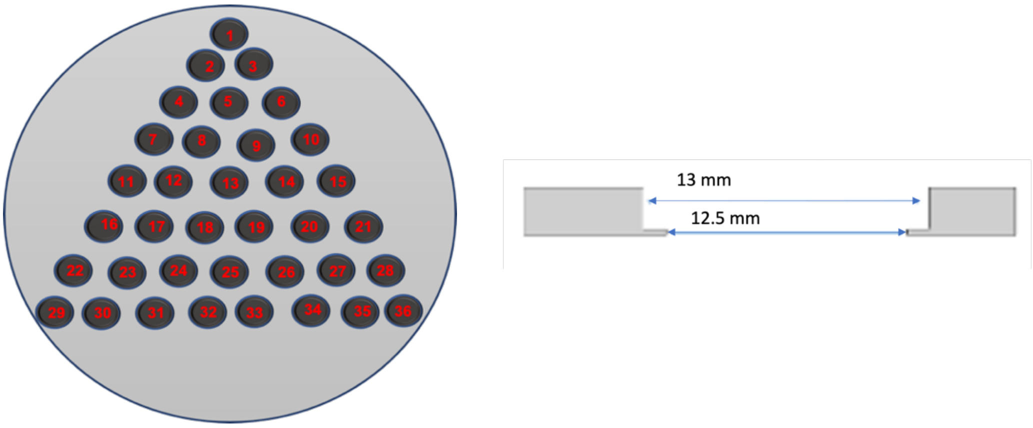

a) **b)**

Figure 4.3 Schematic presentation of sample holder **a)** top view, **b)** side view

Having placed the targets in their gun and substrates to the sample magazine, the experiment was initiated by taking the chamber under vacuum. Once the base pressure reached 10^{-7} Torr, sputtering gas of high purity argon (99.999%, Linde Gaz Inc.) and high purity oxygen (99.999%, Linde Gaz Inc.) were fed with 10 and 13 sccm, respectively. The total chamber pressure was kept at 10^{-3} Torr and gas pressure was kept at 5 mTorr. Once the chamber pressure and argon pressure stabilize, targets were started with proper power settings increases with 0.5 W/sec. Increasing the power load slow protects the targets since they all were ceramic which having insulating behavior. Finally, targets and sample shutters were turned on, respectively.

The experiment first involved the determination of tooling factor. Once gun positions were fixed, tooling factor of thickness monitors were calibrated. Thickness sensor calculation includes materials density, z-ratio, and tooling factor. Materials density and z-ratio are material dependent variables. Therefore, tooling factor should be calibrated. For this purpose, sputtering was made for each target. Glass substrate was selected. Initial tooling factor set as 100. Argon flow set as 10 sccm and oxygen flow set as 13 sccm. Total chamber pressure was kept as 3 mTorr.130 min and 360 min coating were made for peripheral and central guns, respectively. Thickness monitor value is recorded. Then real thickness was measured under SEM. Finally, tooling factor were corrected. For tooling factor determination of the thickness monitor for NiO target, materials density, z-ratio, and tooling factor were set as 7.450, 1 and 100, respectively. After 130 min deposition, measured thickness was ≈100 nm under SEM and sensor thickness was 150 nm. Therefore, tooling factor was set as 66.7.

4.2.2 Material Characterization

4.2.2.1 Structural Characterization

Structural analysis of sputtered cathodes was carried out X-ray diffraction using Rigaku DMAX2200 or Bruker D8 Advance X-ray diffractometer. Rigaku and Bruker X-ray diffractometer were used with Cu-K_α radiation (λ=1.5406Å) at 30 kV acceleration and 40 mA current. The scanning rate was 1°/min with step size of 0.02°.

Sputtered samples were also investigated with Scanning electron microscopy. For this purpose, FEI Nova NanoSEM was used (20 kV with SE detector). Where necessary the samples were investigated with EDS analysis. Weighing of sputtered samples were carried out using Sartorius CPA225D (0.01 mg sensitivity). Measurements were recorded when the balance was reliably stabilized.

4.2.2.2 Electrochemical Characterization

Cells used for electrochemical characterization was of Swagelok type, Figure 4.4. MnO_2 based cathode sputtered on nickel disc 80 μm thick and has a diameter of 12.7 mm in diameter was used as cathode. Anode was Zn foil 300 μm thick (99.8% pure). Separator was 180 μm thick Freudenberg FS 2226. Electrolyte was 2M $ZnSO_4$+0.1M $MnSO_4$ in DI water. Current collectors in the Swagelok cell were 12.9 mm diameter stainless steel rods. Cell has a spring which keep the cell steady state. Spring has a rod diameter of 1 mm and diameter of 12.4 mm and height of 10.5 mm. Cells were assembled starting from cathode and separator first. Then 0.5 ml electrolyte were dripped and let the separator absorb. Finally, Zn foil anode were placed. Before anode current collector rod, 10 mm height of stainless-steel rod and spring were placed, then cell closed by tighten the valves.

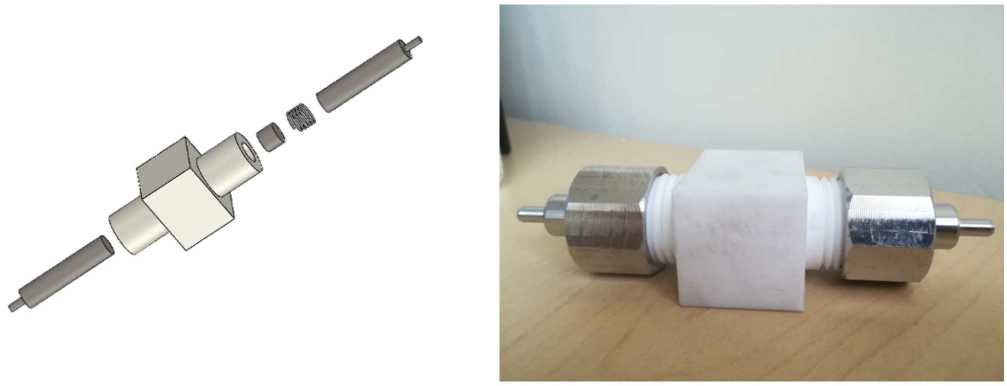

a) **b)**

Figure 4.4 Swagelok type cell **a)** schematic view, **b)** photograph of the cell in as – assembled form

a) **b)**

Figure 4.5 16 channel battery testing system **a)** cabin, **b)** sliding shelves with mounted cells inside the cabin

Electrochemical measurements were made with BioLogic MPG2 cell testing equipment, Figure 4.5. It incorporates total of 16 channels. Cyclic voltammetry (CV) was measured scanning between 1.0 V and 2.0 V with sweep rate of 2 mV/sec for 15 cycles. Galvanostatic testing were made between 1.0 V and 1.9 V for 50 cycles. Samples were investigated under constant current with rate of 61.6 mA/g. Having reached the cut-off voltage, the cell rested for 5 minutes before continuing the test. Rate capability tests were carried out with rates of 61.6, 154, 308 and 616 mA/g each for 5 cycles each.

4.3 Combinatorial Development of MnO_2-Based Cathodes

4.3.1 Compositional mapping

Bi_2O_3 $Na_{0.7}MnO_2$ and NiO targets 2-inch in diameter were placed in the peripheral guns an MnO_2 target of 3-inch in diameter were placed in the central gun. Tooling factors which had been determined entered the respective channel of the thickness monitor. A total of 6 experiments were carried out using power settings as given in Table 4.1 The experiments were carried out first on aluminum substrate (200 μm thick) for duration of 7 hours yielding 1.23 μm thick films. Then the experiment was repeated in the same conditions for nickel substrate (200 μm thick) for 17 hours where the thickness was approximately 3 μm (measured in the corners of the triangular substrate magazine).

A total 36 cathodes deposited on aluminum substrate were characterized with EDS analysis. Three measurements were taken on the sample under low magnification each with a duration of 60 seconds. The compositions determined are shown plotted in Figure 4.6 (a) where the power settings of the targets were 30, 100, 100 and 100 W for Bi_2O_3, $Na_{0.7}MnO_2$, NiO and MnO_2, respectively. Here each composition shown was such that atomic fractions of Bi, Ni and Na summed up to 1 and the atomic fraction of Mn was normalized accordingly. Thus, atomic fraction summed up for all elements when Mn was included were therefore greater than 1. As can be seen in Figure 4.6 (a), thin film cathodes are on collected more towards Na-Ni line. In order to obtain a more homogenous distribution, a second experiment, i.e., Experiment B, was carried out in which the power setting of Bi_2O_3 target was reduced. The power setting of the subsequent four depositions is given in Table 4.1

and were successful in yielding thin films with richer Na content. These are shown plotted in in Figure 4.6.

Table 4.1 Power parameters of different series of sputtering.

Experiment	**Bi_2O_3 (Watt)**	**$Na_{0.7}MnO_2$ (Watt)**	**NiO (Watt)**	**MnO_2 (Watt)**
A	**30**	**100**	**100**	**100**
B	20	100	50	120
C	15	100	25	120
D	**15**	**100**	**35**	**120**
E	10	50	25	120
F	**10**	**25**	**25**	**120**

With 6 sputter deposition experiment each producing 36 thin film electrodes, a total of 216 samples were fabricated. Since some samples were close to one another, a subset comprising a total of 108 samples were selected for detailed study. The selected compositions are shown plotted in Figure 4.7 as Bi-Na-Ni ternary diagram.

Even though the original aim was to examine the modification of MnO_2 with NiO, Bi_2O_3 and Na bearing additives, it was found more useful to look at the chemistry change in Bi-Mn-Ni space. For this reason, the samples reported in Figure 4.7 are replotted in Figure 4.8 as Bi-Mn-Ni space. In particular, Mn corner in Bi-Mn-Ni space contain samples with attractive properties. For this reason, a portion of this space is redrawn in higher magnification in Figure 4.9. Chemical compositions of the samples within the magnified portion are tabulated in Table 4.2.

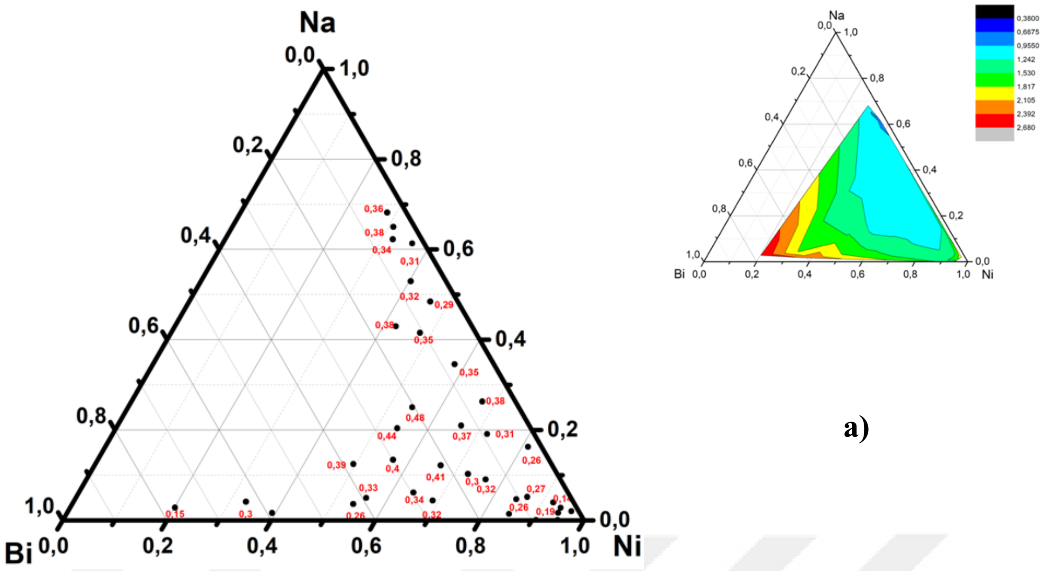
Na
0,0
1,0
0,2
0,8
0,4
0,6
0,6
0,4
0,8
0,2
1,0
0,0
Bi
0,0
0,2
0,4
0,6
0,8
1,0
Ni
0,36
0,38
0,34
0,31
0,32
0,29
0,38
0,35
0,35
0,38
0,48
0,44
0,37
0,31
0,26
0,39
0,4
0,41
0,3
0,32
0,33
0,34
0,27
0,14
0,26
0,19
0,15
0,3
0,26
0,32
Na
0,0
1,0
0,2
0,8
0,4
0,6
0,6
0,4
0,8
0,2
1,0
0,0
Bi
0,0
0,2
0,4
0,6
0,8
1,0
Ni
0,3800
0,6675
0,9550
1,242
1,530
1,817
2,105
2,392
2,680

a)

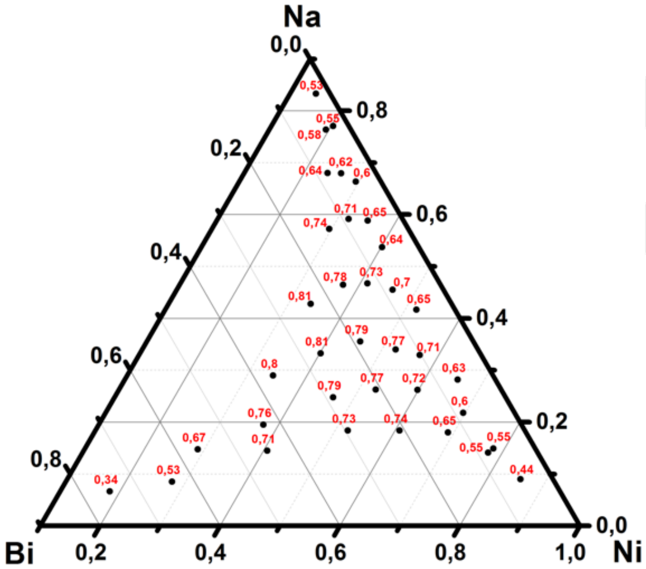
Na
0,0
0,2
0,8
0,4
0,6
0,6
0,4
0,8
0,2
0,0
Bi
0,2
0,4
0,6
0,8
1,0
Ni
0,53
0,55
0,58
0,62
0,64
0,6
0,71
0,65
0,74
0,64
0,78
0,73
0,7
0,81
0,65
0,79
0,81
0,77
0,71
0,8
0,63
0,79
0,77
0,72
0,6
0,76
0,73
0,74
0,65
0,67
0,71
0,55
0,55
0,53
0,44
0,34

b)

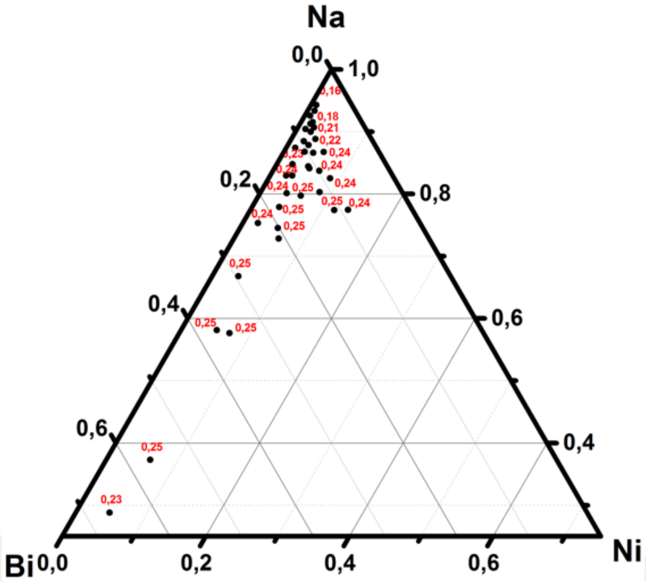
Na
0,0
1,0
0,2
0,8
0,4
0,6
0,6
0,4
Bi
0,0
0,2
0,4
0,6
Ni
0,16
0,18
0,21
0,22
0,23
0,24
0,24
0,24
0,24
0,25
0,24
0,25
0,24
0,25
0,24
0,25
0,25
0,25
0,25
0,25
0,23

c)

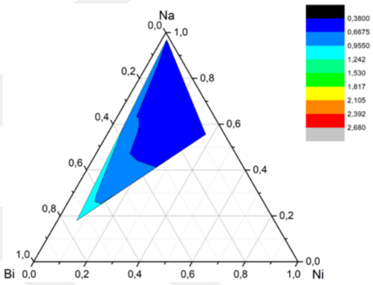
Na
0,0
1,0
0,2
0,8
0,4
0,6
0,6
0,4
0,8
0,2
1,0
0,0
Bi
0,0
0,2
0,4
0,6
0,8
1,0
Ni
0,3800
0,6675
0,9550
1,242
1,530
1,817
2,105
2,392
2,680

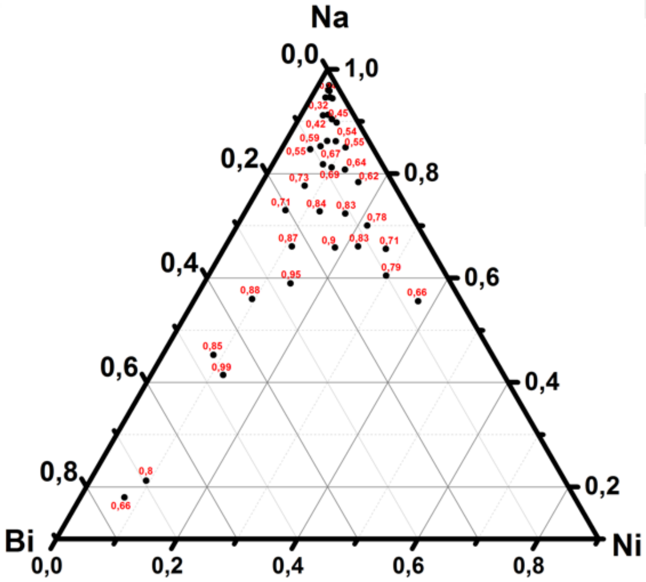
Na
0,0
1,0
0,2
0,8
0,4
0,6
0,6
0,4
0,8
0,2
Bi
0,0
0,2
0,4
0,6
0,8
Ni
0,32
0,45
0,42
0,54
0,59
0,55
0,55
0,67
0,64
0,73
0,69
0,62
0,71
0,84
0,83
0,78
0,87
0,9
0,83
0,71
0,79
0,95
0,88
0,66
0,85
0,99
0,8
0,66

d)

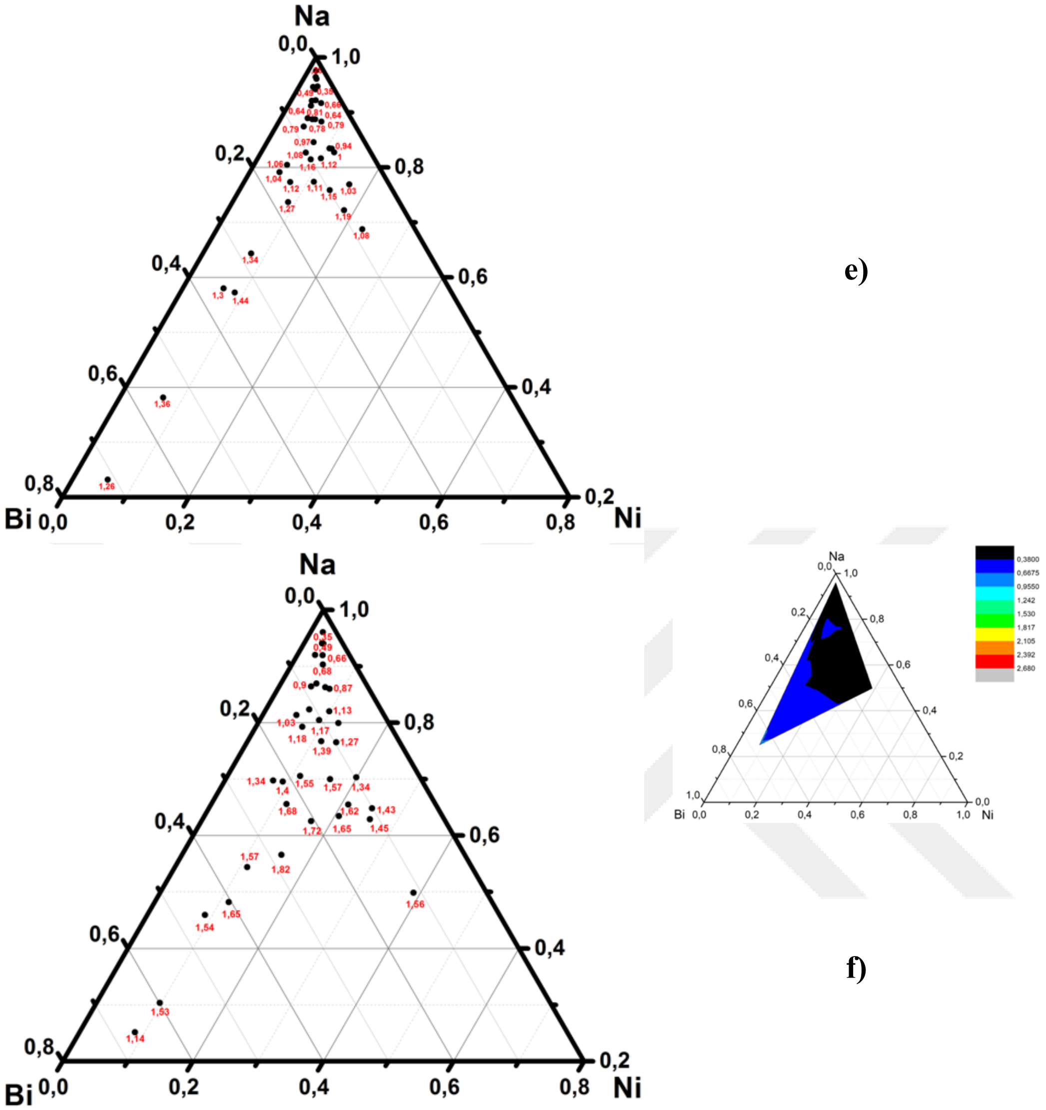

e)

f)

Figure 4.6 Composition distribution on Bi-Na-Ni ternary diagram. Power settings of targets Bi_2O_3-$Na_{0.7}MnO_2$-NiO-MnO_2 were **a)** 30-100-100-100W, **b)** 20-100-50-120W, **c)** 15-100-25-120W, **d)** 15-100-35-120W, **e)** 10-50-25-120W, **f)** 10-25-25-120W. Mass distribution of sputter deposited layers are also shown at the side map for (a), (d) and (f)

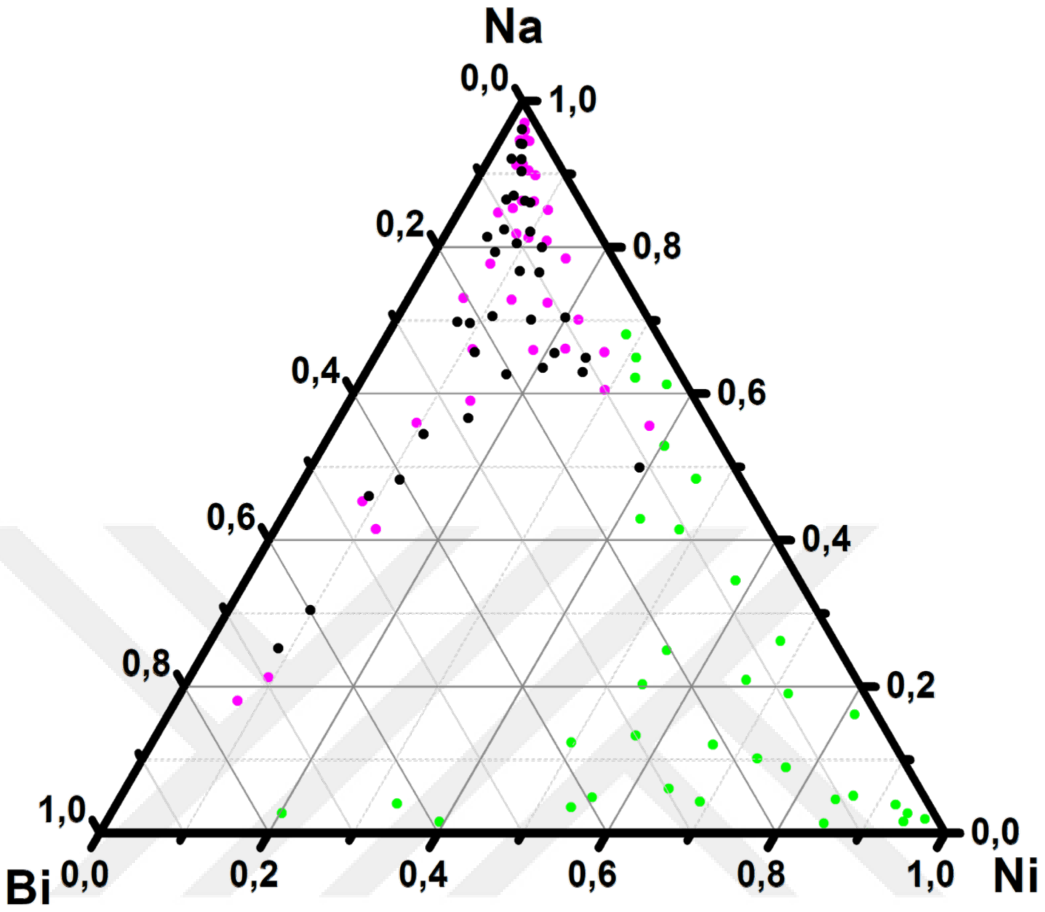

Figure 4.7 Samples on Bi-Na-Ni ternary from three different power combination sputter process (Green, magenta, and black are A, D and F, respectively)

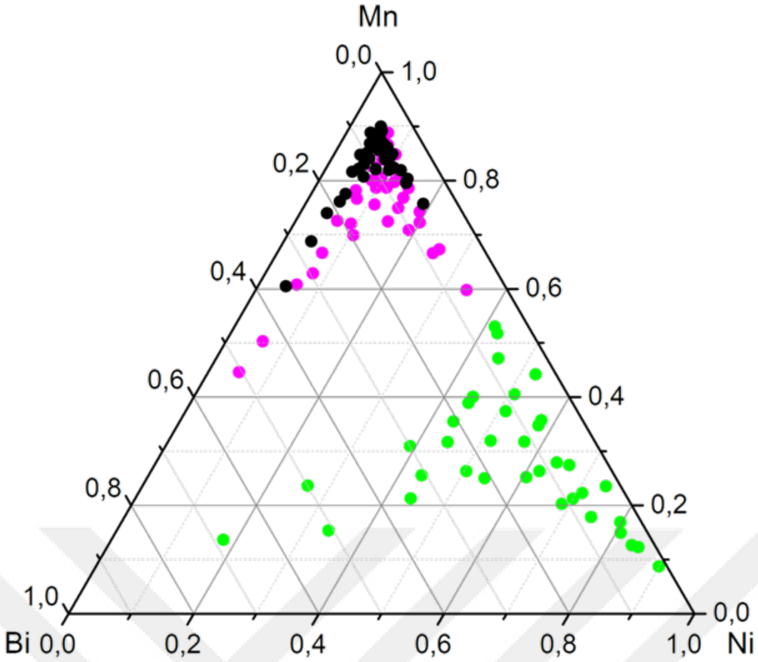

Figure 4.8 Samples on Bi-Mn-Ni ternary from three different power combination sputter process (Green, magenta, and black are A, D and F, respectively)

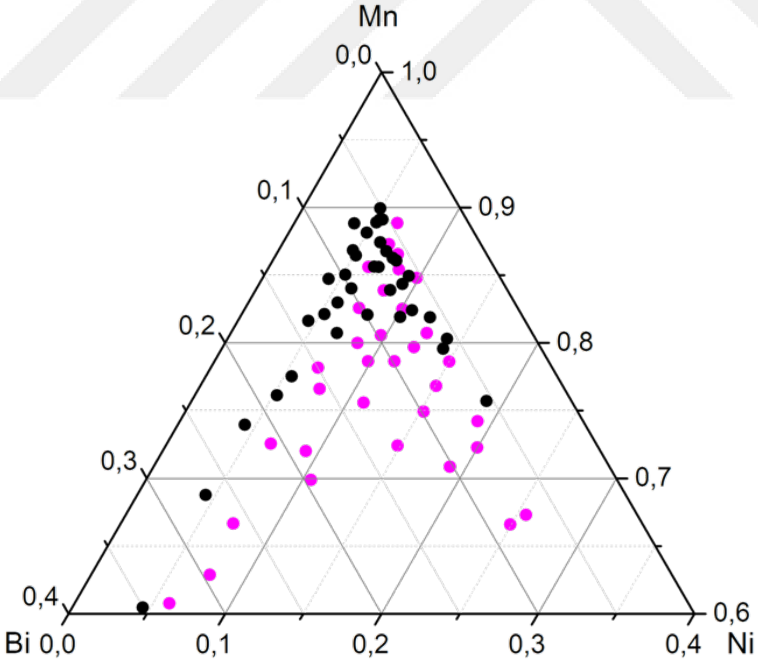

Figure 4.9 Bi-Mn-Ni ternary diagram for Mn-rich compositions

Table 4.2 List of material library that selected samples for Mn sides

Mass(mg)	Bi	Na	Ni	Mn	Formula
0.72	0.01	0.78	0.01	0.20	$Bi_{0.01}Na_{0.78}Ni_{0.01}Mn_{0.20}O_x$
0.65	0.01	0.75	0.02	0.22	$Bi_{0.01}Na_{0.75}Ni_{0.02}Mn_{0.22}O_x$
0.69	0.01	0.76	0.02	0.21	$Bi_{0.01}Na_{0.76}Ni_{0.02}Mn_{0.21}O_x$
0.58	0.02	0.71	0.02	0.24	$Bi_{0.02}Na_{0.71}Ni_{0.02}Mn_{0.24}O_x$
0.59	0.02	0.72	0.02	0.24	$Bi_{0.02}Na_{0.72}Ni_{0.02}Mn_{0.24}O_x$
0.54	0.01	0.72	0.03	0.24	$Bi_{0.01}Na_{0.72}Ni_{0.03}Mn_{0.24}O_x$
0.59	0.04	0.64	0.03	0.29	$Bi_{0.04}Na_{0.64}Ni_{0.03}Mn_{0.29}O_x$
0.55	0.03	0.63	0.03	0.31	$Bi_{0.03}Na_{0.63}Ni_{0.03}Mn_{0.31}O_x$
0.57	0.03	0.62	0.04	0.31	$Bi_{0.03}Na_{0.62}Ni_{0.04}Mn_{0.31}O_x$
0.58	0.03	0.63	0.05	0.30	$Bi_{0.03}Na_{0.63}Ni_{0.05}Mn_{0.30}O_x$
0.52	0.04	0.55	0.04	0.36	$Bi_{0.04}Na_{0.55}Ni_{0.04}Mn_{0.36}O_x$
0.56	0.04	0.56	0.05	0.35	$Bi_{0.04}Na_{0.56}Ni_{0.05}Mn_{0.35}O_x$
0.59	0.12	0.43	0.04	0.42	$Bi_{0.12}Na_{0.43}Ni_{0.04}Mn_{0.42}O_x$
0.61	0.09	0.45	0.04	0.42	$Bi_{0.09}Na_{0.45}Ni_{0.04}Mn_{0.42}O_x$
0.58	0.04	0.49	0.08	0.39	$Bi_{0.04}Na_{0.49}Ni_{0.08}Mn_{0.39}O_x$
0.57	0.12	0.35	0.06	0.47	$Bi_{0.12}Na_{0.35}Ni_{0.06}Mn_{0.47}O_x$
0.58	0.08	0.39	0.07	0.46	$Bi_{0.08}Na_{0.39}Ni_{0.07}Mn_{0.46}O_x$
0.55	0.06	0.40	0.09	0.45	$Bi_{0.06}Na_{0.40}Ni_{0.09}Mn_{0.45}O_x$
0.44	0.05	0.39	0.12	0.44	$Bi_{0.05}Na_{0.39}Ni_{0.12}Mn_{0.44}O_x$
0.48	0.04	0.38	0.16	0.41	$Bi_{0.04}Na_{0.38}Ni_{0.16}Mn_{0.41}O_x$
0.54	0.14	0.30	0.07	0.49	$Bi_{0.14}Na_{0.30}Ni_{0.07}Mn_{0.49}O_x$
0.50	0.07	0.36	0.12	0.45	$Bi_{0.07}Na_{0.36}Ni_{0.12}Mn_{0.45}O_x$
0.50	0.06	0.34	0.17	0.44	$Bi_{0.06}Na_{0.34}Ni_{0.17}Mn_{0.44}O_x$
0.36	0.01	0.71	0.01	0.26	$Bi_{0.01}Na_{0.71}Ni_{0.01}Mn_{0.26}O_x$
0.37	0.02	0.64	0.02	0.32	$Bi_{0.02}Na_{0.64}Ni_{0.02}Mn_{0.32}O_x$
0.24	0.02	0.63	0.02	0.33	$Bi_{0.02}Na_{0.63}Ni_{0.02}Mn_{0.33}O_x$
0.24	0.03	0.56	0.02	0.39	$Bi_{0.03}Na_{0.56}Ni_{0.02}Mn_{0.39}O_x$
0.26	0.03	0.54	0.03	0.40	$Bi_{0.03}Na_{0.54}Ni_{0.03}Mn_{0.40}O_x$
0.29	0.02	0.56	0.02	0.40	$Bi_{0.02}Na_{0.56}Ni_{0.02}Mn_{0.40}O_x$
0.27	0.04	0.44	0.03	0.49	$Bi_{0.05}Na_{0.46}Ni_{0.03}Mn_{0.47}O_x$
0.29	0.03	0.45	0.04	0.47	$Bi_{0.04}Na_{0.44}Ni_{0.03}Mn_{0.49}O_x$
0.28	0.03	0.46	0.04	0.46	$Bi_{0.03}Na_{0.45}Ni_{0.04}Mn_{0.47}O_x$
0.28	0.07	0.40	0.03	0.51	$Bi_{0.03}Na_{0.46}Ni_{0.04}Mn_{0.46}O_x$
0.32	0.05	0.39	0.03	0.53	$Bi_{0.07}Na_{0.40}Ni_{0.03}Mn_{0.51}O_x$
0.30	0.05	0.37	0.04	0.54	$Bi_{0.05}Na_{0.39}Ni_{0.03}Mn_{0.53}O_x$
0.27	0.04	0.39	0.05	0.53	$Bi_{0.05}Na_{0.37}Ni_{0.04}Mn_{0.54}O_x$
0.27	0.04	0.37	0.06	0.53	$Bi_{0.04}Na_{0.39}Ni_{0.05}Mn_{0.53}O_x$
0.20	0.10	0.30	0.03	0.57	$Bi_{0.04}Na_{0.37}Ni_{0.06}Mn_{0.53}O_x$
0.31	0.09	0.29	0.04	0.58	$Bi_{0.10}Na_{0.30}Ni_{0.03}Mn_{0.57}O_x$
0.37	0.06	0.36	0.03	0.54	$Bi_{0.09}Na_{0.29}Ni_{0.04}Mn_{0.58}O_x$
0.43	0.05	0.32	0.05	0.58	$Bi_{0.06}Na_{0.36}Ni_{0.03}Mn_{0.54}O_x$
0.40	0.04	0.34	0.06	0.56	$Bi_{0.05}Na_{0.32}Ni_{0.05}Mn_{0.58}O_x$
0.39	0.04	0.30	0.09	0.57	$Bi_{0.04}Na_{0.34}Ni_{0.06}Mn_{0.56}O_x$
0.32	0.18	0.18	0.04	0.61	$Bi_{0.04}Na_{0.30}Ni_{0.09}Mn_{0.57}O_x$
0.53	0.13	0.21	0.04	0.61	$Bi_{0.18}Na_{0.18}Ni_{0.04}Mn_{0.61}O_x$
0.45	0.09	0.25	0.04	0.63	$Bi_{0.13}Na_{0.21}Ni_{0.04}Mn_{0.61}O_x$
0.28	0.07	0.28	0.04	0.61	$Bi_{0.09}Na_{0.25}Ni_{0.04}Mn_{0.63}O_x$

Table 4.2 (cont'd)

0.37	0.05	0.27	0.06	0.61	$Bi_{0.07}Na_{0.28}Ni_{0.04}Mn_{0.61}O_x$
0.32	0.05	0.25	0.08	0.62	$Bi_{0.05}Na_{0.27}Ni_{0.06}Mn_{0.61}O_x$
0.26	0.04	0.27	0.10	0.59	$Bi_{0.05}Na_{0.25}Ni_{0.08}Mn_{0.62}O_x$
0.57	0.24	0.12	0.04	0.61	$Bi_{0.24}Na_{0.12}Ni_{0.04}Mn_{0.61}O_x$
0.42	0.15	0.18	0.04	0.62	$Bi_{0.15}Na_{0.18}Ni_{0.04}Mn_{0.62}O_x$
0.31	0.10	0.20	0.05	0.65	$Bi_{0.10}Na_{0.20}Ni_{0.05}Mn_{0.65}O_x$
0.23	0.08	0.23	0.06	0.63	$Bi_{0.08}Na_{0.23}Ni_{0.06}Mn_{0.63}O_x$
0.31	0.06	0.24	0.08	0.62	$Bi_{0.06}Na_{0.24}Ni_{0.08}Mn_{0.62}O_x$
0.31	0.05	0.26	0.11	0.59	$Bi_{0.05}Na_{0.26}Ni_{0.11}Mn_{0.59}O_x$
0.28	0.04	0.19	0.15	0.61	$Bi_{0.04}Na_{0.19}Ni_{0.15}Mn_{0.61}O_x$

4.3.2 Structural Characterization

Cathodes deposited on Ni substrate were characterized with X-ray diffraction using Bragg-Brentano geometry. A typical spectrum recorded between $10° < 2\theta < 85°$ is given in Figure 4.10. It is seen that there is a broad peak centered at $2\theta \approx 16°$ plus three well defined sharp peaks located at $2\theta = 44.78°$, 52.06° and 76.47°. These peaks refer to nickel which was used as substrate during the sputter deposition. Since the cathodes deposited are oxides, they are expected to produce peaks at low angles. For that reason, X-ray diffraction was confined to $10° < 2\theta < 44°$.

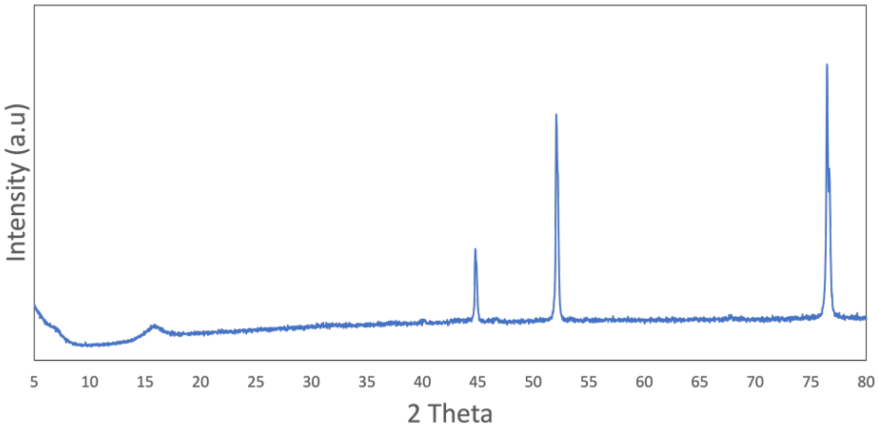

Figure 4.10 X-ray diffraction pattern of a cathode $Bi_{0.03}Na_{0.50}Ni_{0.21}Mn_{0.26}O_x$ deposited on Ni Substrate. Sharp peaks are those of Ni substrate. The broad peak at $2\theta = 16°$ is from the cathode

Figure 4.11 shows typical XRD pattern recorded from the as deposited cathode. Figure 4.11 (a) refers to a sample close to Bi_2O_3 corner of the ternary diagram. The pattern comprises a broad peak centered at 2θ≈28°. Normally Bi_2O_3 have their strongest peaks close to 2θ≈27° and comprises other peaks located at 2θ = 22.7°, 27.9° and 32.3° (pdf card no. 00-027-0052). Therefore, the broad peak at 2θ= 28° is consistent with an amorphous pattern formed by broadening of the Bi_2O_3 peaks. The case close to MnO_2 corner is similar, Figure 4.11 (b). Here there are two broad peaks centered on 2θ≈12.5° (001) and 25° (002). The positions are consistent with δ-MnO_2 which have peaks at 2θ=12.6°, 2θ=25.3° (pdf card no. 01-042-1317). Figure 4.11 (c) refers to a sample close equidistant to Ni and Mn corner. The pattern comprises a small hump at low angles plus a well-defined peak at 2θ≈40.5°. The latter peak is close with that of NiO which normally occurs at 2θ= 43.2° (pdf card no. 00-047-1049).

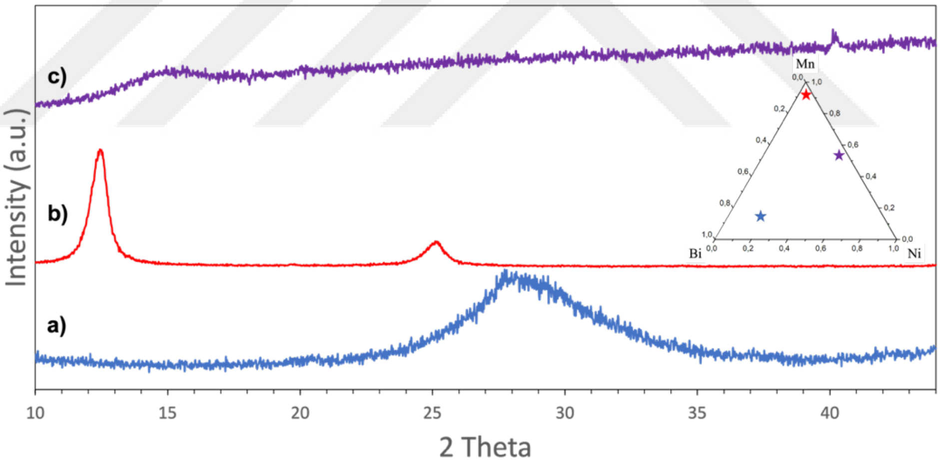

Figure 4.11 Typical XRD pattern of sputtered cathodes **a)** near Bi corner ($Bi_{0.67}Na_{0.02}Ni_{0.17}Mn_{0.13}O_x$), **b)** near Mn corner ($Bi_{0.01}Na_{0.71}Ni_{0.01}Mn_{0.26}O_x$), **c)** equidistant to Ni and Mn corner ($Bi_{0.10}Na_{0.15}Ni_{0.48}Mn_{0.27}O_x$)

After electrochemical testing which involved 50 cycles of charging and discharging, the cells were dismantled, and the cathodes were checked for their structure again using X-ray diffraction. A Typical SEM micrograph of a cathode under low magnifications given in Figure 4.12. It is seen that cathode which was continuous in the as-deposited state were fragmented into islands during cycling, Figure 4.12 (b). Figure 4.13 shows the structure of cycled cathodes at high magnifications.

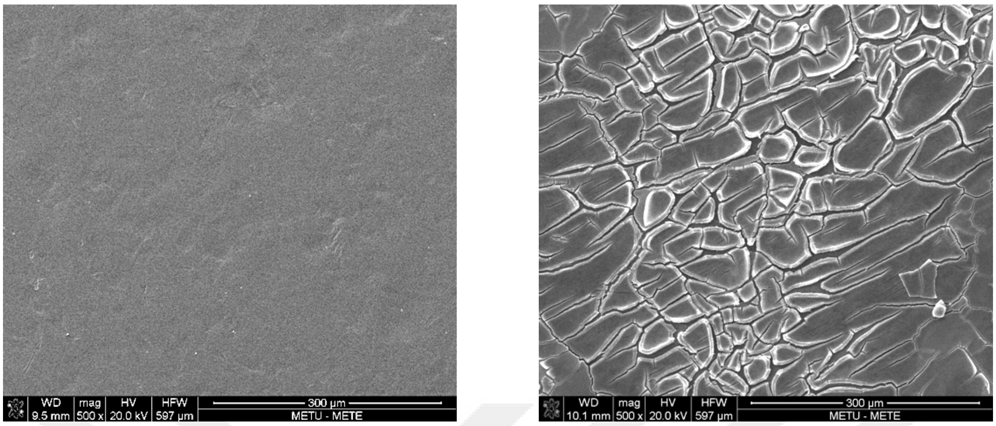

a) **b)**

Figure 4.12 SEM image of a cathode ($Bi_{0.02}Na_{0.71}Ni_{0.02}Mn_{0.24}O_x$) **a)** before cycling, **b)** after cycling

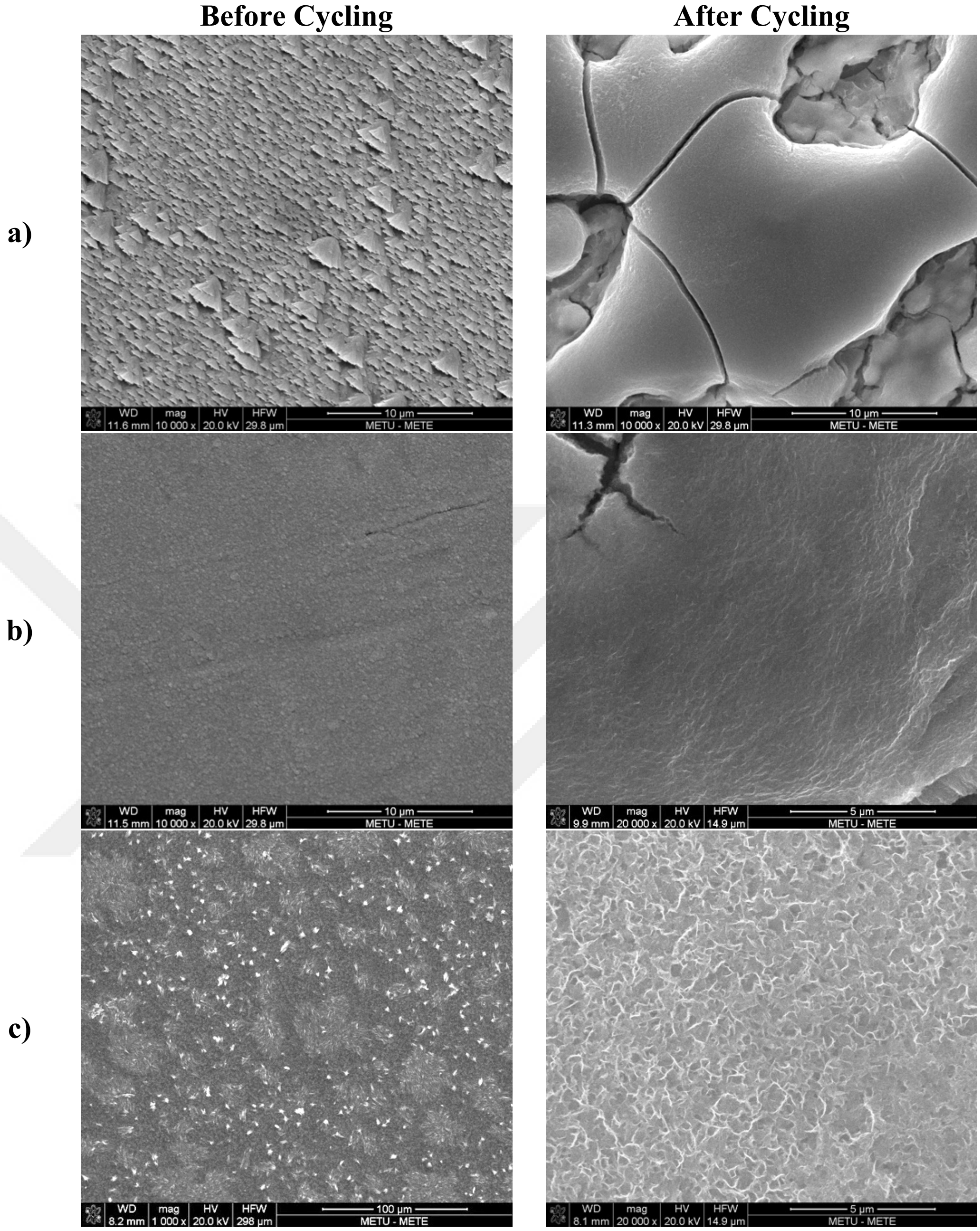

Figure 4.13 Typical characteristic of microstructural change after 50 cycles; **a)** Bi corner ($Bi_{0.39}Na_{0.12}Ni_{0.05}Mn_{0.44}O_x$) **b)** Ni corner ($Bi_{0.06}Na_{0.34}Ni_{0.17}Mn_{0.44}O_x$) **c)** Mn-side ($Bi_{0.01}Na_{0.71}Ni_{0.01}Mn_{0.26}O_x$)

Cycling also lead to changes in the crystal structure. Figure 4.14 shows cathodes with featureless XRD patterns in the as deposited state. As seen in Figure 4.14 (a) there is a slight hump formed at $2\theta=12.5°$. In Figure 4.14 (b) and (c), there is a clear sign of crystallization with well-defined peak(s). Figure 4.14 (d) shows a fully crystallized structure with well-defined peaks. The position of the peaks in the cycled cathode should be compared with a XRD pattern of δ-MnO_2 given in Figure 4.15. It is seen that the peak positions seen in Figure 4.14 do math the positions in δ-MnO_2 which has a layered structure.

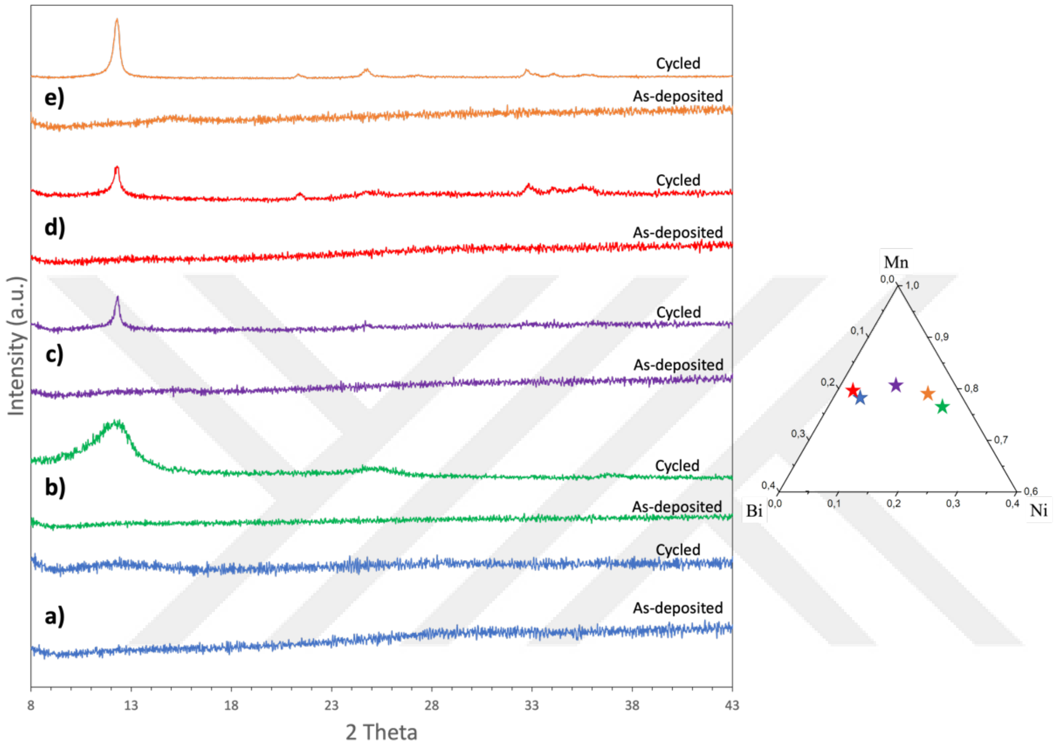

Figure 4.14 XRD pattern of cathodes before and after cycling; **a)** $Bi_{0.09}Na_{0.45}Ni_{0.04}Mn_{0.42}O_x$ **b)** $Bi_{0.04}Na_{0.19}Ni_{0.15}Mn_{0.61}O_x$ **c)** $Bi_{0.04}Na_{0.55}Ni_{0.04}Mn_{0.36}O_x$ **d)** $Bi_{0.07}Na_{0.55}Ni_{0.03}Mn_{0.35}O_x$, **e)** $Bi_{0.03}Na_{0.55}Ni_{0.07}Mn_{0.35}O_x$

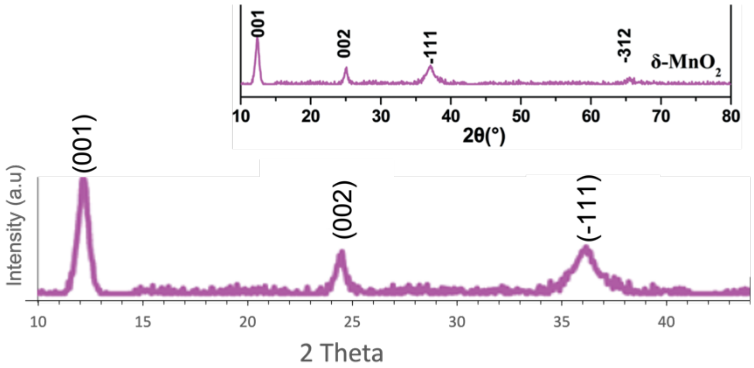

Figure 4.15 XRD pattern of δ-MnO_2 [81]

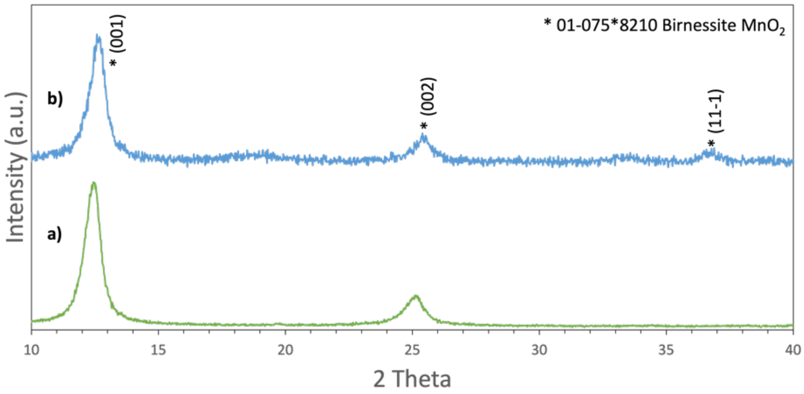

Figure 4.16 XRD pattern of a cathode ($Bi_{0.01}Na_{0.71}Ni_{0.01}Mn_{0.26}O_x$) keeps the crystalline δ-MnO_2 phase; **a)** as-deposited, **b)** after 50 cycles

Similarly, Figure 4.16 refers to a cathode which was crystalline δ-MnO_2 in the as-deposited state and remained crystalline with cycling. There were also cathodes little affected by cycling. Figure 4.17 refers to a sample close to Bi corner where amorphous structure remained amorphous during cycling.

Although great majority of the cathodes after cycling were converted into layered crystalline structure, there were also exceptions. Figure 4.18 refers to an amorphous cathode in the as-deposited state, but after cycling it developed a well-defined crystal structure of ZHS and $Na_4Mn_{12}O_{28}$ which peak positions totally different from those of δ-MnO_2.

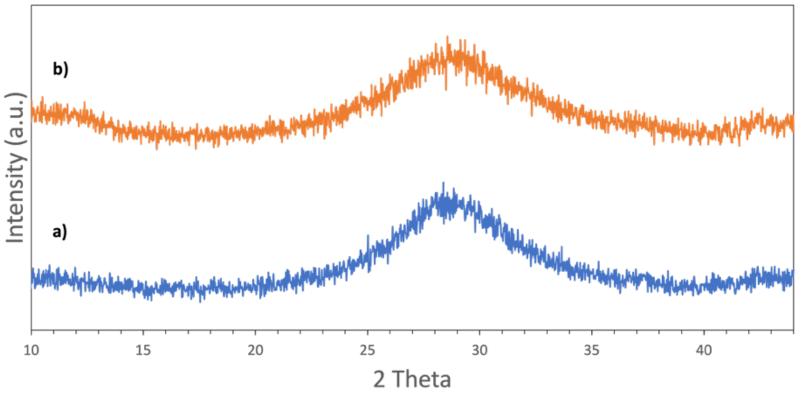

Figure 4.17 Amorphous tendency at Bi side; **a)** as-deposited, **b)** after 50 cycles

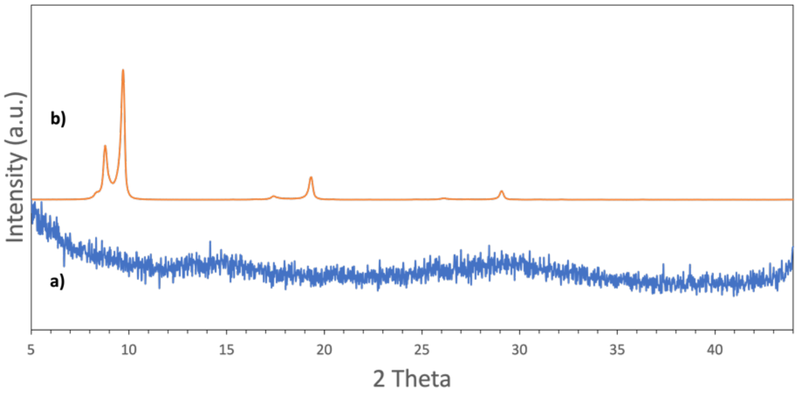

Figure 4.18 Crystallized as sodium manganese oxide hydrate and zinc hydroxide sulfate; **a)** as-deposited, **b)** after 50 cycles

4.3.3 Cyclic Voltammetry

Cyclic voltammetry experiments were carried on a cell where the anode was zinc sheet, and the electrolyte was 2M $ZnSO_4$ and 0.1M $MnSO_4$. Voltammograms were recorded from 1.0 V to 2.0 V with a sweep rate of 2 mV/sec.

Typical examples are reported in Figure 4.19. The first curve refers to a bismuth rich cathode $Bi_{0.45}Na_{0.11}Ni_{0.04}Mn_{0.40}O_x$. The initial curve showed an oxidation peak at 1.7 V, but subsequently the cathode became less active with a general drop in current. Figure 4.19 (b) refers to $Bi_{0.09}Na_{0.45}Ni_{0.04}Mn_{0.42}O_x$. Here in the first cycle, there is an oxidation peak at 1.707 V and a shoulder at 1.802 V and reduction peaks at 1.278 V and 1.137 V. With cycling we see a single oxidation peak at 1.729 V, but this later stabilizes in a broad peak at 1.725 V. With cycling the reduction peaks deepens and stabilizes at 1.127 and 1.265 V. Figure 4.19 (c) refer to a cathode $Bi_{0.01}Na_{0.71}Ni_{0.01}Mn_{0.26}O_x$ which is rich in its Na content. There is a well-defined a single oxidation peak at 1.689 V and a well-defined reduction peak 1.218 V.

A voltammogram similar to Figure 4.19 (b) is given in Figure 4.20 (a). Here with cycling oxidation peaks move to higher voltages and reduction peaks does opposite and move to lower voltages with the result that rechargeability is adversely affected.

A voltammogram similar to that given above is given in Figure 4.20 (b). Here with cycling results in favorable change in peak positions. Accordingly, the oxidation peaks move to lower voltages and reduction peaks move to higher voltages with the net result that the voltage difference decreases with cycling.

The peak positions for oxidation and reduction varies with compositions. The values after 10th cycle in Mn rich samples are tabulated in Table 4.3.

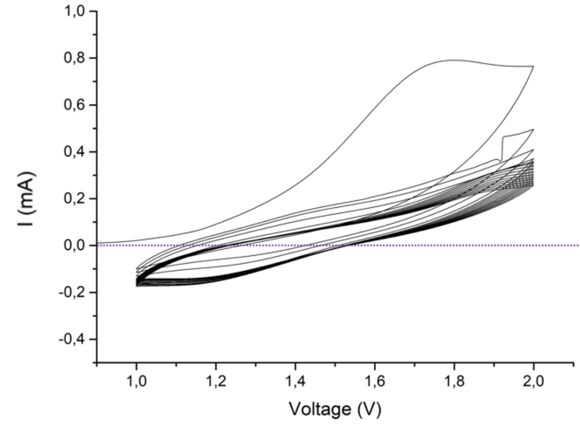

a) $Bi_{0.45}Na_{0.11}Ni_{0.04}Mn_{0.40}O_x$

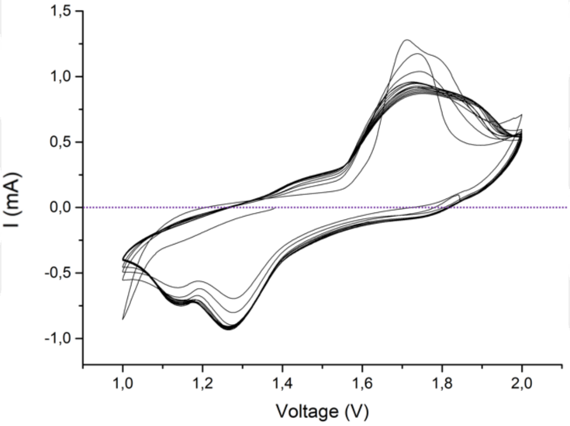

b) $Bi_{0.09}Na_{0.45}Ni_{0.04}Mn_{0.42}O_x$

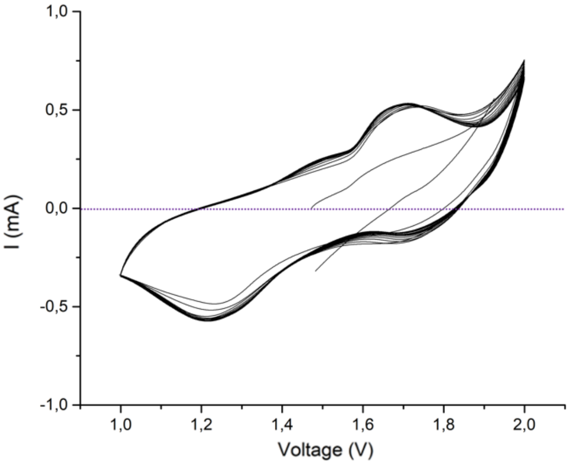

c) $Bi_{0.01}Na_{0.71}Ni_{0.01}Mn_{0.26}O_x$

Figure 4.19 Typical examples of cyclic voltammograms in MnO_2 based cathodes **a)** $Bi_{0.45}Na_{0.11}Ni_{0.04}Mn_{0.40}O_x$, **b)** $Bi_{0.09}Na_{0.45}Ni_{0.04}Mn_{0.42}O_x$, **c)** $Bi_{0.01}Na_{0.71}Ni_{0.01}Mn_{0.26}O_x$

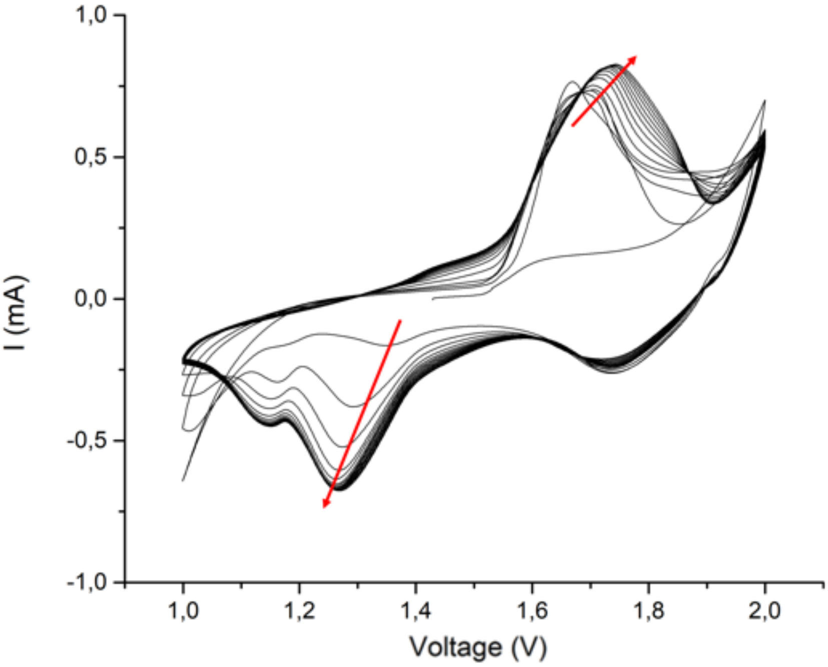

a)

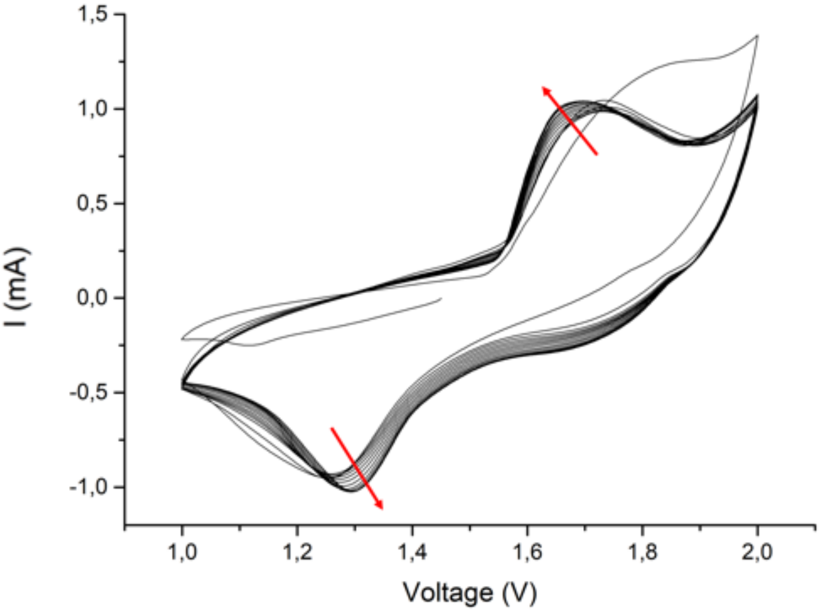

b)

Figure 4.20 Typical CV profile of as-deposited cathodes **a)** increasing redox potential, **b)** decreasing redox potential

Table 4.3 List of cathodes with their oxidation and reduction peaks voltages

Cathode Compositions	Oxidation Peak (V)	Reduction Peak (V)	Voltage Difference
$Bi_{0.03}Na_{0.50}Ni_{0.21}Mn_{0.26}$	1.6873	1.31531	0.37199
$Bi_{0.02}Na_{0.47}Ni_{0.28}Mn_{0.23}$	1.85051	1.22081	0.6297
$Bi_{0.03}Na_{0.47}Ni_{0.22}Mn_{0.27}$	1.74123	1.27613	0.4651
$Bi_{0.04}Na_{0.38}Ni_{0.36}Mn_{0.22}$	1.76547	1.22146	0.54401
$Bi_{0.11}Na_{0.31}Ni_{0.31}Mn_{0.28}$	1.75856	1.27922	0.47934
$Bi_{0.08}Na_{0.31}Ni_{0.35}Mn_{0.26}$	1.70428	1.29392	0.41036
$Bi_{0.05}Na_{0.21}Ni_{0.53}Mn_{0.22}$	1.72379	1.2671	0.45669
$Bi_{0.18}Na_{0.14}Ni_{0.38}Mn_{0.30}$	1.80102	1.25409	0.54693
$Bi_{0.02}Na_{0.13}Ni_{0.65}Mn_{0.20}$	1.70723	1.27421	0.43302
$Bi_{0.27}Na_{0.09}Ni_{0.36}Mn_{0.28}$	1.79917	1.26747	0.5317
$Bi_{0.15}Na_{0.09}Ni_{0.47}Mn_{0.29}$	1.74472	1.28259	0.46213
$Bi_{0.11}Na_{0.07}Ni_{0.58}Mn_{0.25}$	1.69132	1.29526	0.39606
$Bi_{0.07}Na_{0.04}Ni_{0.68}Mn_{0.21}$	1.71325	1.28519	0.42806
$Bi_{0.03}Na_{0.03}Ni_{0.77}Mn_{0.16}$	1.71118	1.26518	0.446
$Bi_{0.30}Na_{0.04}Ni_{0.42}Mn_{0.25}$	1.6863	1.26557	0.42073
$Bi_{0.22}Na_{0.05}Ni_{0.48}Mn_{0.25}$	1.7605	1.27192	0.48858
$Bi_{0.13}Na_{0.08}Ni_{0.56}Mn_{0.23}$	1.7185	1.28661	0.43189
$Bi_{0.04}Ni_{0.81}Mn_{0.15}$	1.70522	1.26922	0.436
$Bi_{0.67}Na_{0.02}Ni_{0.17}Mn_{0.13}$	1.7253	1.2862	0.4391
$Bi_{0.34}Na_{0.03}Ni_{0.43}Mn_{0.21}$	1.82188	1.22686	0.59502
$Bi_{0.20}Na_{0.03}Ni_{0.52}Mn_{0.24}$	1.74724	1.27586	0.47138
$Bi_{0.11}Na_{0.01}Ni_{0.68}Mn_{0.20}$	1.71865	1.28753	0.43112
$Bi_{0.01}Na_{0.02}Ni_{0.88}Mn_{0.09}$	1.74278	1.29722	0.44556
$Bi_{0.02}Na_{0.72}Ni_{0.02}Mn_{0.24}O_x$	1.70771	1.28443	0.42328
$Bi_{0.03}Na_{0.63}Ni_{0.03}Mn_{0.31}O_x$	1.65626	1.28909	0.36717
$Bi_{0.03}Na_{0.62}Ni_{0.04}Mn_{0.31}O_x$	1.71036	1.27779	0.43257
$Bi_{0.03}Na_{0.63}Ni_{0.05}Mn_{0.30}O_x$	1.71177	1.24007	0.4717
$Bi_{0.05}Na_{0.54}Ni_{0.04}Mn_{0.37}O_x$	1.7316	1.26062	0.47098
$Bi_{0.04}Na_{0.55}Ni_{0.04}Mn_{0.36}O_x$	1.72349	1.27585	0.44764
$Bi_{0.04}Na_{0.56}Ni_{0.05}Mn_{0.35}O_x$	1.70764	1.27071	0.43693
$Bi_{0.03}Na_{0.55}Ni_{0.07}Mn_{0.35}O_x$	1.7034	1.27136	0.43204
$Bi_{0.09}Na_{0.45}Ni_{0.04}Mn_{0.42}O_x$	1.74223	1.26388	0.47835

Table 4.3 (cont’d)

$Bi_{0.06}Na_{0.49}Ni_{0.05}Mn_{0.40}O_x$	1.7315	1.27902	0.45248
$Bi_{0.04}Na_{0.49}Ni_{0.08}Mn_{0.39}O_x$	1.7184	1.2659	0.4525
$Bi_{0.25}Na_{0.24}Ni_{0.05}Mn_{0.46}O_x$	1.816	1.25368	0.56232
$Bi_{0.12}Na_{0.35}Ni_{0.06}Mn_{0.47}O_x$	1.88731	1.2153	0.67201
$Bi_{0.08}Na_{0.39}Ni_{0.07}Mn_{0.46}O_x$	1.7506	1.26915	0.48145
$Bi_{0.06}Na_{0.40}Ni_{0.09}Mn_{0.45}O_x$	1.70913	1.2881	0.42103
$Bi_{0.05}Na_{0.39}Ni_{0.12}Mn_{0.44}O_x$	1.72556	1.28001	0.44555
$Bi_{0.04}Na_{0.38}Ni_{0.16}Mn_{0.41}O_x$	1.78305	1.27675	0.5063
$Bi_{0.14}Na_{0.30}Ni_{0.07}Mn_{0.49}O_x$	1.81173	1.27771	0.53402
$Bi_{0.08}Na_{0.36}Ni_{0.10}Mn_{0.47}O_x$	1.8294	1.2887	0.5407
$Bi_{0.07}Na_{0.36}Ni_{0.12}Mn_{0.45}O_x$	1.70481	1.27983	0.42498
$Bi_{0.04}Na_{0.33}Ni_{0.22}Mn_{0.40}O_x$	1.77691	1.29086	0.48605
$Bi_{0.01}Na_{0.71}Ni_{0.01}Mn_{0.26}O_x$	1.70804	1.21641	0.49163
$Bi_{0.02}Na_{0.64}Ni_{0.02}Mn_{0.32}O_x$	1.73593	1.24059	0.49534
$Bi_{0.02}Na_{0.63}Ni_{0.02}Mn_{0.33}O_x$	1.78829	1.23500	0.55329
$Bi_{0.03}Na_{0.56}Ni_{0.02}Mn_{0.39}O_x$	1.74467	1.25906	0.48561
$Bi_{0.03}Na_{0.54}Ni_{0.03}Mn_{0.40}O_x$	1.73215	1.26585	0.4663
$Bi_{0.05}Na_{0.46}Ni_{0.03}Mn_{0.47}O_x$	1.77275	1.24851	0.52424
$Bi_{0.03}Na_{0.46}Ni_{0.04}Mn_{0.46}O_x$	1.7131	1.27942	0.43368
$Bi_{0.07}Na_{0.40}Ni_{0.03}Mn_{0.51}O_x$	1.77381	1.26059	0.51322
$Bi_{0.05}Na_{0.39}Ni_{0.03}Mn_{0.53}O_x$	1.7875	1.20874	0.57876
$Bi_{0.05}Na_{0.37}Ni_{0.04}Mn_{0.54}O_x$	1.66999	1.25763	0.41236
$Bi_{0.04}Na_{0.39}Ni_{0.05}Mn_{0.53}O_x$	1.7408	1.26463	0.47617
$Bi_{0.04}Na_{0.37}Ni_{0.06}Mn_{0.53}O_x$	1.72959	1.26411	0.46548
$Bi_{0.09}Na_{0.29}Ni_{0.04}Mn_{0.58}O_x$	1.79196	1.25556	0.5364
$Bi_{0.04}Na_{0.30}Ni_{0.09}Mn_{0.57}O_x$	1.72166	1.26862	0.45304
$Bi_{0.07}Na_{0.28}Ni_{0.04}Mn_{0.61}O_x$	1.71245	1.25338	0.45907
$Bi_{0.05}Na_{0.27}Ni_{0.06}Mn_{0.61}O_x$	1.73492	1.25797	0.47695
$Bi_{0.04}Na_{0.27}Ni_{0.10}Mn_{0.59}O_x$	1.73232	1.25183	0.48049
$Bi_{0.15}Na_{0.18}Ni_{0.04}Mn_{0.62}O_x$	1.84281	1.26442	0.57839
$Bi_{0.08}Na_{0.23}Ni_{0.06}Mn_{0.63}O_x$	1.73434	1.25227	0.48207
$Bi_{0.06}Na_{0.24}Ni_{0.08}Mn_{0.62}O_x$	1.77157	1.26958	0.50199
$Bi_{0.05}Na_{0.26}Ni_{0.11}Mn_{0.59}O_x$	1.71163	1.27081	0.44082
$Bi_{0.04}Na_{0.19}Ni_{0.15}Mn_{0.61}O_x$	1.70922	1.27089	0.43833

4.3.4 Galvanostatic Charge/Discharge Performance

Voltage profile during charging and discharging varied quite significantly from sample to sample. Some samples did not have a plateau at all. Figure 4.21 gives an example which refers to $Bi_{0.04}Na_{0.44}Ni_{0.03}Mn_{0.49}O_x$ where charge and discharge profiles are sampled up to 50th cycle.

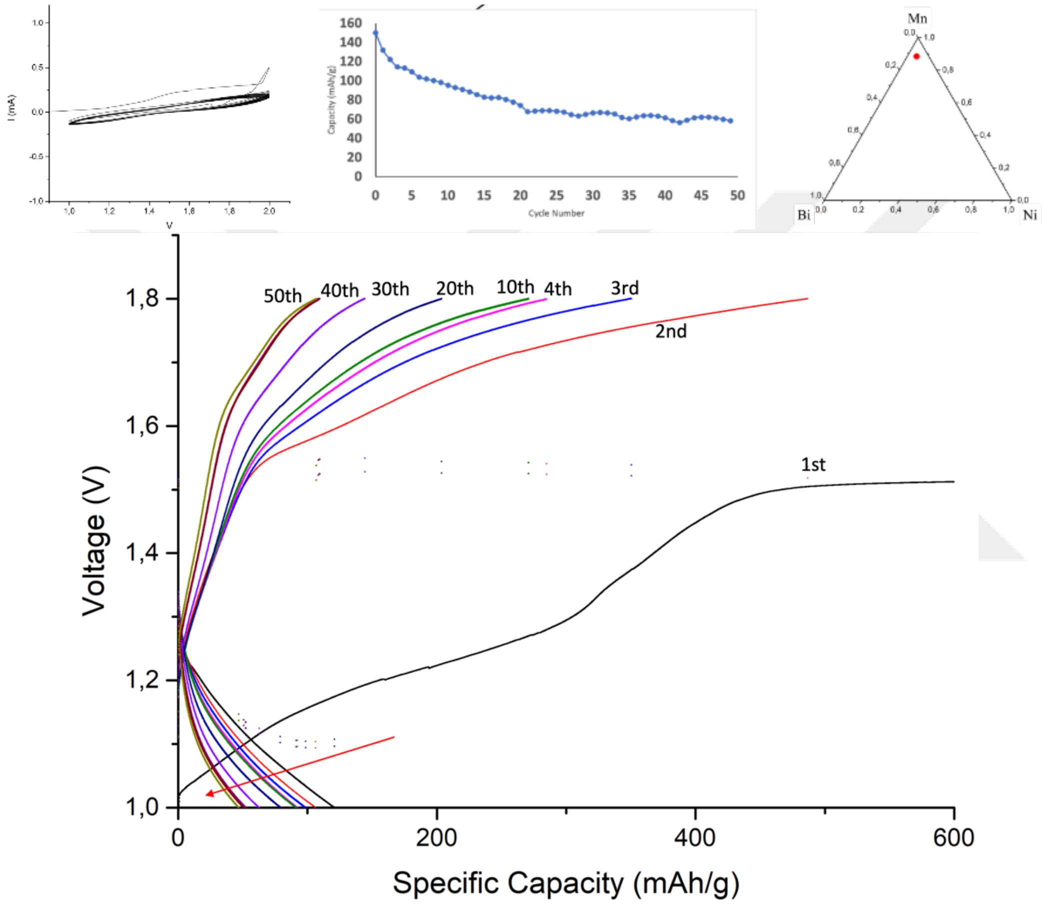

Figure 4.21 Charge-discharge profiles of $Bi_{0.04}Na_{0.44}Ni_{0.03}Mn_{0.49}O_x$. Note that there is no plateau formation in the profiles

Figure 4.22 refers to $Bi_{0.08}Na_{0.39}Ni_{0.07}Mn_{0.46}O_x$ where defined plateau both in charge and in discharge can be seen in the initial cycles. There seems to be two plateau like regions in the discharge curve with turning points at 1. 43 and 1.31 V. However, after 10^{th} cycle all disappear and charge and discharge curves are without plateau.

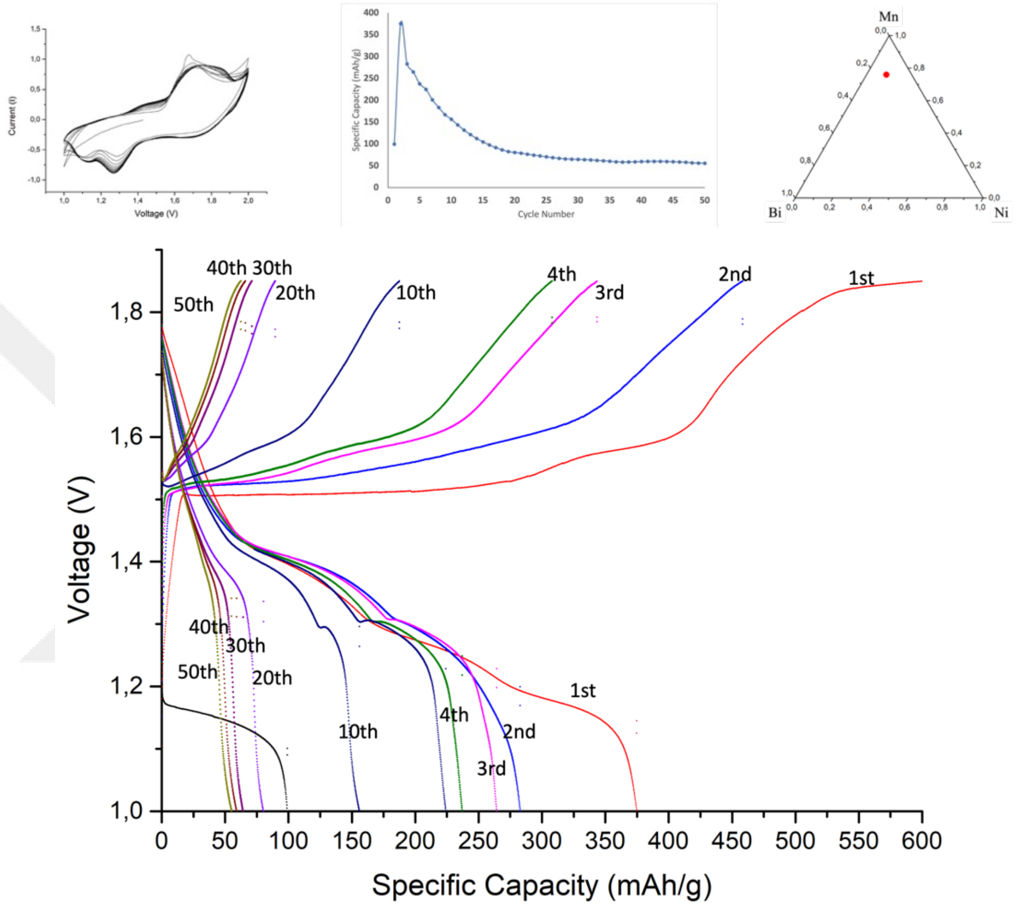

Figure 4.22 Charge-discharge profiles of $Bi_{0.08}Na_{0.39}Ni_{0.07}Mn_{0.46}O_x$. Note that there is a plateau formation with a turning point at 1.3 V in the profiles.

Figure 4.23 is an example where there are three plateau like regions in the discharge curve. These curves refer to $Bi_{0.05}Na_{0.39}Ni_{0.12}Mn_{0.44}O_x$. Transition occurs at 1.39, 1.24 and 1.10 V. After 5^{th} cycle third turning point disappears as a result there are two plateaus. This is reduced to a single plateau after 20^{th} cycle.

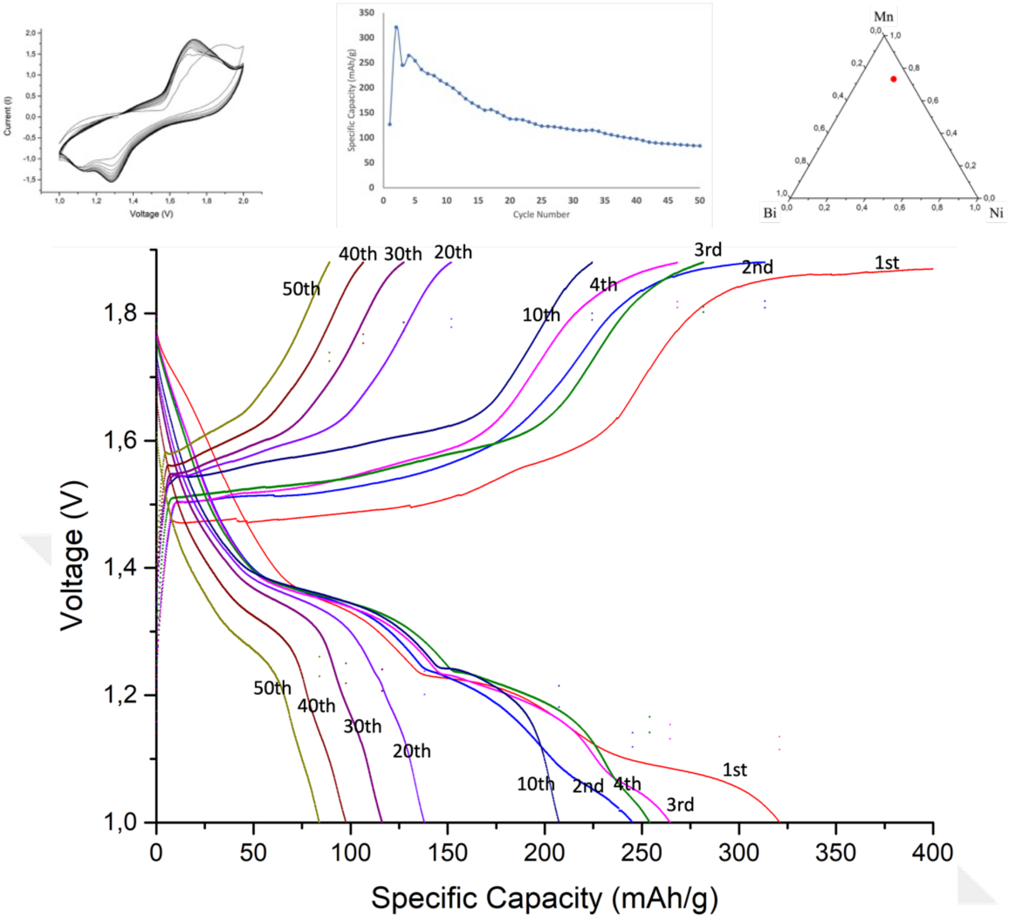

Figure 4.23 Charge-discharge profiles of $Bi_{0.05}Na_{0.39}Ni_{0.12}Mn_{0.44}O_x$. Note that there is a plateau formation with a turning point at 1.3 and 1.1 V in the profiles

Discharge capacities varied from cathode to cathode quite significantly. In some cathodes the capacity increased with cycling. An example for this is given Figure 4.24. The capacity which was 99 mAh/g in the first cycle then increased to 136 mAh/g and then to 152 mAh/g in 20th and 50th cycles respectively.

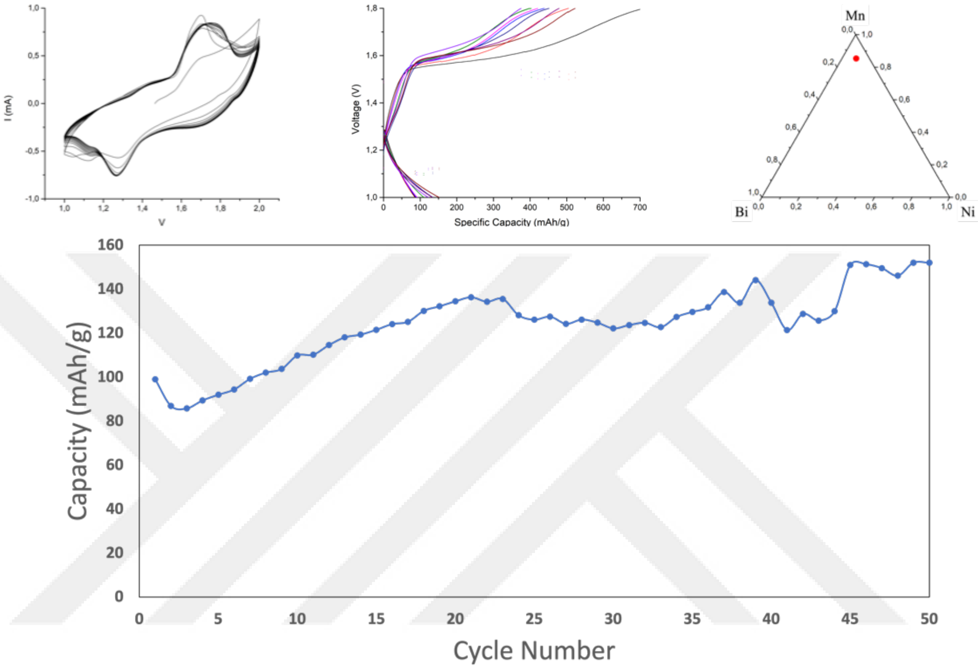

Figure 4.24 Discharge capacity versus cycle number for $Bi_{0.03}Na_{0.54}Ni_{0.03}Mn_{0.40}O_x$. Note that the capacity increases with increase cycle number

Figure 4.25 refers to $Bi_{0.04}Na_{0.33}Ni_{0.22}Mn_{0.40}O_x$ cathode. Here the capacity initially is quite high but reduces with cycling. Here the value of initial capacity which was calculated more than 1400 mAh/g need to be confirmed, but the value after 50 cycle is 294 mAh/g.

Figure 4.26 refers to an example where the capacity remains almost the same with cycling. The figure refers to $Bi_{0.23}Na_{0.21}Ni_{0.06}Mn_{0.50}O_x$. The capacity in the first cycle is 106 mAh/g and the capacity in the 50th cycle is slightly more with a value of 126 mAh/g.

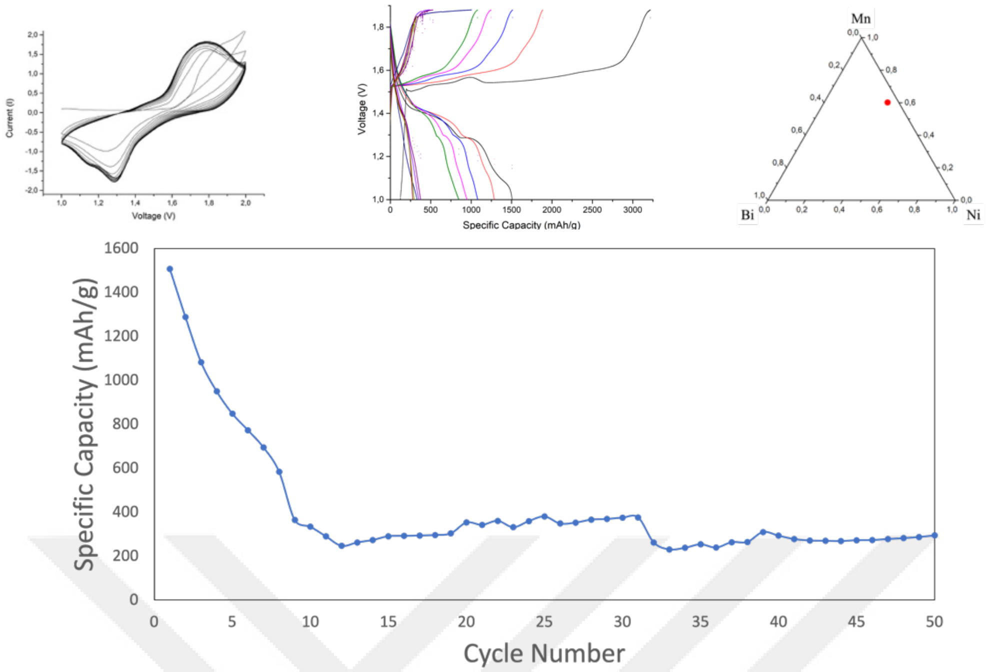

Figure 4.25 Discharge capacity versus cycle number for $Bi_{0.04}Na_{0.33}Ni_{0.22}Mn_{0.40}O_x$. The capacity stabilizes at 200 mAh/g after 10th cycle

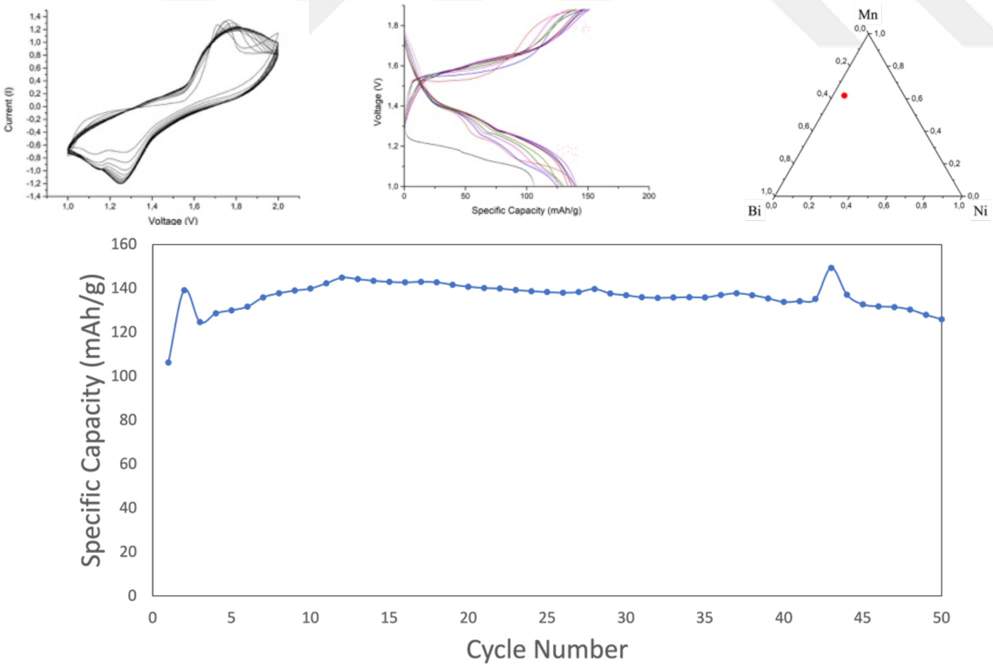

Figure 4.26 Discharge capacity versus cycle number in $Bi_{0.23}Na_{0.21}Ni_{0.06}Mn_{0.50}O_x$ which has a stable specific capacity at 130 mAh/g for 50 cycles

It may be pointed out that in some cells the capacity was reduced drastically with no prior sign in discharge curve. Figure 4.27 is an example for this. Here the cell $Bi_{0.11}Na_{0.31}Ni_{0.31}Mn_{0.28}O_x$ with capacities in the order of 500 mAh/g drops suddenly to 300 mAh/g at 11th cycle. This is probably due to contact problems in the cell as in the previous cycle there are irregularities in the charge curve.

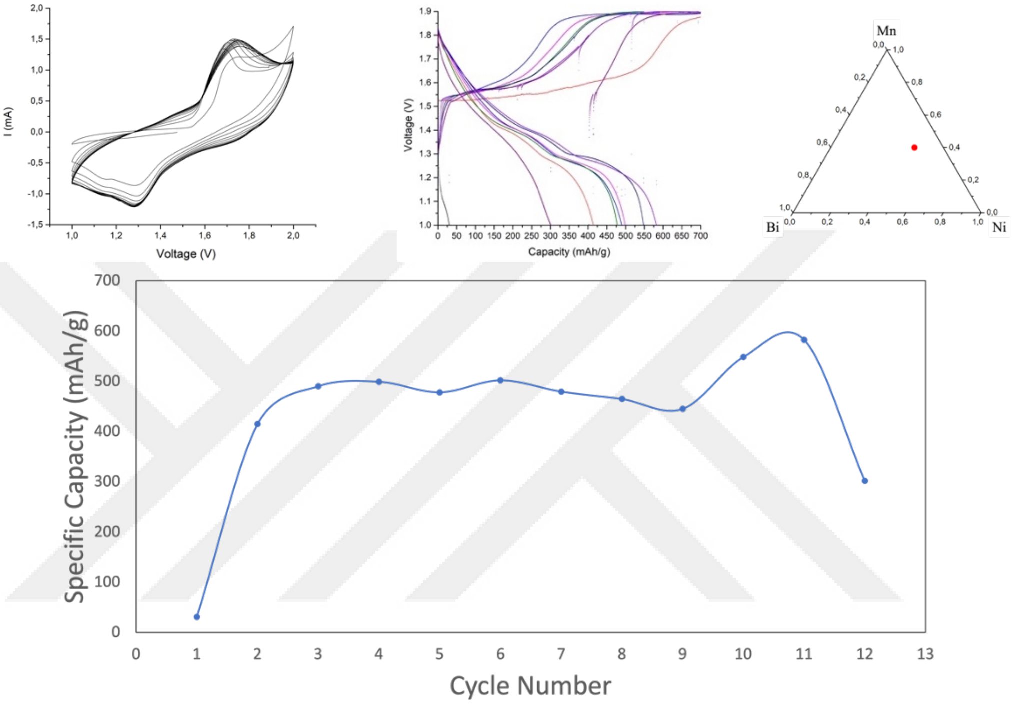

Figure 4.27 Discharge capacity versus cycle number for $Bi_{0.11}Na_{0.31}Ni_{0.31}Mn_{0.28}O_x$ which has a sudden drop in capacity after 11th cycle

4.3.5 Selection of candidate cathode compositions

Results reported above indicates that capacities are quite high in Mn rich compositions. For this reason, cathodes rich in Mn content was examined in more detail. All cells were thoroughly examined and data concerning discharge capacity of initial, maximum, average, and the final are determined. These values which covers total of 57 cathodes are tabulated in Table 4.4. It should be noted that the ternary diagram just covers the Mn rich corner of the complete ternary given in Figure 4.28. It covers Mn content from 0.65 up to 0.90.

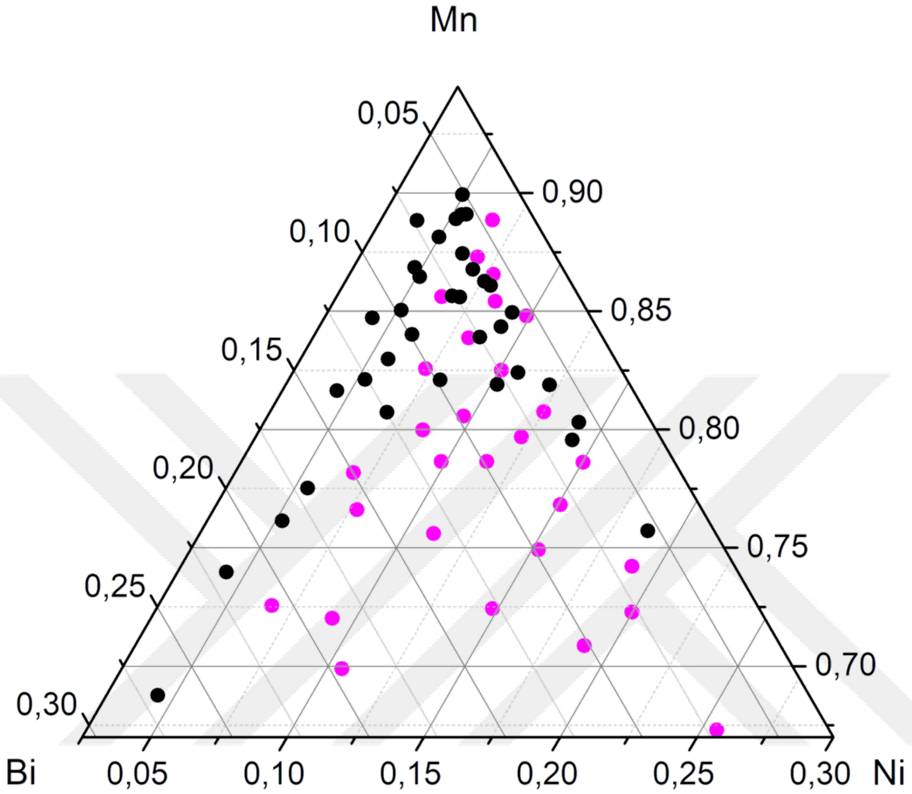

Figure 4.28 Mn-rich cathodes on Bi-Mn-Ni space

Table 4.4 Discharge capacities of the cathodes in (Bi,Na,Ni,Mn)O_x

Cathode Compositions	**Initial Discharge Capacity (mAh/g)**	**Maximum Discharge Capacity (mAh/g)**	**Average Discharge Capacity (mAh/g)**	**Final Discharge Capacity (mAh/g)**
$Bi_{0.01}Na_{0.78}Ni_{0.01}Mn_{0.20}O_x$	151	151	113	137
$Bi_{0.01}Na_{0.75}Ni_{0.02}Mn_{0.22}O_x$	101	182	111	102
$Bi_{0.01}Na_{0.76}Ni_{0.02}Mn_{0.21}O_x$	53	272	98	80
$Bi_{0.02}Na_{0.71}Ni_{0.02}Mn_{0.24}O_x$	39	382	153	137
$Bi_{0.02}Na_{0.72}Ni_{0.02}Mn_{0.24}O_x$	222	222	103	77
$Bi_{0.01}Na_{0.72}Ni_{0.03}Mn_{0.24}O_x$	235	238	144	165
$Bi_{0.04}Na_{0.64}Ni_{0.03}Mn_{0.29}O_x$	765	765	259	201
$Bi_{0.03}Na_{0.63}Ni_{0.03}Mn_{0.31}O_x$	335	341	180	132
$Bi_{0.03}Na_{0.62}Ni_{0.04}Mn_{0.31}O_x$	222	222	123	92
$Bi_{0.03}Na_{0.63}Ni_{0.05}Mn_{0.30}O_x$	734	734	199	159
$Bi_{0.04}Na_{0.55}Ni_{0.04}Mn_{0.36}O_x$	571	571	393	429
$Bi_{0.04}Na_{0.56}Ni_{0.05}Mn_{0.35}O_x$	361	361	189	201
$Bi_{0.12}Na_{0.43}Ni_{0.04}Mn_{0.42}O_x$	374	374	110	68
$Bi_{0.09}Na_{0.45}Ni_{0.04}Mn_{0.42}O_x$	329	329	177	118
$Bi_{0.04}Na_{0.49}Ni_{0.08}Mn_{0.39}O_x$	47	47	23	17
$Bi_{0.12}Na_{0.35}Ni_{0.06}Mn_{0.47}O_x$	968	968	381	230
$Bi_{0.08}Na_{0.39}Ni_{0.07}Mn_{0.46}O_x$	374	374	102	55
$Bi_{0.06}Na_{0.40}Ni_{0.09}Mn_{0.45}O_x$	16	16	7	4
$Bi_{0.05}Na_{0.39}Ni_{0.12}Mn_{0.44}O_x$	320	320	143	83
$Bi_{0.04}Na_{0.38}Ni_{0.16}Mn_{0.41}O_x$	446	455	234	141
$Bi_{0.14}Na_{0.30}Ni_{0.07}Mn_{0.49}O_x$	615	618	260	162
$Bi_{0.07}Na_{0.36}Ni_{0.12}Mn_{0.45}O_x$	239	239	156	108
$Bi_{0.06}Na_{0.34}Ni_{0.17}Mn_{0.44}O_x$	244	244	126	66
$Bi_{0.01}Na_{0.71}Ni_{0.01}Mn_{0.26}O_x$	180	228	151	164
$Bi_{0.02}Na_{0.64}Ni_{0.02}Mn_{0.32}O_x$	40	40	7	0.2
$Bi_{0.02}Na_{0.63}Ni_{0.02}Mn_{0.33}O_x$	396	763	538	750
$Bi_{0.03}Na_{0.56}Ni_{0.02}Mn_{0.39}O_x$	423	507	284	507
$Bi_{0.03}Na_{0.54}Ni_{0.03}Mn_{0.40}O_x$	99	151	124	151
$Bi_{0.02}Na_{0.56}Ni_{0.02}Mn_{0.40}O_x$	51	58	43	33
$Bi_{0.04}Na_{0.44}Ni_{0.03}Mn_{0.49}O_x$	120	120	78	46
$Bi_{0.03}Na_{0.45}Ni_{0.04}Mn_{0.47}O_x$	195	195	72	18

Table 4.4 (cont'd)

$Bi_{0.03}Na_{0.46}Ni_{0.04}Mn_{0.46}O_x$	88	172	134	119
$Bi_{0.07}Na_{0.40}Ni_{0.03}Mn_{0.51}O_x$	54	101	79	102
$Bi_{0.05}Na_{0.39}Ni_{0.03}Mn_{0.53}O_x$	398	398	29	97
$Bi_{0.05}Na_{0.37}Ni_{0.04}Mn_{0.54}O_x$	528	528	195	161
$Bi_{0.04}Na_{0.39}Ni_{0.05}Mn_{0.53}O_x$	442	442	151	114
$Bi_{0.04}Na_{0.37}Ni_{0.06}Mn_{0.53}O_x$	282	1282	574	661
$Bi_{0.10}Na_{0.30}Ni_{0.03}Mn_{0.57}O_x$	196	196	41	7
$Bi_{0.09}Na_{0.29}Ni_{0.04}Mn_{0.58}O_x$	403	403	129	81
$Bi_{0.06}Na_{0.36}Ni_{0.03}Mn_{0.54}O_x$	62	62	36	35
$Bi_{0.05}Na_{0.32}Ni_{0.05}Mn_{0.58}O_x$	37	37	25	17
$Bi_{0.04}Na_{0.34}Ni_{0.06}Mn_{0.56}O_x$	39	64	55	64
$Bi_{0.04}Na_{0.30}Ni_{0.09}Mn_{0.57}O_x$	359	359	142	103
$Bi_{0.18}Na_{0.18}Ni_{0.04}Mn_{0.61}O_x$	23	23	6	5
$Bi_{0.13}Na_{0.21}Ni_{0.04}Mn_{0.61}O_x$	32	32	11	9
$Bi_{0.09}Na_{0.25}Ni_{0.04}Mn_{0.63}O_x$	526	526	210	167
$Bi_{0.07}Na_{0.28}Ni_{0.04}Mn_{0.61}O_x$	259	259	104	58
$Bi_{0.05}Na_{0.27}Ni_{0.06}Mn_{0.61}O_x$	89	89	46	34
$Bi_{0.05}Na_{0.25}Ni_{0.08}Mn_{0.62}O_x$	124	188	137	103
$Bi_{0.04}Na_{0.27}Ni_{0.10}Mn_{0.59}O_x$	204	367	236	247
$Bi_{0.24}Na_{0.12}Ni_{0.04}Mn_{0.61}O_x$	157	157	73	37
$Bi_{0.15}Na_{0.18}Ni_{0.04}Mn_{0.62}O_x$	220	220	90	32
$Bi_{0.10}Na_{0.20}Ni_{0.05}Mn_{0.65}O_x$	67	155	75	30
$Bi_{0.08}Na_{0.23}Ni_{0.06}Mn_{0.63}O_x$	99	185	131	164
$Bi_{0.06}Na_{0.24}Ni_{0.08}Mn_{0.62}O_x$	270	270	84	44
$Bi_{0.05}Na_{0.26}Ni_{0.11}Mn_{0.59}O_x$	51	51	40	45
$Bi_{0.04}Na_{0.19}Ni_{0.15}Mn_{0.61}O_x$	283	283	105	73

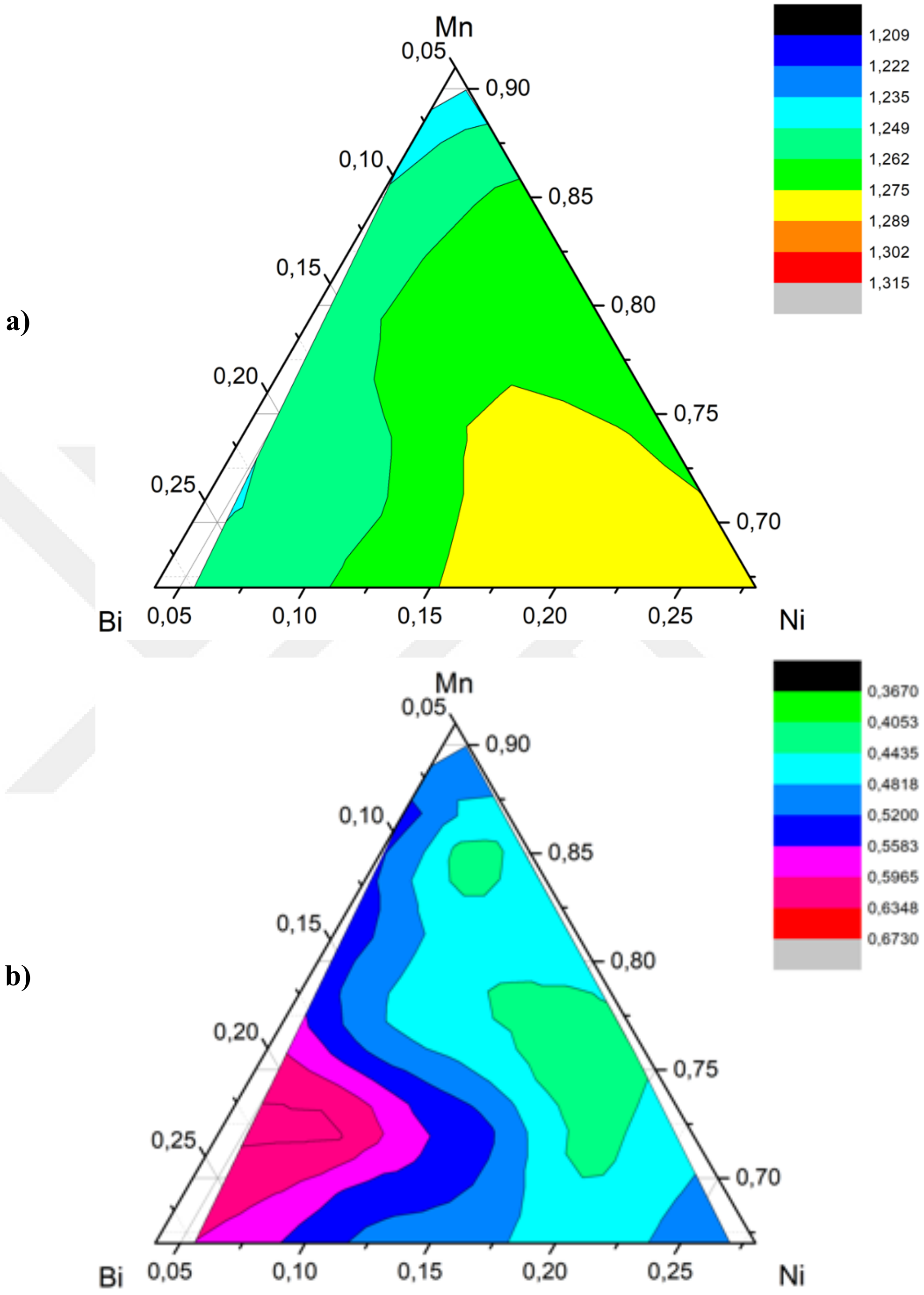

Figure 4.29 Sample distribution on Bi-Mn-Ni ternary diagram; **a)** discharge voltages, **b)** redox potential difference

Figure 4.29 shows maps two maps. The first one refers to discharge voltages as determined from CV (10th cycle), Figure 4.29 (a). The value of this potential is important in terms of the cell power. Figure 4.29 (b) refers to voltage difference between oxidation and reduction peaks in CV again at the 10th cycle, which is a measure of the ease of rechargeability.

Figure 4.30 (a) shows a map of initial discharge capacity for Mn rich cathodes. It should be noted that the initial capacity is highest in $Bi_{0.12}Na_{0.35}Ni_{0.06}Mn_{0.47}O_x$ and $Bi_{0.14}Na_{0.30}Ni_{0.07}Mn_{0.36}O_x$ cathodes marked with yellow and orange contours. This position was marked with “L” in Figure 4.30 (a) The position of their battery performance plotted in Figure 4.32.

Figure 4.30 (b) shows a map of maximum discharge capacity in the cathodes. It is seen that it is in the same region as that in Figure 4.30 (a) where the maximum capacity was observed. Therefore, this position was also marked with L. Highest capacity observed was 968 mAh/g. However, this high capacity decreased with cycle number and stabilized at around 175 mAh/g after 50 cycles.

In terms of galvanostatic performance of cathodes, perhaps most representative map is that of average capacity, i.e., capacity averaged over 50 cycles. Figure 4.31 (a). It is seen that there are three maxima along the line where Ni≈ 0.10. The highest average capacity is obtained in the same position as that marked with L in the maps given above. This cathode has Mn≈0.72. The next positions are two yellow area where Mn content is Mn≈ 0.80 and 0.85 respectively. These marked with M and H1.

Figure 4.31 (b) is most instructive map which gives the final capacities of the cathode. Here the position M which was already marked above shows up very clearly as it is the area with highest final capacity. Here the value is 700 mAh/g. The map also shows up a region in the upper left corner of the ternary diagram. This region is marked with H2.

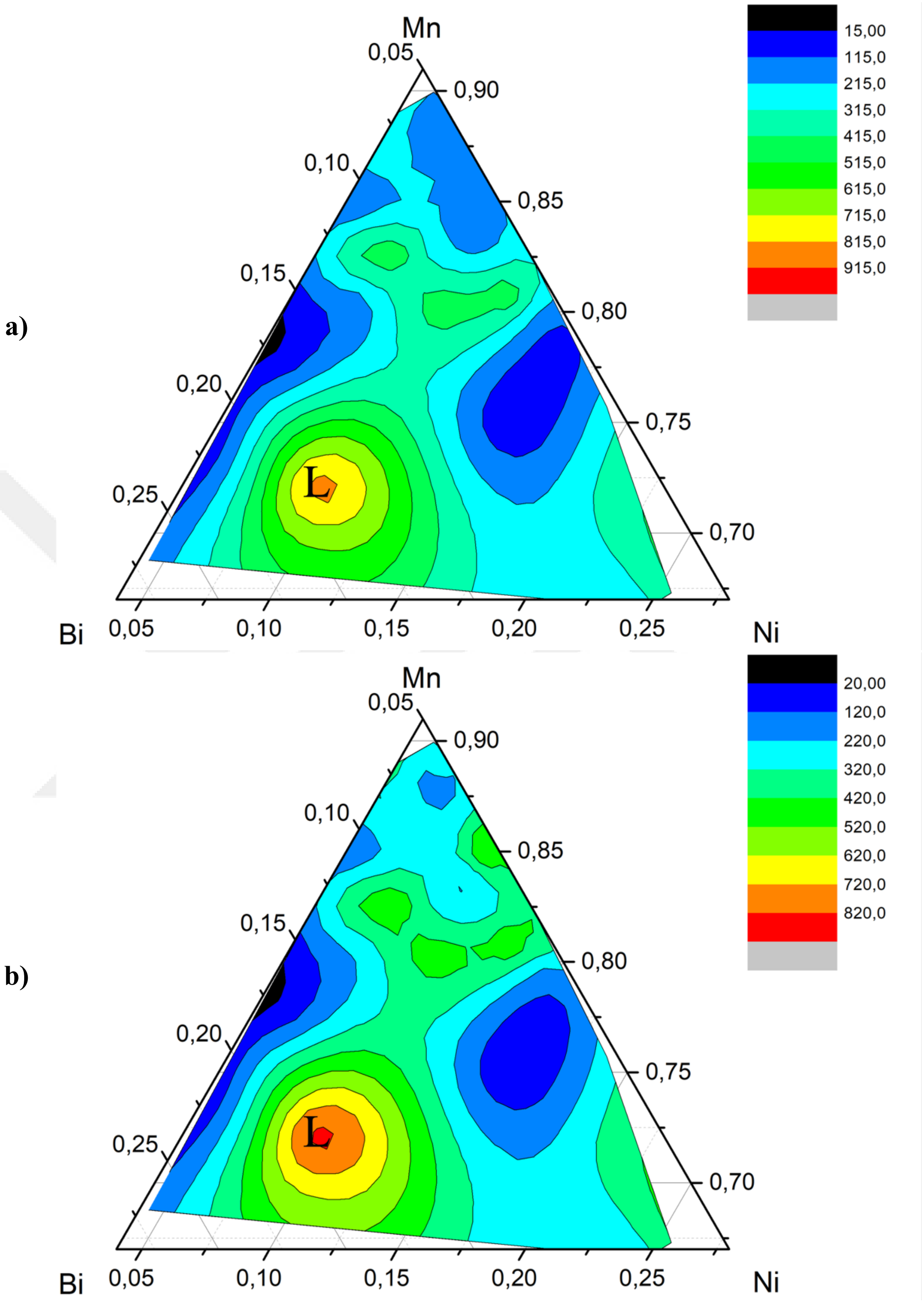

Figure 4.30 Discharge capacities of cathodes; **a)** initial capacity, **b)** maximum capacity. Note that red, orange, and yellow color codes indicate higher capacity

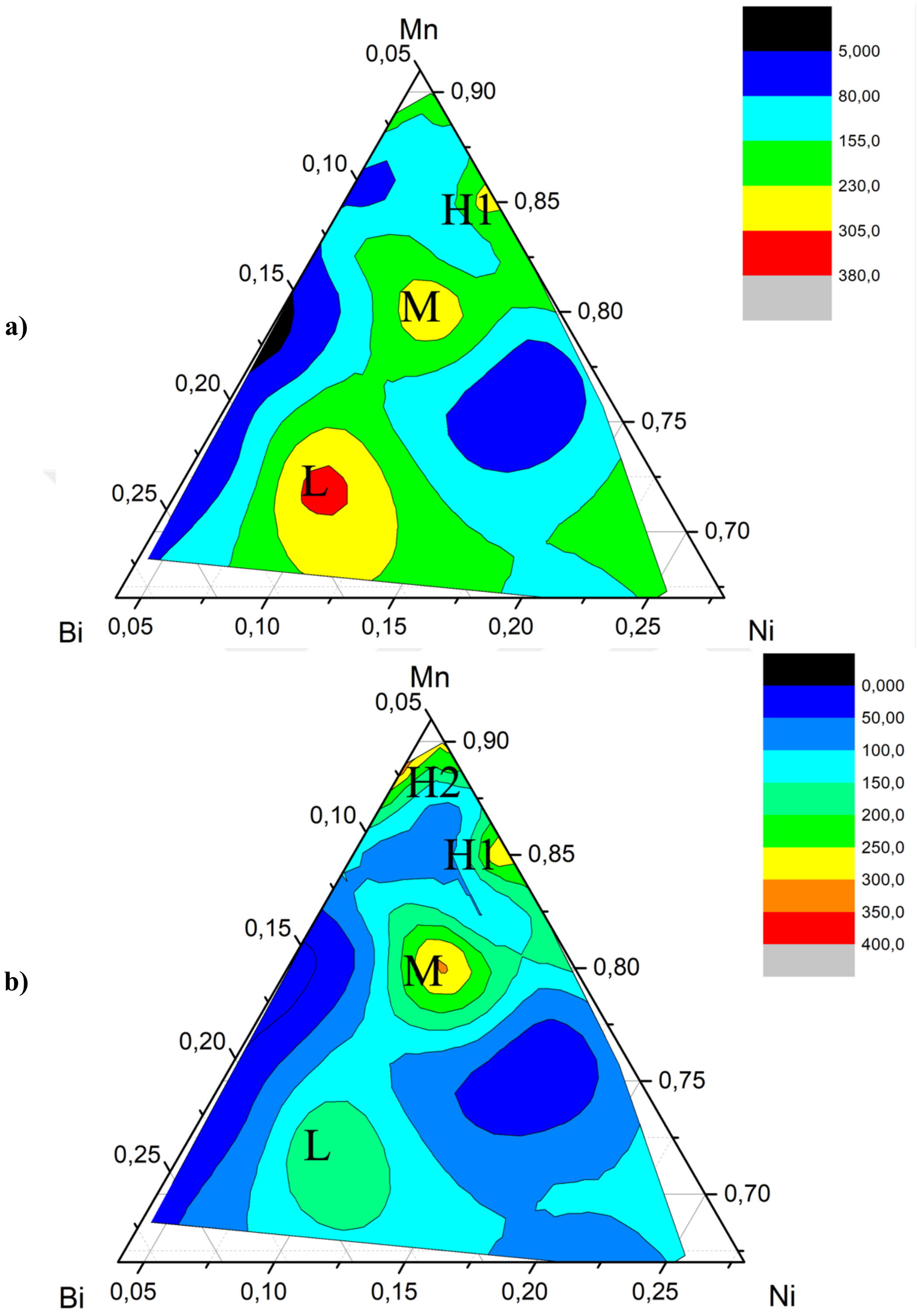

Figure 4.31 Discharge capacities of cathodes; **a)** average capacity, **b)** final capacity. Note that red, orange, and yellow color codes indicate higher capacity

Candidate compositions therefore fall into four regions in the ternary diagram. These are examined in detail below.

Figure 4.32 refers to a representative sample in region L. It is seen that the voltammogram appears to have a single oxidation and two reduction peaks, which with cycling become quite stable. Charge-discharge profile changes quite significantly with cycling with loss of plateaus. The capacity is reduced with cycling and goes down to quite a low value of 162 mAh/g. XRD pattern of the cathode before and after cycling is given in Figure 4.33 where it is seen that the cathode remains amorphous with no sign of crystallization.

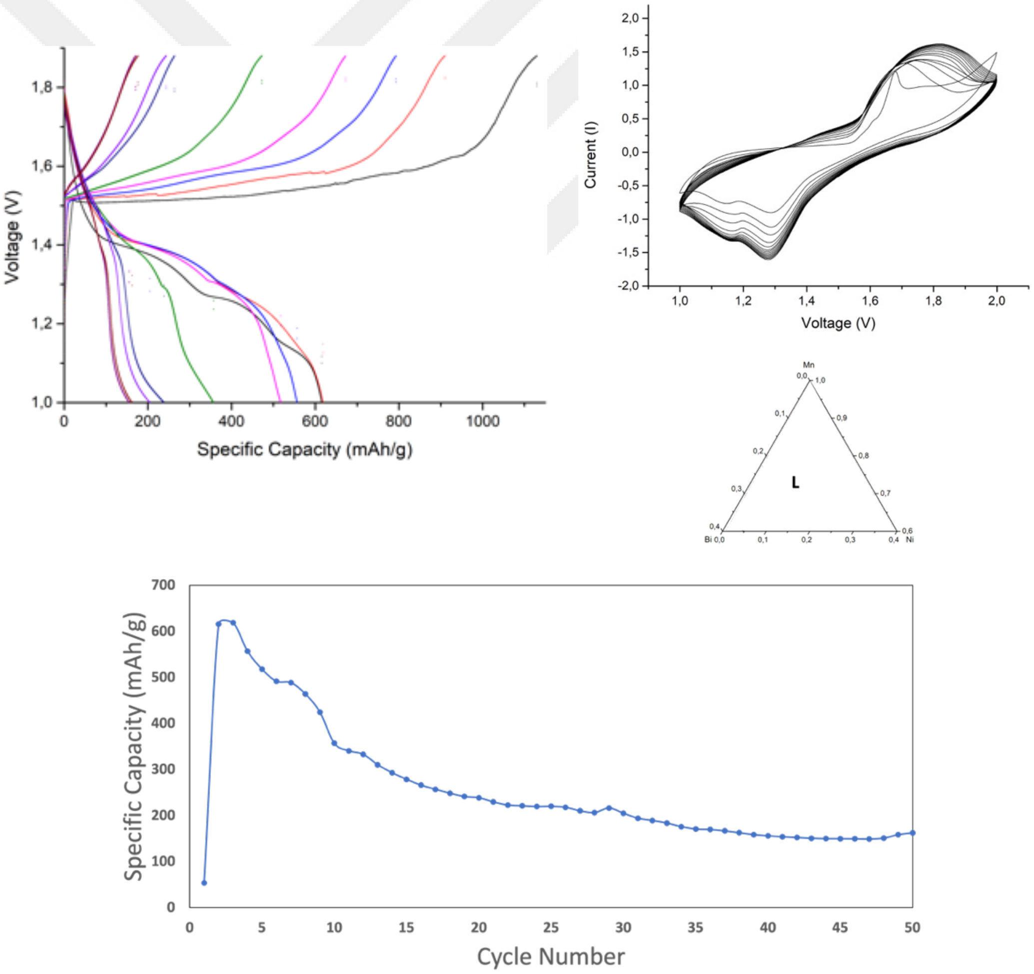

Figure 4.32 Battery performance of the cathode composition of **L** $Bi_{0.14}Na_{0.30}Ni_{0.07}Mn_{0.36}O_x/Bi_{0.20}Na0.{}_{43}Ni_{0.11}Mn_{0.70}O_x$

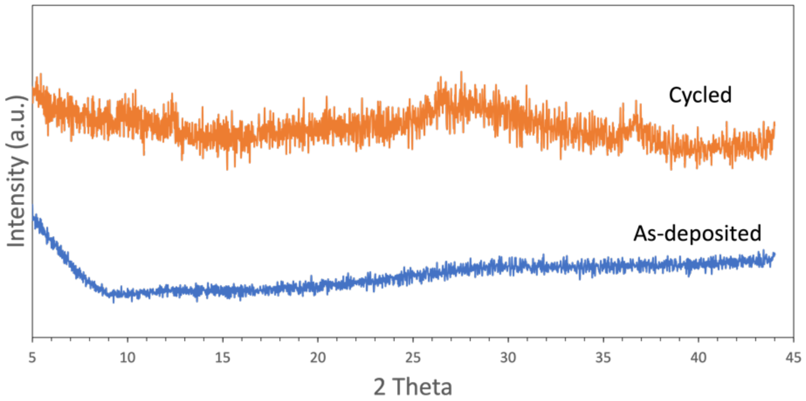

Figure 4.33 XRD pattern of the representative sample from the region **L**, having composition of $Bi_{0.14}Na_{0.30}Ni_{0.07}Mn_{0.36}O_x/Bi_{0.20}Na0._{43}Ni_{0.11}Mn_{0.70}O_x$

Unlike region L, the region M display structural change upon cycling. XRD patterns of a representative sample from this region is given in Figure 4.34 The cathode was amorphous in the as–deposited case but it is crystalline after cycling with peak positions matching δ-MnO_2. The voltammogram is similar to that reported above implying that charge discharge reactions are similar in both region L and M. In terms of capacity, the initial value close 600 mAh/g shows a decrease but stabilizes at an immersive value of 400 mAh/g and remain the same from 15th cycle onwards Figure 4.35.

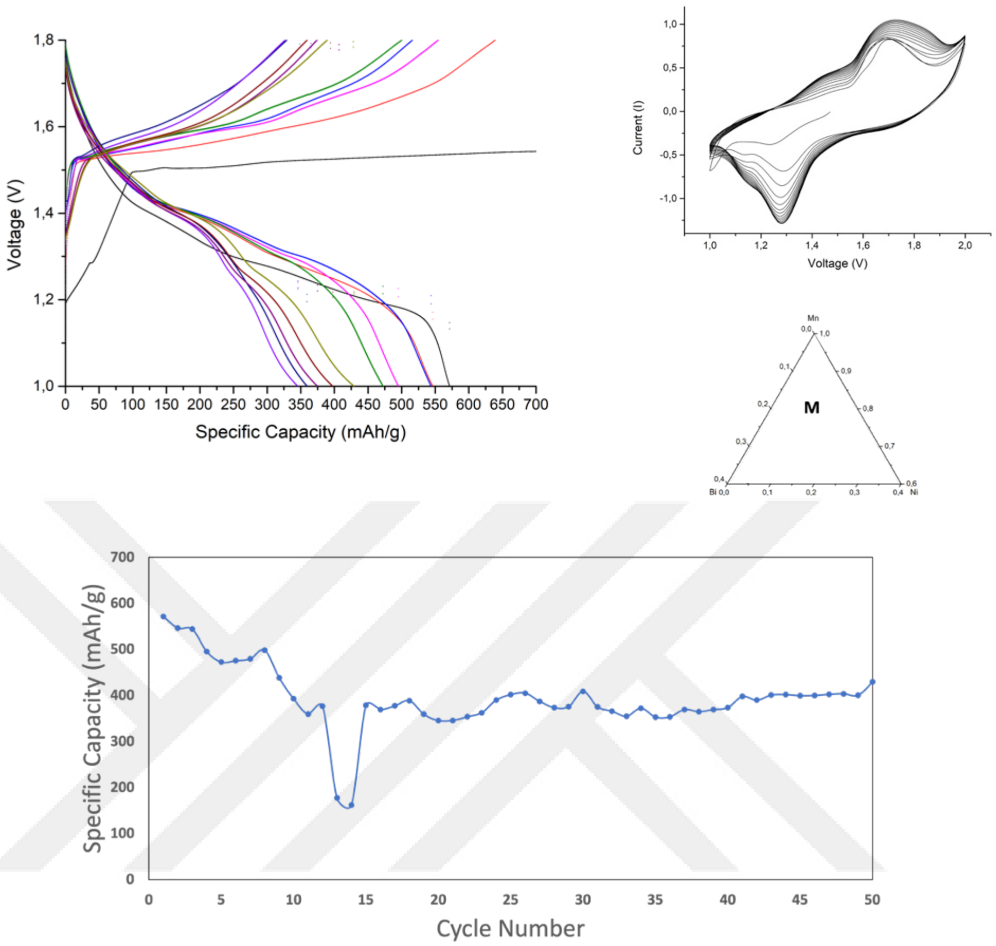

Figure 4.34 Representative battery performance of the **M** region cathodes with the composition of $Bi_{0.04}Na_{0.55}Ni_{0.04}Mn_{0.36}O_x$/$Bi_{0.10}Na_{1.22}Ni_{0.10}Mn_{0.81}O_x$

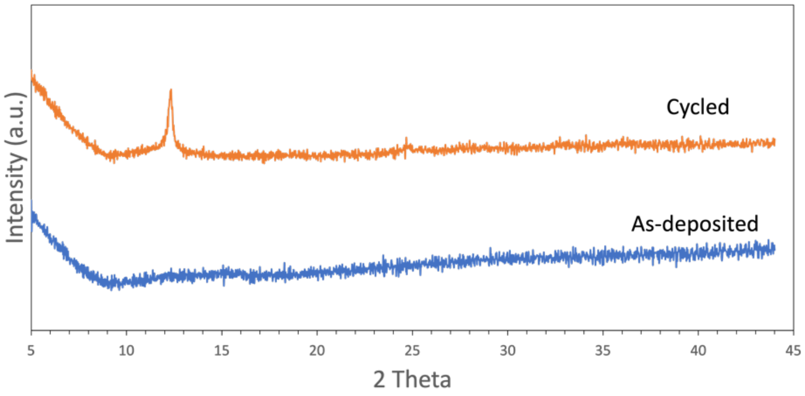

Figure 4.35 XRD pattern of the representative sample from the region **M**, having composition of $Bi_{0.04}Na_{0.55}Ni_{0.04}Mn_{0.36}O_x$/$Bi_{0.10}Na_{1.22}Ni_{0.10}Mn_{0.81}O_x$

The region H1 have features which are quite similar to those of region M, Figure 4.36. The amorphous cathode crystallizes into layered structure of delta MnO_2, but here the peaks are not as sharp as those in region M implying that the cathode is nanocrystalline, Figure 4.37. In capacity versus cycle number curve, there are temporary falls in the capacity which recovers later on, similar sudden drop was also observed in region M. Rate capability of the H1 was impressive which is the discharge capacity is between 400 and 300 mAh/g as increasing the current from 61.6 mA/g to 616 mA/g.

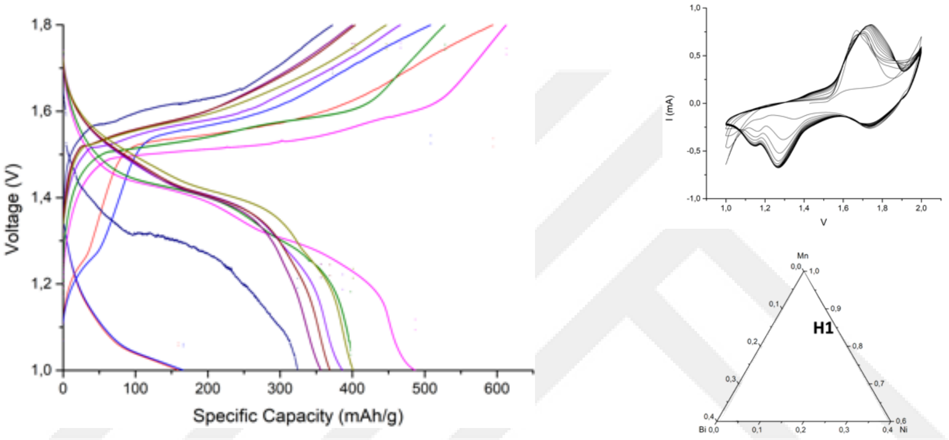

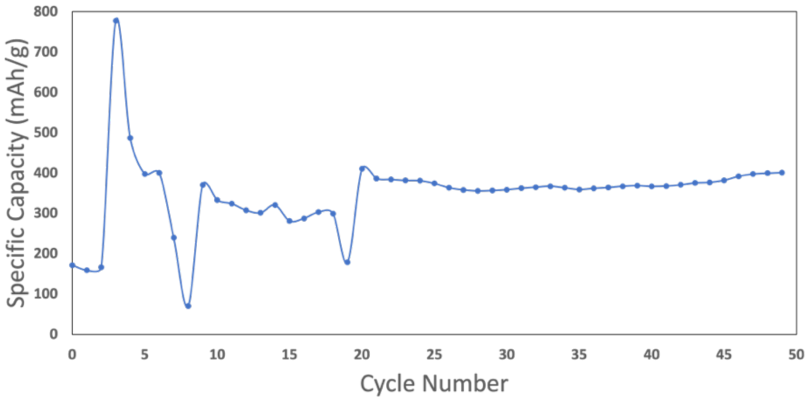

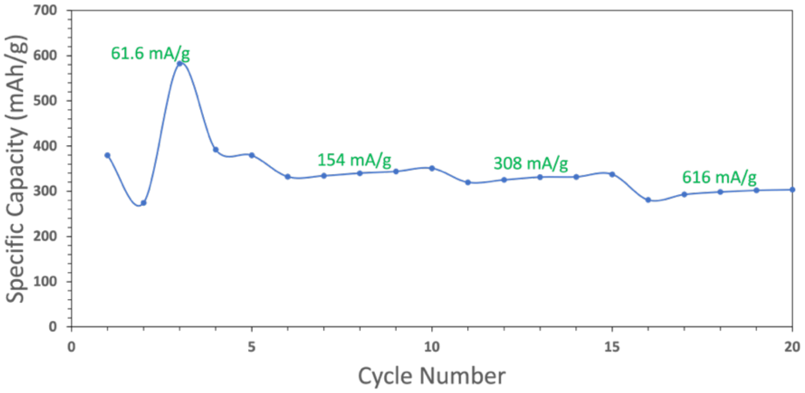

Figure 4.36 Representative battery performance of the **H1** region cathodes with the composition of $Bi_{0.04}Na_{0.37}Ni_{0.06}Mn_{0.53}O_x/Bi_{0.06}Na_{0.60}Ni_{0.09}Mn_{0.85}O_x$

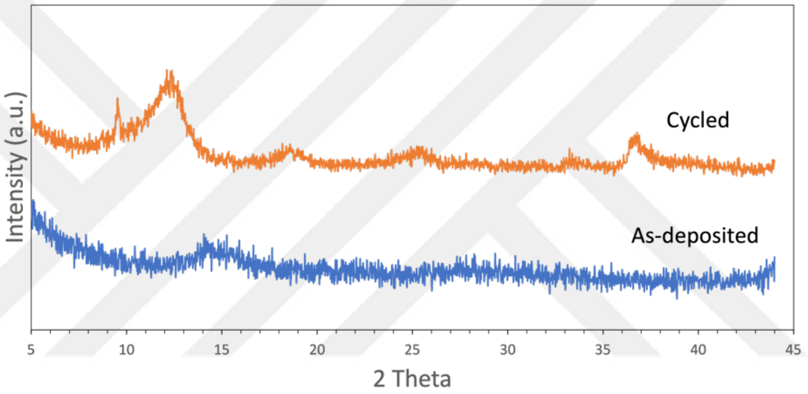

Figure 4.37 XRD pattern of the representative sample from the region **H1**, having composition of $Bi_{0.04}Na_{0.37}Ni_{0.06}Mn_{0.53}O_x/Bi_{0.06}Na_{0.60}Ni_{0.09}Mn_{0.85}O_x$

The region H2 display quite different features, Figure 4.38. Here the most striking feature is that the capacity increases with cycling. Initially high capacity drops to 270 mAh/g, but then rises steadily and after 30th cycle yields a capacity close to 700 mAh/g. Voltammogram of this cathode have also different features. Shoulders close to the main oxidation and reduction peaks on their left side are almost non-existent. XRD pattern of this sample before and after cycling is given in Figure 4.39. Here the cathode was nanocrystalline in the as-deposited state and upon cycling the peaks are broadened more implying that the structure was refined upon cycling. Rate capability of the H2 was impressive which is the discharge capacity is between 300 and 150 mAh/g as increasing the current from 61.6 mA/g to 616 mA/g.

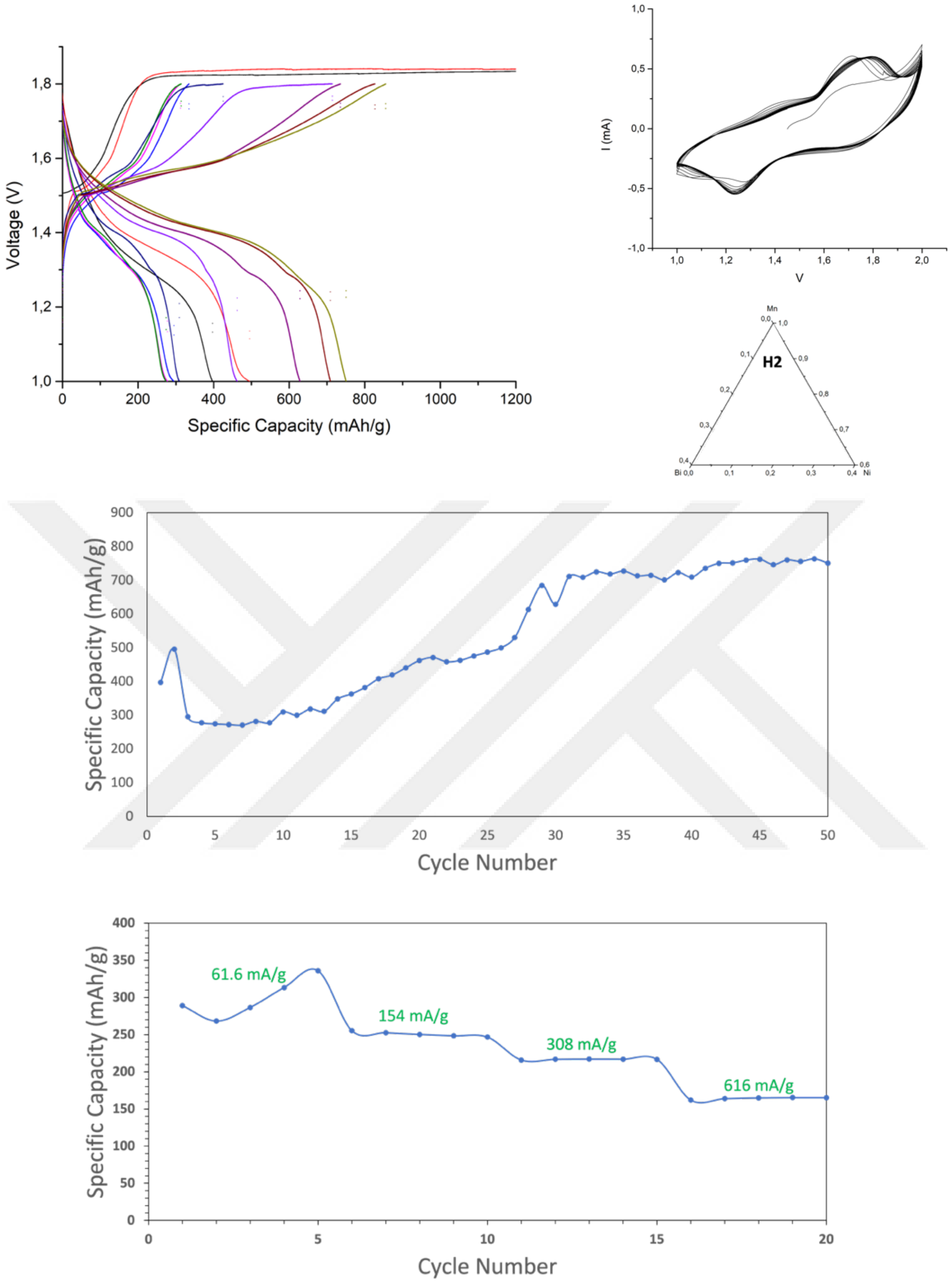

Figure 4.38 Representative battery performance of the **H2** region cathodes with composition of $Bi_{0.02}Na_{0.63}Ni_{0.02}Mn_{0.33}O_x/Bi_{0.05}Na_{1.71}Ni_{0.06}Mn_{0.89}O_x$

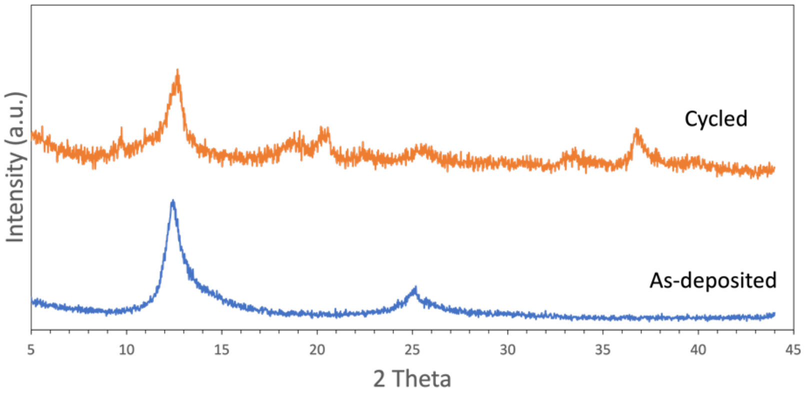

Figure 4.39 XRD pattern of the representative sample from the region **H2**, having composition of $Bi_{0.02}Na_{0.63}Ni_{0.02}Mn_{0.33}O_x/Bi_{0.05}Na_{1.71}Ni_{0.06}Mn_{0.89}O_x$

Having selected the candidate compositions, it would be useful to examine Bi content less than 10% contributes to the improvement of redox potential via decreasing the difference between the charge and discharge potential. Meanwhile, region L, M and H1 are on the 10% Ni line in the ternary diagram.

As a result, three different locations were selected namely, M, H1 and H2 having representative compositions of $Bi_{0.04}Na_{0.55}Ni_{0.04}Mn_{0.36}O_x$, $Bi_{0.04}Na_{0.37}Ni_{0.06}Mn_{0.53}O_x$, and $Bi_{0.02}Na_{0.63}Ni_{0.02}Mn_{0.33}O_x$, respectively. They are tabulated in Table 4.5. Na content in the ternary phase flied is shown platted in Figure 4.40 It is seen that the selected compositions M, H1 and H2 fall in Na rich region.

Table 4.5 Specific discharge capacities (mAh/g) of selected compositions

Composition	**Region**	**First**	**Last**	**Max.**	**Min.**	**Avg.**	**1st discharge OCV (V)**
$Bi_{0.04}Na_{0.55}Ni_{0.04}Mn_{0.36}O_x$	M	571	429	571	162	393	1.79
$Bi_{0.04}Na_{0.37}Ni_{0.06}Mn_{0.53}O_x$	H1	171	401	777	70	348	1.49
$Bi_{0.02}Na_{0.63}Ni_{0.02}Mn_{0.33}O_x$	H2	396	750	763	270	538	1.77

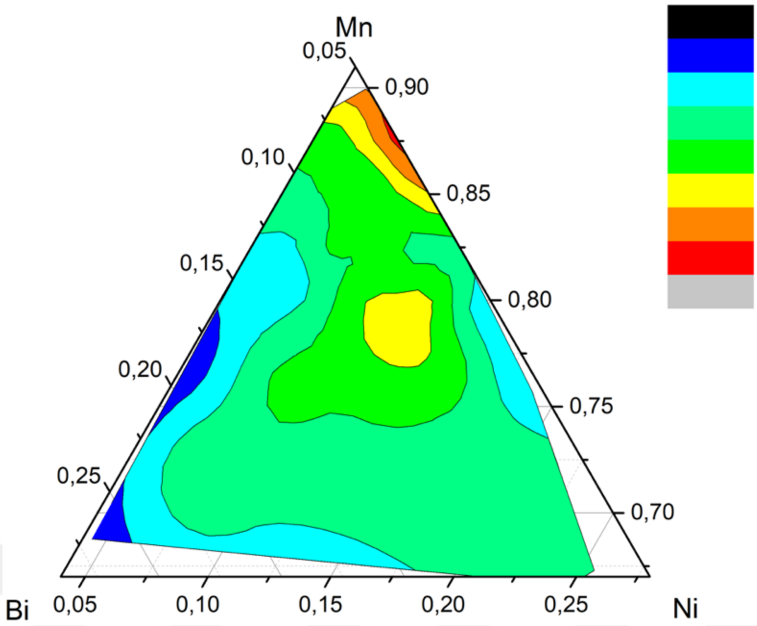

Figure 4.40 Na distribution on Bi-Mn-Ni ternary diagram

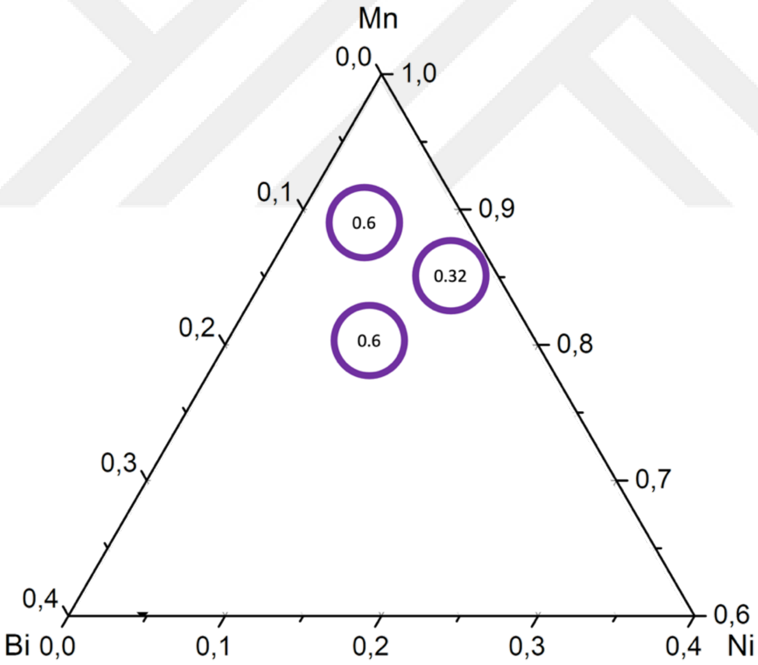

Figure 4.41 Selected regions from the Mn-rich cathodes. Note that their Na content written in the circles

Some of the capacities reported in this study is quite high, higher than that obtained with two electron exchanges of MnO_2 (616 mAh/g). These cathodes are quite rich both in Na and Mn. A preliminary study was made as to the source of these additional capacity. An experiment was therefore carried using nickel foil without any active material on it, anode was zinc foil. Two cells were made one with 2M $ZnSO_4$ and the other 2M $ZnSO_4$+0.1M $MnSO_4$ aqueous electrolyte. Cells were cycled with 20 μA between 1.0 V and 1.8 V. Voltammograms were recorded from 1.0 to 1.8 V with a sweep rate of 2 mV/sec.

Voltage profile and the CV profile of those two cells were plotted in Figure 4.42. The capacity was 0.0015 mAh for the cell with 2M $ZnSO_4$ electrolyte while with 2M ZnSO4+0.1M $MnSO_4$ the capacity was six times higher with 0.009 mAh. CV profiles confirm these results as with 2M $ZnSO_4$+0.1M $MnSO_4$ electrolyte has a well-defined oxidation and reduction peaks at around 1.7 V and 1.35 V respectively.

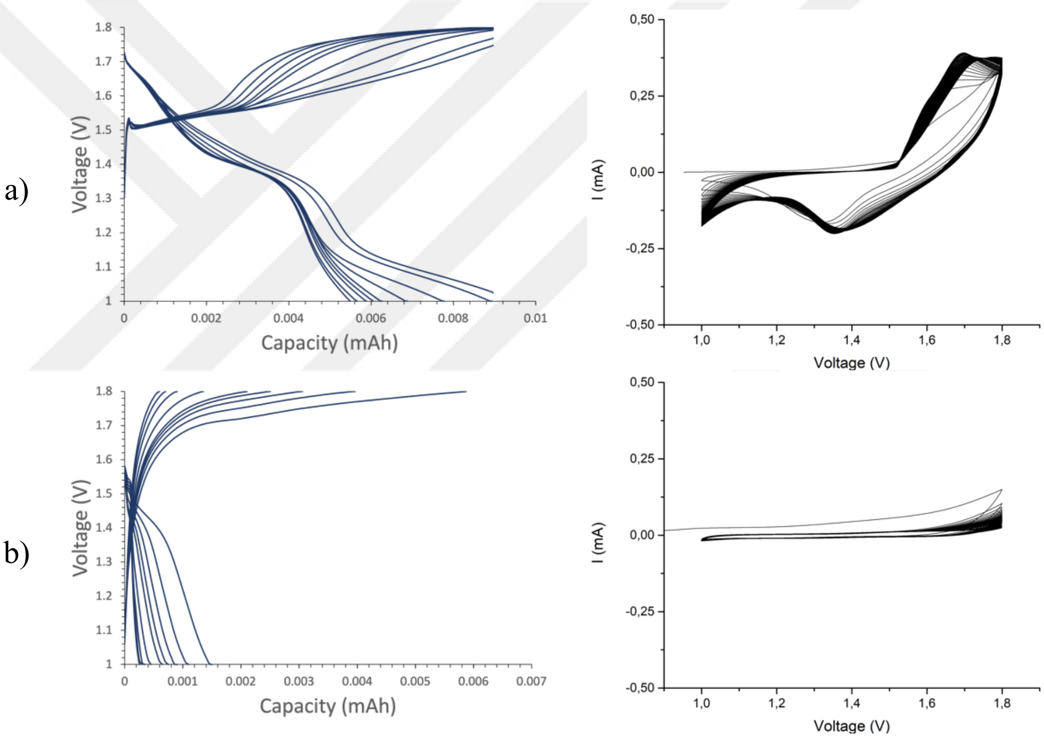

Figure 4.42 Voltage and CV profile of Ni-Zn cell in electrolyte of **a)** 2M $ZnSO_4$+0.1M $MnSO_4$ and **b)** 2M $ZnSO_4$

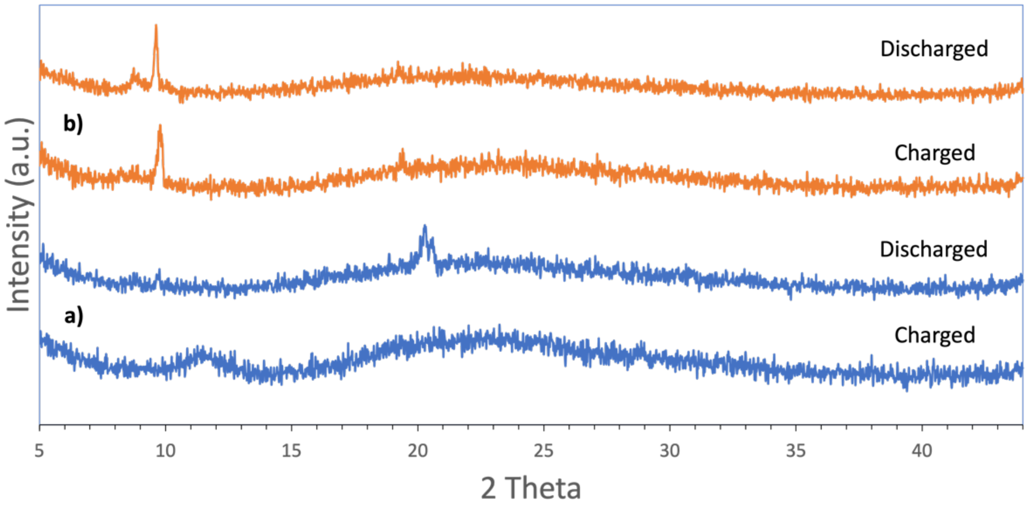

Figure 4.43 XRD pattern of Ni cathodes at charged/discharged state in electrolyte of **a)** 2M $ZnSO_4$+0.1M $MnSO_4$ and **b)** 2M $ZnSO_4$

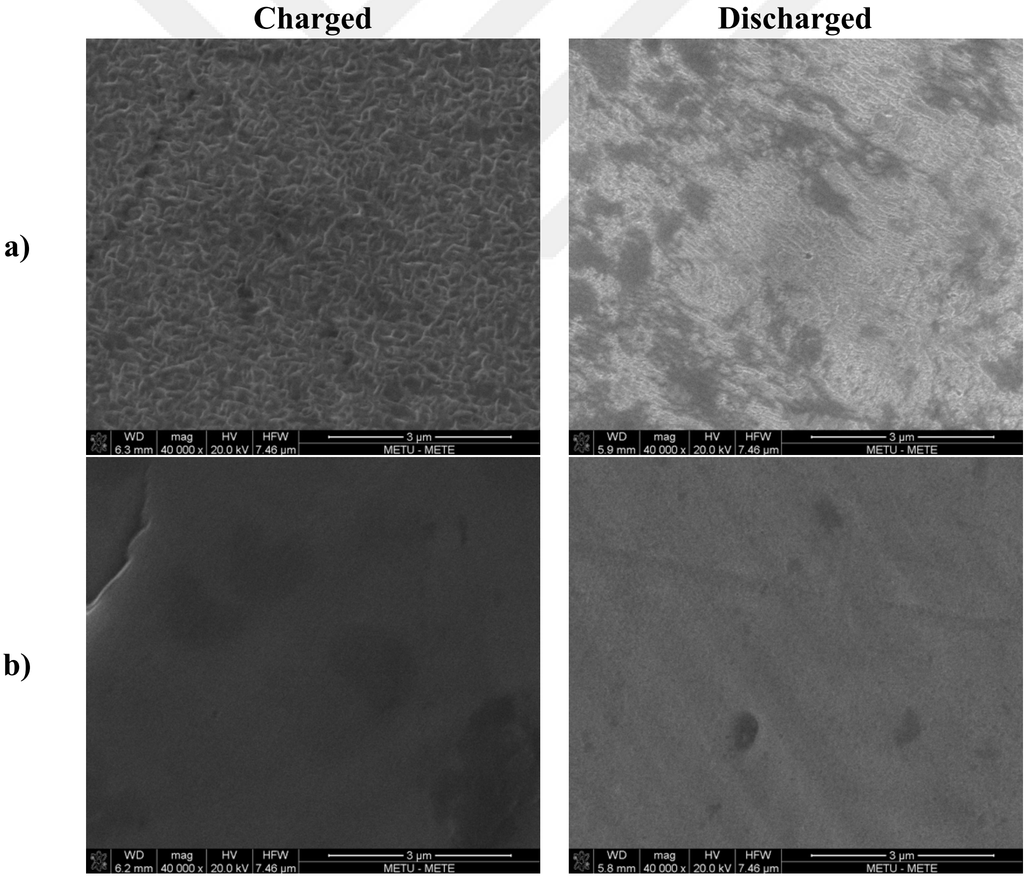

Figure 4.44 SEM image of Ni cathodes surface after 50 cycles in electrolyte of **a)** 2M $ZnSO_4$+0.1M $MnSO_4$ and **b)** 2M $ZnSO_4$

XRD pattern of these cathodes in charged and discharged states are given in Figure 4.43. The patterns appear to differ from each other in the case of 2M $ZnSO_4$+0.1M $MnSO_4$ electrolyte from charged and discharge state, whereas with 2M $ZnSO_4$ electrolyte there is not much difference. SEM micrographs were also similar, Figure 4.44. Without $MnSO_4$ the “cathode” surface is featureless whereas with 2M $ZnSO_4$+0.1M $MnSO_4$ there are quite distinct changes in the surface. In the charged state, there are platelet structure which is similar to those commonly observed in δ-MnO_2. All these point out to the possibility that the active compound may deposit onto cathode reversibly which might be responsible for a fraction of the observed capacity.

4.3.6 Conclusion

Thick film cathodes were successfully deposited in combinatorial geometry on (Bi, Na,Ni,Mn)O_x quaternary compositional space. A total of 108 thick film cathode were tested in terms of CV, charge, and discharge profiles as well as in terms of capacity versus cycle number. A Mn rich space was mapped in terms of discharge voltage, redox potential difference, initial, maximum, average, and final capacities. The study has shown three compositions where the capacity was 400 mAh/g or above. These were $Bi_{0.04}Na_{0.55}Ni_{0.04}Mn_{0.36}O_x$, $Bi_{0.04}Na_{0.37}Ni_{0.06}Mn_{0.53}O_x$, and $Bi_{0.02}Na_{0.63}Ni_{0.02}Mn_{0.33}O_x$.

CHAPTER 5

GENERAL CONCLUSION

This thesis focuses on finding a new MnO_2-based cathode composition(s) for Zn-ion batteries. For this purpose combinatorial approach was employed using thick film cathodes deposited via magnetron sputtering. The system under study was MnO_2 alloyed with $NaMnO_2$, Bi_2O_3, NiO. Accordingly, four sputter targets were prepared; MnO_2 target was in 3-inch diameter placed in the center and the other oxides were 2-inch in diameter placed 120° to one another forming a triangle. Substrates were 12.7 mm in diameter placed in a substrate magazine with a triangular geometry mimicking the targets underneath. A total of 36 cathode were deposited in a single sputtering experiment each with a different composition.

A total of six experiments were carried yielding 216 cathodes. Cathodes were deposited on Ni foil used as a current collector. They were typically 3 μm thick with a mass varying from 0.23 to 2.38 mg. Cells used was of Swagelok type, anode was 300 μm thick Zn foil electrolyte was 2M $ZnSO_4$ + 0.1 M $MnSO_4$ aqueous solution.

The preliminary results indicated favorable results in Mn rich cathodes. As a result, out of six sets three set of cathodes were selected for detailed study.

Cyclic voltammetry as well as galvanostatic tests were carried for each cathode. Mn rich corner of the Bi-Mn-Ni ternary diagram where Na varied from 11 to 78% were mapped in terms of capacities, cyclic stability, and discharge plateau potential. Based on maps, three candidate compositions were selected with discharge capacities above 400 mAh/g. These are $Bi_{0.04}Na_{0.55}Ni_{0.04}Mn_{0.36}O_x$, $Bi_{0.04}Na_{0.37}Ni_{0.06}Mn_{0.53}O_x$ and $Bi_{0.02}Na_{0.63}Ni_{0.02}Mn_{0.33}O_x$.

The findings reported above, and the compositions reported refer to a rather special case of cathodes which were in the form coating no more than 3 μm thick which is fully adhered to the nickel current collector. Although with cycling the coatings may break-off in some cases, this geometry is rather special making full use of the cathode material. This is unlike the case in cathodes prepared with slurry method where it is well known than MnO_2 has severe conductivity problems. Therefore, further work is needed to check the full potential of the selected cathodes with slurry method and establish what fraction of capacity obtained in this work is reproducible with slurry method. An optimization study would therefore be needed, with regard to the preparation of slurry in terms of the choice of conductivity agent and the binder. Another aspect is that the current cathodes being in the form of films has large specific surface area, this advantage will no longer be applicable with slurry method. Mass load of the cathodes can be optimized, and cathode performance can be compared in terms of areal current density.

REFERENCES

[1] H. Y. Kang and C. C. Liang, “The Anodic Oxidation of Manganese Oxides in Alkaline Electrolytes,” *J. Electrochem. Soc.*, vol. 115, no. 1, p. 6, 1968.

[2] K. Kordesch, J. Gsellmann, M. Peri, K. Tomantschger, and R. Chemelli, “The rechargeability of manganese dioxide in alkaline electrolyte,” *Electrochim. Acta*, vol. 26, no. 10, pp. 1495–1504, 1981.

[3] Q. N. Zhu *et al.*, “Challenges and strategies for ultrafast aqueous zinc-ion batteries,” *Rare Met.*, vol. 40, no. 2, pp. 309–328, Feb. 2021.

[4] G. G. Yadav *et al.*, “Regenerable Cu-intercalated MnO 2 layered cathode for highly cyclable energy dense batteries,” *Nat. Commun.*, vol. 8, no. May 2016, pp. 1–9, 2017.

[5] B. J. Hertzberg *et al.*, “Effect of Multiple Cation Electrolyte Mixtures on Rechargeable Zn-MnO2 Alkaline Battery,” *Chem. Mater.*, vol. 28, no. 13, pp. 4536–4545, 2016.

[6] T. Shoji, M. Hishinuma, and T. Yamamoto, “Zinc-manganese dioxide galvanic cell using zinc sulphate as electrolyte. Rechargeability of the cell,” *J. Appl. Electrochem.*, vol. 18, no. 4, pp. 521–526, 1988.

[7] C. Xu, B. Li, H. Du, and F. Kang, “Energetic zinc ion chemistry: The rechargeable zinc ion battery,” *Angew. Chemie - Int. Ed.*, vol. 51, no. 4, pp. 933–935, 2012.

[8] W. Sun *et al.*, “Zn/MnO2 Battery Chemistry with H+ and Zn2+ Coinsertion,” *J. Am. Chem. Soc.*, vol. 139, no. 29, pp. 9775–9778, 2017.

[9] F. R. McLarnon and E. J. Cairns, “The Secondary Alkaline Zinc Electrode,” *J. Electrochem. Soc.*, vol. 138, no. 2, pp. 645–656, 1991.

[10] J. Shin, J. Lee, Y. Park, and J. W. Choi, “Aqueous zinc ion batteries: Focus on zinc metal anodes,” *Chem. Sci.*, vol. 11, no. 8, pp. 2028–2044, 2020.

[11] C. C. Yang and S. J. Lin, “Improvement of high-rate capability of alkaline Zn-MnO2 battery,” *J. Power Sources*, vol. 112, no. 1, pp. 174–183, 2002.

[12] N. Zhang *et al.*, “Cation-Deficient Spinel ZnMn2O4 Cathode in Zn(CF3SO3)2 Electrolyte for Rechargeable Aqueous Zn-Ion Battery,” *J. Am. Chem. Soc.*, vol. 138, no. 39, pp. 12894–12901, 2016.

[13] C. Li *et al.*, “Spatially homogeneous copper foam as surface dendrite-free host for zinc metal anode,” *Chem. Eng. J.*, vol. 379, p. 122248, Jan. 2020.

[14] H. Li *et al.*, “Enhancement on Cycle Performance of Zn Anodes by Activated Carbon Modification for Neutral Rechargeable Zinc Ion Batteries,” *J. Electrochem. Soc.*, vol. 162, no. 8, pp. A1439–A1444, 2015.

[15] X. Xie *et al.*, “Manipulating the ion-transfer kinetics and interface stability for high-performance zinc metal anodes,” *Energy Environ. Sci.*, vol. 13, no. 2, pp. 503–510, 2020.

[16] L. Kang *et al.*, “Nanoporous CaCO3 Coatings Enabled Uniform Zn Stripping/Plating for Long-Life Zinc Rechargeable Aqueous Batteries,” *Adv. Energy Mater.*, vol. 8, no. 25, p. 1801090, Sep. 2018.

[17] K. Zhao *et al.*, “Ultrathin Surface Coating Enables Stabilized Zinc Metal Anode,” *Adv. Mater. Interfaces*, vol. 5, no. 16, p. 1800848, Aug. 2018.

[18] M. Cui *et al.*, “Quasi-Isolated Au Particles as Heterogeneous Seeds to Guide Uniform Zn Deposition for Aqueous Zinc-Ion Batteries,” *ACS Appl. Energy Mater.*, vol. 2, no. 9, pp. 6490–6496, 2019.

[19] Z. Zhao *et al.*, “Long-life and deeply rechargeable aqueous Zn anodes enabled by a multifunctional brightener-inspired interphase,” *Energy Environ. Sci.*, vol. 12, no. 6, pp. 1938–1949, 2019.

[20] H. Pan *et al.*, “Reversible aqueous zinc/manganese oxide energy storage from conversion reactions,” *Nat. Energy*, vol. 1, pp. 1–9, 2016.

[21] N. Zhang *et al.*, “Rechargeable aqueous zinc-manganese dioxide batteries with high energy and power densities,” *Nat. Commun.*, vol. 8, no. 1, pp. 1–9, 2017.

[22] T. Yuan *et al.*, “Novel Alkaline Zn/Na0.44MnO2 Dual-Ion Battery with a High Capacity and Long Cycle Lifespan,” *ACS Appl. Mater. Interfaces*, vol. 10, no. 40, pp. 34108–34115, 2018.

[23] M. Chamoun, W. R. Brant, C. W. Tai, G. Karlsson, and D. Noréus, “Rechargeability of aqueous sulfate Zn/MnO2 batteries enhanced by accessible Mn2+ ions,” *Energy Storage Mater.*, vol. 15, no. December 2017, pp. 351–360, 2018.

[24] S. Zhang *et al.*, “An adaptive and stable bio-electrolyte for rechargeable Zn-ion batteries,” *J. Mater. Chem. A*, vol. 6, no. 26, pp. 12237–12243, 2018.

[25] Y. Huang *et al.*, “Novel Insights into Energy Storage Mechanism of Aqueous Rechargeable Zn/MnO2 Batteries with Participation of Mn2+,” *Nano-Micro Lett.*, vol. 11, no. 1, 2019.

[26] W. Fan *et al.*, “A high voltage aqueous zinc-manganese battery using a hybrid alkaline-mild electrolyte,” *Chem. Commun.*, vol. 56, no. 13, pp. 2039–2042, 2020.

[27] C. Zhong *et al.*, “Decoupling electrolytes towards stable and high-energy rechargeable aqueous zinc–manganese dioxide batteries,” *Nat. Energy*, vol. 5, no. 6, pp. 440–449, 2020.

[28] S. D. Han *et al.*, “Mechanism of Zn Insertion into Nanostructured δ-MnO2: A Nonaqueous Rechargeable Zn Metal Battery,” *Chem. Mater.*, vol. 29, no. 11, pp. 4874–4884, 2017.

[29] W. Wei, X. Cui, W. Chen, and D. G. Ivey, “Manganese oxide-based materials as electrochemical supercapacitor electrodes,” *Chem. Soc. Rev.*, vol. 40, no. 3, pp. 1697–1721, Feb. 2011.

[30] D. A. Kitchaev, S. T. Dacek, W. Sun, and G. Ceder, “Thermodynamics of Phase Selection in MnO2 Framework Structures through Alkali Intercalation and Hydration,” *J. Am. Chem. Soc.*, vol. 139, no. 7, pp. 2672–2681, 2017.

[31] J. E. Post, “Manganese oxide minerals: Crystal structures and economic and environmental significance,” *Proc. Natl. Acad. Sci. U. S. A.*, vol. 96, no. 7, pp. 3447–3454, Mar. 1999.

[32] C. C. Ji, M. W. Xu, S. J. Bao, C. J. Cai, R. Y. Wang, and D. Z. Jia, “Effect of alkaline and alkaline-earth cations on the supercapacitor performance of MnO2 with various crystallographic structures,” *J. Solid State Electrochem.*, vol. 17, no. 5, pp. 1357–1368, May 2013.

[33] J. Hao *et al.*, “Electrochemically induced spinel-layered phase transition of Mn3O4 in high performance neutral aqueous rechargeable zinc battery,” *Electrochim. Acta*, vol. 259, pp. 170–178, 2018.

[34] B. Jiang, C. Xu, C. Wu, L. Dong, J. Li, and F. Kang, “Manganese Sesquioxide as Cathode Material for Multivalent Zinc Ion Battery with High Capacity and Long Cycle Life,” *Electrochim. Acta*, vol. 229, pp. 422–428, 2017.

[35] S. Chen, X. Feng, M. Yao, Y. Wang, F. Wang, and Y. Zhang, “Rice-shaped porous ZnMn2O4 microparticles as advanced anode materials for lithium-ion batteries,” *Dalt. Trans.*, vol. 47, no. 32, pp. 11166–11175, Aug. 2018.

[36] J. E. Post, “Crystal structures of manganese oxide minerals,” *Catena Suppl.*, vol. 21, pp. 51–73, 1992.

[37] Y. Chabre and J. Pannetier, “Structural and electrochemical properties of the proton / γ-MnO2 system,” *Prog. Solid State Chem.*, vol. 23, no. 1, pp. 1–130, Jan. 1995.

[38] S. Fritsch, J. E. Post, and A. Navrotsky, “Energetics of low-temperature polymorphs of manganese dioxide and oxyhydroxide,” *Geochim.*

Cosmochim. Acta, vol. 61, no. 13, pp. 2613–2616, Jul. 1997.

[39] A. M. Byström, E. W. Lund, L. K. Lund, and M. Hakala, “The Crystal Structure of Ramsdellite, an Orthorhombic Modification of MnO2.,” *Acta Chem. Scand.*, vol. 3, pp. 163–173, 1949.

[40] M. H. Alfaruqi *et al.*, “Electrochemically induced structural transformation in a γ-MnO2 cathode of a high capacity zinc-ion battery system,” *Chem. Mater.*, vol. 27, no. 10, pp. 3609–3620, 2015.

[41] H. Li *et al.*, “An extremely safe and wearable solid-state zinc ion battery based on a hierarchical structured polymer electrolyte,” *Energy Environ. Sci.*, vol. 11, no. 4, pp. 941–951, 2018.

[42] X. Gao *et al.*, “H+-Insertion Boosted α-MnO2 for an Aqueous Zn-Ion Battery,” *Small*, vol. 16, no. 5, pp. 1–10, 2020.

[43] L. Li, T. K. A. Hoang, J. Zhi, M. Han, S. Li, and P. Chen, “Functioning Mechanism of the Secondary Aqueous Zn-β-MnO2 Battery,” *ACS Appl. Mater. Interfaces*, vol. 12, no. 11, pp. 12834–12846, 2020.

[44] M. Han *et al.*, “Oxygen Defects in β-MnO2 Enabling High-Performance Rechargeable Aqueous Zinc/Manganese Dioxide Battery,” *iScience*, vol. 23, no. 1, 2020.

[45] S. Islam *et al.*, “Facile synthesis and the exploration of the zinc storage mechanism of β-MnO2 nanorods with exposed (101) planes as a novel cathode material for high performance eco-friendly zinc-ion batteries,” *J. Mater. Chem. A*, vol. 5, no. 44, pp. 23299–23309, Nov. 2017.

[46] M. H. Alfaruqi *et al.*, “A layered δ-MnO2 nanoflake cathode with high zinc-storage capacities for eco-friendly battery applications,” *Electrochem. commun.*, vol. 60, pp. 121–125, 2015.

[47] C. Guo *et al.*, “Ultrathin δ-MnO 2 nanosheets as cathode for aqueous rechargeable zinc ion battery,” *Electrochim. Acta*, vol. 304, pp. 370–377,

2019.

[48] C. Guo *et al.*, “A case study of β- and δ-MnO2 with different crystallographic forms on ion-storage in rechargeable aqueous zinc ion battery,” *Electrochim. Acta*, vol. 324, pp. 1–9, 2019.

[49] D. Wang *et al.*, “A Superior δ-MnO2 Cathode and a Self-Healing Zn-δ-MnO2 Battery,” *ACS Nano*, vol. 13, no. 9, pp. 10643–10652, 2019.

[50] X. Guo *et al.*, “A hollow-structured manganese oxide cathode for stable zn-mno2 batteries,” *Nanomaterials*, vol. 8, no. 5, 2018.

[51] Y. Wu *et al.*, “Amorphous Manganese Oxides: An Approach for Reversible Aqueous Zinc-Ion Batteries,” *ACS Appl. Energy Mater.*, vol. 3, no. 2, pp. 1627–1633, Feb. 2020.

[52] V. Soundharrajan *et al.*, “The dominant role of Mn2+ additive on the electrochemical reaction in ZnMn2O4 cathode for aqueous zinc-ion batteries,” *Energy Storage Mater.*, vol. 28, pp. 407–417, 2020.

[53] I. Stoševski, A. Bonakdarpour, B. Fang, S. T. Voon, and D. P. Wilkinson, “Hausmannite Mn3O4 as a positive active electrode material for rechargeable aqueous Mn-oxide/Zn batteries,” *Int. J. Energy Res.*, vol. 45, no. 1, pp. 220–230, 2021.

[54] T. Yuan *et al.*, “Novel Alkaline Zn/Na0.44MnO2 Dual-Ion Battery with a High Capacity and Long Cycle Lifespan,” *ACS Appl. Mater. Interfaces*, vol. 10, no. 40, pp. 34108–34115, 2018.

[55] T. Sun *et al.*, “Micron-sized Na0.7MnO2.05 as cathode materials for aqueous rechargeable magnesium-ion batteries,” *Ionics (Kiel).*, vol. 25, no. 10, pp. 4805–4815, 2019.

[56] J. Manzi *et al.*, “Monoclinic and orthorhombic namno2 for secondary batteries: A comparative study,” *Energies*, vol. 14, no. 5, p. 1230, Feb. 2021.

[57] F. Sauvage, L. Laffont, J. M. Tarascon, and E. Baudrin, “Study of the insertion/deinsertion mechanism of sodium into Na 0.44MnO2,” *Inorg. Chem.*, vol. 46, no. 8, pp. 3289–3294, Apr. 2007.

[58] J. P. Parant, R. Olazcuaga, M. Devalette, C. Fouassier, and P. Hagenmuller, “Sur quelques nouvelles phases de formule NaxMnO2 (x ≤ 1),” *J. Solid State Chem.*, vol. 3, no. 1, pp. 1–11, Feb. 1971.

[59] C. Delmas, C. Fouassier, and P. Hagenmuller, “Structural classification and properties of the layered oxides,” *Phys. B+C*, vol. 99, no. 1–4, pp. 81–85, Jan. 1980.

[60] X. Wu *et al.*, “The electrochemical performance of aqueous rechargeable battery of Zn/Na0.44MnO2 based on hybrid electrolyte,” *Journal of Power Sources*, 2016. [Online]. Available: https://reader.elsevier.com/reader/sd/pii/S0378775316314446?token=0941D80F68185CFC6450BAF60A946EA9A3A70C9D8956908FA7619CD4BCA5B2E0B763294F7B1A0CC3F4EA1C51A9D08AFC&originRegion=eu-west-1&originCreation=20220114005527. [Accessed: 14-Jan-2022].

[61] F. Yin *et al.*, “Na4Mn9O18/Carbon Nanotube Composite as a High Electrochemical Performance Material for Aqueous Sodium-Ion Batteries,” *Nanoscale Res. Lett.*, vol. 12, 2017.

[62] X. Wang, X. Qin, Q. Lu, M. Han, A. Omar, and D. Mikhailova, “Mixed phase sodium manganese oxide as cathode for enhanced aqueous zinc-ion storage,” *Chinese Journal of Chemical Engineering*, 2020. [Online]. Available: https://reader.elsevier.com/reader/sd/pii/S1004954120302275?token=DA49836E2EE75D5CECFE5CD0DCC85435E9BF2C5812331FA33C818CE2E8E6C91253E44AECCEC2D996857FC9EEB7EFB8E1&originRegion=eu-west-1&originCreation=20220114012642. [Accessed: 14-Jan-2022].

[63] L. T. Yu, “Rechargeability of MnO2 in KOH Media Produced by

Decomposition of Dissolved KMnO4 and Bi (NO 3) 3 Mixtures: II. A Reaction Viewpoint on the Role of Bi," *J. Electrochem. Soc.*, vol. 144, no. 3, pp. 802–809, 1997.

[64] M. Minakshi and P. Singh, "Synergistic effect of additives on electrochemical properties of MnO 2 cathode in aqueous rechargeable batteries," *J. Solid State Electrochem.*, vol. 16, no. 4, pp. 1487–1492, 2012.

[65] A. Biswal, M. Minakshi, and B. C. Tripathy, "Electrodeposition of Sea Urchin and Cauliflower-like Nickel-/Cobalt-Doped Manganese Dioxide Hierarchical Nanostructures with Improved Energy-Storage Behavior," *ChemElectroChem*, vol. 3, no. 6, pp. 976–985, 2016.

[66] G. Sokolsky, L. Zudina, E. Boldyrev, O. Miroshnikov, N. Gauk, and O. Y. Kiporenko, "ORR electrocatalysis on Cr3+, Fe2+, Co2+-doped manganese(IV) oxides," *Acta Phys. Pol. A*, vol. 133, no. 4, pp. 1097–1102, 2018.

[67] D. Sari, F. Piskin, Z. C. Torunoglu, B. Yasar, Y. E. Kalay, and T. Ozturk, "Combinatorial development of nanocrystalline/amorphous (La,Sr)CoO3-(La,Sr)2CoO4 composite cathodes for IT-SOFCs," *Solid State Ionics*, vol. 326, pp. 124–130, Nov. 2018.

[68] L. Lutterotti, S. Matthies, and H.-R. Wenk, "MAUD: a friendly Java program for material analysis using diffraction," *IUCr Newsl. CPD*, vol. 21, pp. 14–15, 1999.

[69] Y. N. Zhou, M. Z. Xue, and Z. W. Fu, "Nanostructured thin film electrodes for lithium storage and all-solid-state thin-film lithium batteries," *J. Power Sources*, vol. 234, pp. 310–332, Jul. 2013.

[70] S. Lobe, A. Bauer, S. Uhlenbruck, and D. Fattakhova-Rohlfing, "Physical Vapor Deposition in Solid-State Battery Development: From Materials to Devices," *Adv. Sci.*, vol. 8, no. 11, p. 2002044, Jun. 2021.

[71] P. J. Bouwman, B. A. Boukamp, H. J. M. Bouwmeester, H. J. Wondergem, and P. H. L. Notten, “Structural Analysis of Submicrometer LiCoO2 Films,” *J. Electrochem. Soc.*, vol. 148, no. 4, p. A311, 2001.

[72] M. D. Fleischauer, T. D. Hatchard, A. Bonakdarpour, and J. R. Dahn, “Combinatorial investigations of advanced Li-ion rechargeable battery electrode materials,” *Meas. Sci. Technol.*, vol. 16, no. 1, pp. 212–220, 2005.

[73] J. F. Whitacre, W. C. West, and B. V. Ratnakumar, “A Combinatorial Study of Li[sub y]Mn[sub x]Ni[sub 2−x]O[sub 4] Cathode Materials Using Microfabricated Solid-State Electrochemical Cells,” *J. Electrochem. Soc.*, vol. 150, no. 12, p. A1676, 2003.

[74] J. J. Hanak, “The ‘multiple-sample concept’ in materials research: Synthesis, compositional analysis and testing of entire multicomponent systems,” *J. Mater. Sci.*, vol. 5, no. 11, pp. 964–971, 1970.

[75] T. D. Hatchard, J. M. Topple, M. D. Fleischauer, and J. R. Dahn, “Electrochemical performance of SiAlSn films prepared by combinatorial sputtering,” *Electrochem. Solid-State Lett.*, vol. 6, no. 7, 2003.

[76] M. A. Borysiewicz, M. Wzorek, M. Myśliwiec, J. Kaczmarski, and M. Ekielski, “MnO2 ultrathin films deposited by means of magnetron sputtering: Relationships between process conditions, structural properties and performance in transparent supercapacitors,” *Superlattices Microstruct.*, vol. 100, pp. 1213–1220, 2016.

[77] C. C. Lin and P. Y. Lin, “Capacitance measurements of MnOx films deposited by reactive sputtering of a Mn target,” *Electrochemistry*, vol. 79, no. 6, pp. 458–463, 2011.

[78] F. Pişkin, H. Akyildiz, and T. Öztürk, “Ti modified Pd-Ag membranes for hydrogen separation,” *Int. J. Hydrogen Energy*, vol. 40, no. 24, pp. 7553–7558, Jun. 2015.

[79] F. Pişkin and T. Öztürk, “Combinatorial screening of Pd-Ag-Ni membranes for hydrogen separation,” *J. Memb. Sci.*, vol. 524, pp. 631–636, Feb. 2017.

[80] F. Pişkin and T. Öztürk, “Nb-Pd-Ti BCC thin films for hydrogen separation,” *J. Alloys Compd.*, vol. 775, pp. 411–418, Feb. 2019.

[81] J. Zhang, Y. Li, L. Wang, C. Zhang, and H. He, “Catalytic oxidation of formaldehyde over manganese oxides with different crystal structures,” *Catal. Sci. Technol.*, vol. 5, no. 4, pp. 2305–2313, Mar. 2015.

APPENDICES

A. Fabrication And Testing of Slurry Based Zn-MnO_2 Battery

A.1 Introduction

A study conducted on (Bi,Na,Ni)MnO_2 system using thick film approach has yielded two compositions with high discharge capacity; $Bi_{0.04}Na_{0.37}Ni_{0.06}Mn_{0.53}O_x$, and $Bi_{0.02}Na_{0.63}Ni_{0.02}Mn_{0.33}O_x$. Following the selection of these candidate compositions, attempts were made to manufacture conventional battery using the slurry method. The cell is that of Swagelok, but instead of using thick film cathode deposited on Ni foil, here, the cathode was prepared using conventional slurry method on nickel foam.

A.2 Experimental Procedure

Structural characterization was carried using Rigaku DMAX2200 or Bruker D8 Advance X-ray diffractometer using with Cu-Kα radiation (λ=1.5406Å) at 30 kV at 40 mA current. The scanning rate was 1o/min with step size of 0.02°. Material characterization also included scanning electron microscopy. For this purpose, FEI Nova NanoSEM was used. Where necessary the samples were investigated with EDS analysis.

Active material for cathode was prepared by two methods; mixing and milling the oxide ingredients of the selected proportions or via calcination of the mixture prepared from ingredients of selected proportions at elevated temperature. Having prepared the active materials, the cathode slurry was prepared by mixing the active ingredients with carbon black and binder of selected proportions in DI water-ethanol (60:40) solution using. First, the binder (Teflon or CMC) was dissolved in the solution for 15 min and then carbon black was added and mixed for 30 min. Finally, active material was added and mixed for 60 minutes. All mixings were carried out using magnetic stirrer. Ni foam was used as the current collector. The slurry was coated onto Ni foams by dipping it into the solution. Then nickel foam was dried overnight in an oven at 60°C. Before and after coating, the foam was weighed (Sartorius CPA225D -0.01 mg sensitivity) from which the quantity of the cathode was determined. Ni foam loaded with cathode material was then pressed under 20 MPa to increase the compaction of the whole assembly.

Cells used for electrochemical characterization was of Swagelok type. Conventionally prepared MnO_2 based cathodes were loaded on Ni foams of 12.7 mm in diameter. Anode was Zn foil 300 μm thick (99.8% pure). Separator was Freudenberg FS 2226. Electrolyte was 2M $ZnSO_4$+0.1M $MnSO_4$ in DI water. Current collectors in the Swagelok cell were 12.9 mm diameter stainless steel rods. The Cell had a spring between the anode and the stainless-steel current collector which presses the cell assembly against the current collector on the cathode side. Spring was made of 1 mm stainless steel wire wound to a diameter of 12.4 mm with the length of 10.5 mm.

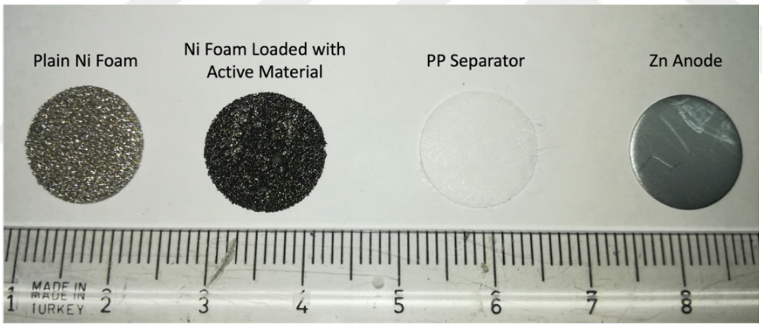

Figure A. 1 The components of the battery

Components of the cell are shown in Figure A. 1. Cells were assembled first by inserting the current collector and fixing the position of it using the conical insert. Then the cathode was placed against the current collector. This was followed by placing the separator on the cathode. Then 0.5 ml electrolyte were applied by drops which was absorbed by separator. Finally, Zn anode were placed over the separator. Then the cell was closed by placing a short stainless-steel rod followed by the spring and the current collector which was lightly pressed and fixed in position by a conical insert.

Electrochemical measurements were made with BioLogic MPG2 multichannel battery testing system.

A.3 Results and discussion

A.3.1 Separator (Polypropylene)

First, we investigated the separator. For this purpose, active material used was β-MnO_2 in powder form (Alfa Aesar, 98% pure). It was ball milled (Retsch PM 400 Ma-Type) at 400 rpm for 10 hours. XRD pattern of the milled powder is given in Figure A. 2. After ball milling, the powder had a mixture of phases, namely β-MnO_2 and Mn_2O_3. Active material, binder (Teflon) and conductive agent (carbon black) in mass proportions of 75:5:20 were mixed in DI water-ethanol as explained above.

Three cells were prepared where the number of separators used was changed. The capacity versus cycle number determined for the cell prepared with single separator is shown in blue in Figure A. 2 (a). The maximum capacity is around 80 mAh/g, but more importantly, the capacity drops to zero unexpectedly at 18th cycle. Upon examining the cell, it was observed that there was a short circuit between the anode and cathode as a result of dendritic growth of zinc which perforated the separator. So as to prevent the short circuit, multiple separators were used. The performance of the cell with 3 separator was included in Figure A. 3 (yellow). The cycle life was slightly longer and reached 24 cycles before it has failed.

Figure A. 3 also comprise data with cell incorporating 5 separators. The cell continued to function well even after 100 cycles. Fig 5.4 shows photograph of both the electrodes and the separators in sequence. It is seen that the first separator in contact with zinc was blackened quite markedly probably containing fragments of zinc dendrites. The second, third and fourth separators are affected less and less. Based on these observations it was concluded for cycle numbers of near 100 or so, a total of 5 separators yielding a total thickness of 900 micron would be necessary so as to prevent shorting of the electrodes.

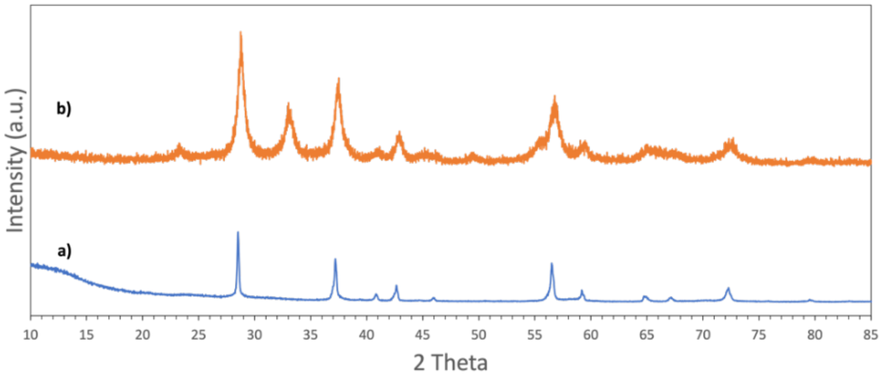

Figure A. 2 XRD pattern of **a)** β-MnO_2 and **b)** ball milled MnO_2

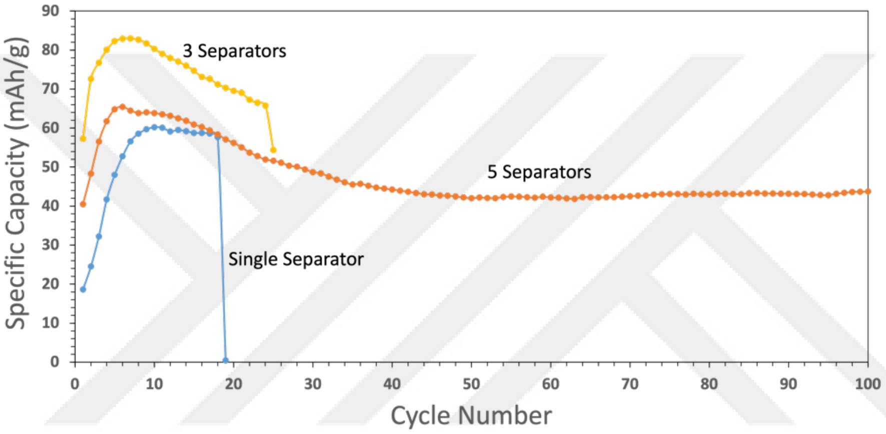

Figure A. 3 Cycling performance of ball milled MnO_2 with 20% carbon black. Note that increasing the number of the separator, increases the cycle life

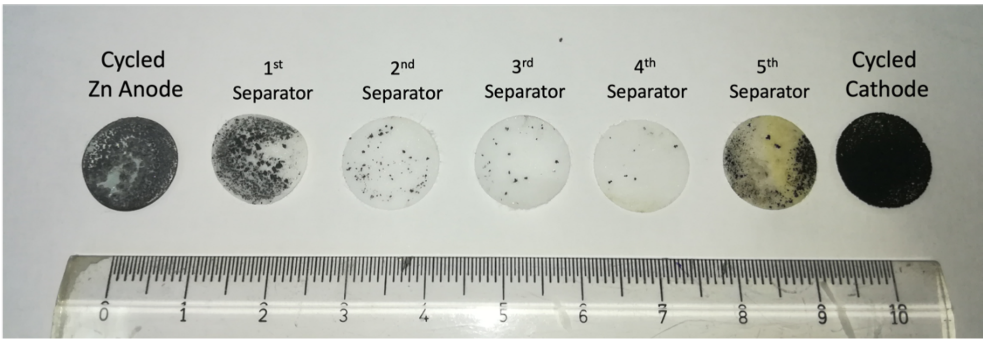

Figure A. 4 Disassembled battery with five separators

A.3.2 Conductive Agent (Carbon Black)

Four experiments were conducted to see the effect of conductive agent (carbon black) addition. For this purpose, slurries were prepared mixing active material (ball milled MnO_2 or as-synthesized $Na_{0.7}MnO_2$, binder (Teflon) and carbon black in mass proportions of 85:5:10 and 75:5:20. For ball milled MnO_2, the capacity versus cycle number for both carbon black additions are shown in Figure A. 5. It is seen that 10% carbon black addition for which two experiments were carried out yielded better performance. The initial capacity with 10% CB was higher in excess of 60 mAh/g. The capacity after 100 cycle was around 50 mAh/g which was slightly better than that with 20% CB.

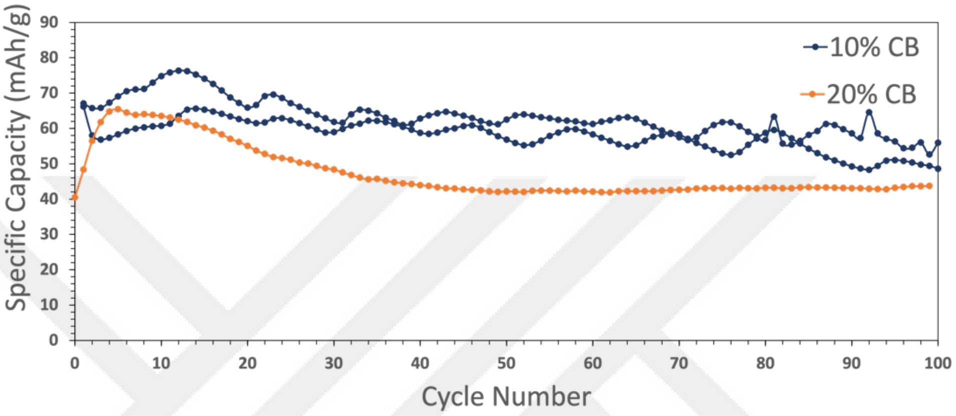

Figure A. 5 Cycling performance of ball milled MnO_2 with 10% and 20% carbon black

For as-synthesized $Na_{0.7}MnO_2$, the capacity versus cycle number was plotted in Figure A. 6. As seen in the figure, the initial capacity with 10% CB was low but increased with cycling reaching a capacity of around 60 mAh/g. The capacity after 100 cycles were similar in both samples.

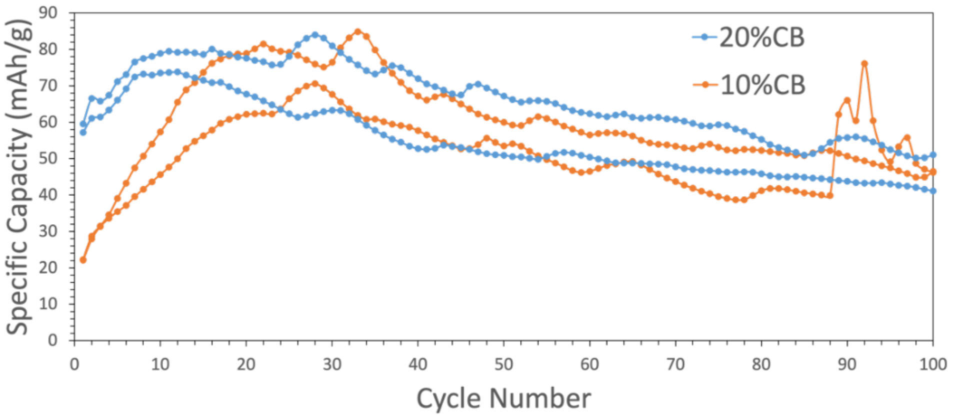

Figure A. 6 Cycling performance of as-synthesized $Na_{0.7}MnO_2$ with 10% and 20% carbon black

In conclusion, there was no significant difference between 10% and 20% carbon black additions and both additions may be preferred, though 10% CB has its advantage as it would maximize the active ingredient of the cathode.

A.3.3 Particle Size Reduction (Ball Milling)

Experiment reported above with $Na_{0.7}MnO_2$ was carried out by hand grinding of as-synthesized powder in mortar. So as to see the effect of ball milling, a separate experiment was also carried out where the as-synthesized powder was milled at 180 rpm for 6 hours.

For electrochemical measurements, slurry was prepared mixing the ball milled powder, Teflon (binder) and carbon black (conductive agent) in mass proportions of 75:5:20. Capacities versus cycle number are plotted in Figure A. 7. It is seen that the electrode with ball milled powder is already active yielding significantly higher capacity at around 140 mAh/g. However, the capacity decays quite rapidly with cycling and after 10 cycles or so there is very little difference between ground and milled samples.

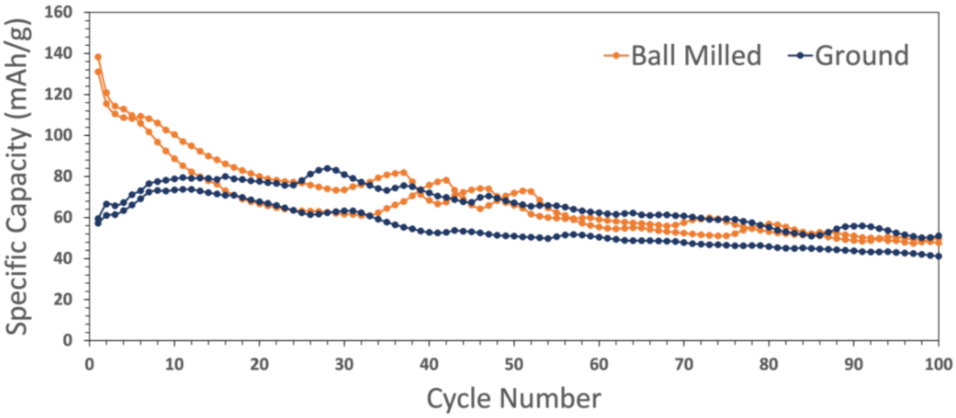

Figure A. 7 Cycling performance of ball milled $Na_{0.7}MnO_2$ and non-ball milled $Na_{0.7}MnO_2$

A.3.4 Binder ($Na_{0.7}MnO_2$)

Several binders were used to evaluate their effect on the cell performance. The active material was ball milled $Na_{0.7}MnO_2$, the conductive agent was carbon black. The binder used were Teflon, PVDF, PVA, PVB and CMC. An electrode without binder was also included in the study, Table A. 1. Capacities versus cycle number are given in Figure A. 8.

Table A. 1 List of slurry compositions with different type of binders

Active Material (A)	**Binder (B)**	**Conductive Agent (C)**	**Weight Ratio A:B:C**
$Na_{0.7}MnO_2$ (Ball milled)	Teflon	Carbon Black	75:5:20
	PVDF	Carbon Black	70:10:20
	PVA	Carbon Black	70:10:20
	PVB	Carbon Black	70:10:20
	CMC	Carbon Black	70:10:20
	-	Carbon Black	80:0:20

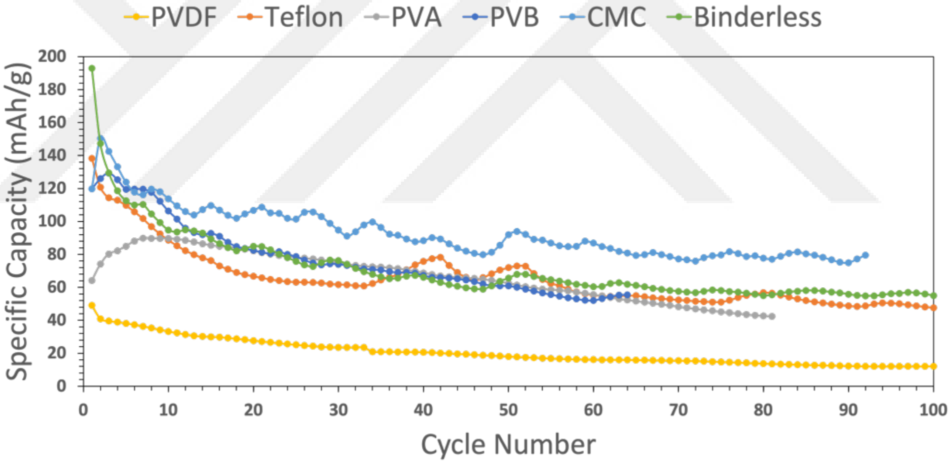

Figure A. 8 Cycling performance of $Na_{0.7}MnO_2$ with different binders and without a binder. Note that batteries tested with using 5 separators

As seen in Figure A. 8, the cathode without binder delivered highest initial capacity. All binders display similar performances except for PVDF with which the capacity is quite low. CMC as binder yield better performance where the capacity is around 80 mAh/g.

A.3.4 Cells with (Bi,Na,Ni,Mn)O_x Cathodes

Cathodes were prepared with conventional slurry making. The locations of the cathode compositions in ternary Bi-Mn-Ni oxides diagram are shown in Figure A. 9 and tabulated in Table A. 2.

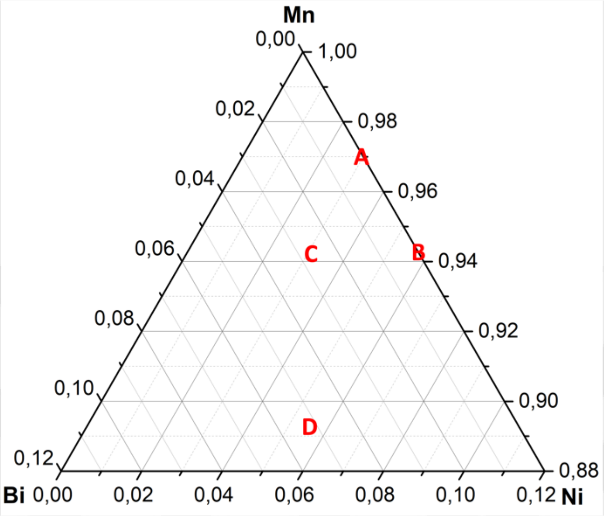

Figure A. 9 Synthesized compositions on Bi-Mn-Ni ternary diagram

Table A. 2 Cathodes prepared with slurry method

Code	**Active Material (A)**	**Binder (B)**	**Conductive Agent (C)**	**Weight Ratio A:B:C**
A	$Na_{0.49}Ni_{0.03}Mn_{0.49}O_x$ (Calcined&ground)	Teflon:CMC	Carbon Black	84:5:1:10
B	$Na_{0.49}Ni_{0.01}Mn_{0.49}O_x$ (Calcined&ground)	Teflon:CMC	Carbon Black	84:5:1:10
C	$Bi_{0.01}Na_{0.49}Ni_{0.01}Mn_{0.49}O_x$ (Calcined&ground)	Teflon:CMC	Carbon Black	84:5:1:10
D	$Bi_{0.03}Na_{0.47}Ni_{0.03}Mn_{0.47}O_x$ (Calcined&ground)	Teflon:CMC	Carbon Black	84:5:1:10
D	$Bi_{0.05}Na_{0.08}Ni_{0.05}Mn_{0.82}O_x$ (Calcined&ground)	Teflon:CMC	Carbon Black	84:5:1:10
D	$Bi_{0.05}Na_{0.08}Ni_{0.05}Mn_{0.82}O_x$ (Ball milled)	Teflon:CMC	Carbon Black	84:5:1:10
D	$Bi_{0.04}Na_{0.25}Ni_{0.04}Mn_{0.67}O_x$ (Ball milled)	Teflon:CMC	Carbon Black	84:5:1:10

The cathodes were in two groups. One group comprising two cathodes were without bismuth, i.e., $Na_{0.49}Ni_{0.03}Mn_{0.49}O_x$ and $Na_{0.49}Ni_{0.01}Mn_{0.49}O_x$. These were prepared using stoichiometric proportions of Na_2CO_3, MnO_2, and NiO which were mixed and calcined at 850℃ for 15 hours. XRD pattern of the samples without Bi are shown in Figure A. 10. Here the cathode is crystalline containing more than one phase.

Slurries were prepared in the ratio of 84:10:1:5 active material, carbon black, CMC and Teflon. Capacities versus cycle number are given in Figure A. 11. It is seen that the capacity which was above 100 mAh/g decreases rapidly down to 50 mAh/g with cycling. The voltage profiles of the cells are given in Figure A. 12.

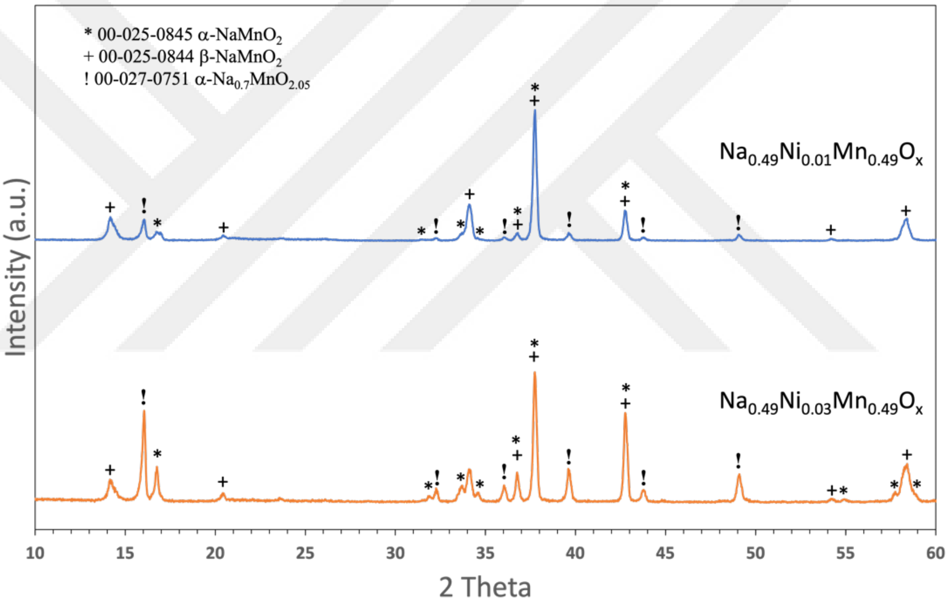

Figure A. 10 XRD patterns of solid state synthesized $(Na,Ni,Mn)O_x$ cathodes

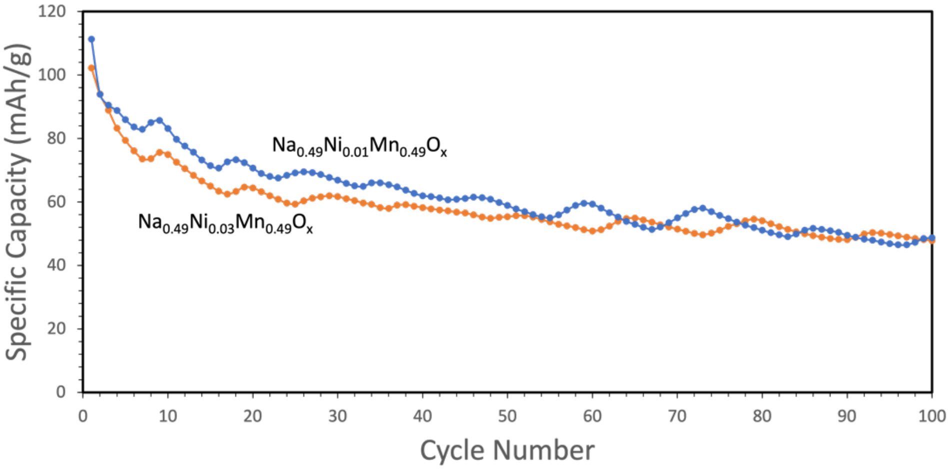

Figure A. 11 Capacity versus cycle number of cells with solid state synthesized (Na,Ni,Mn)O_x cathodes

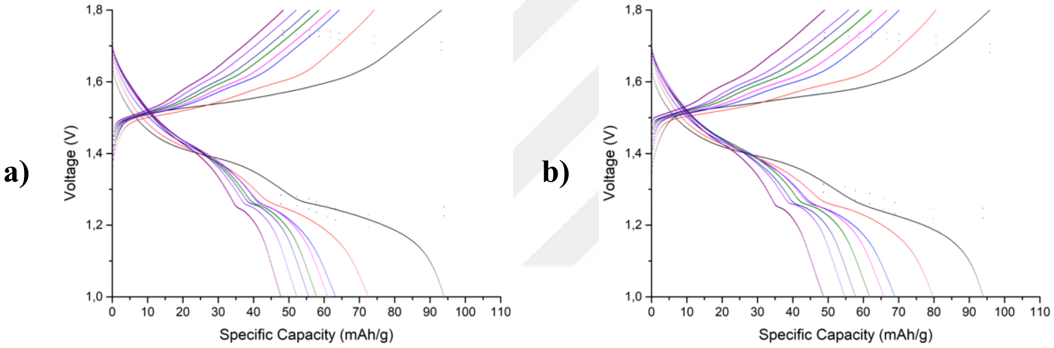

Figure A. 12 Voltage profiles of **a)** $Na_{0.49}Ni_{0.03}Mn_{0.49}O_x$, **b)** $Na_{0.49}Ni_{0.01}Mn_{0.49}O_x$

The other group of samples which contained bismuth were prepared in similar way using Na_2CO_3, MnO_2, Bi_2O_3 and NiO. XRD Pattern of the synthesized powders are given in Figure A. 13. The structure as before contained mixture of phases. In addition, there was unidentified phases due to Bi addition.

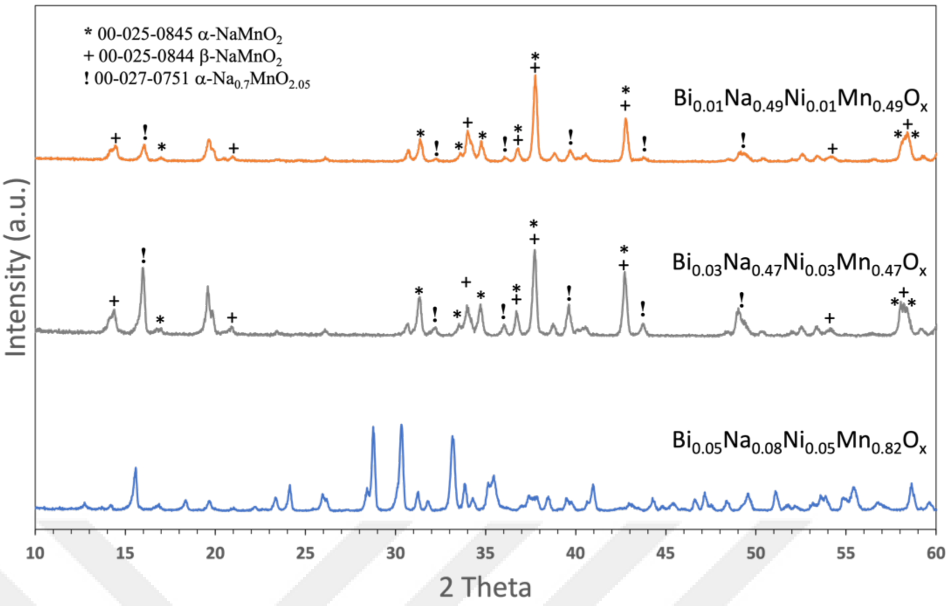

Figure A. 13 XRD patterns of solid state synthesized (Bi,Na,Ni,Mn)O_x cathodes

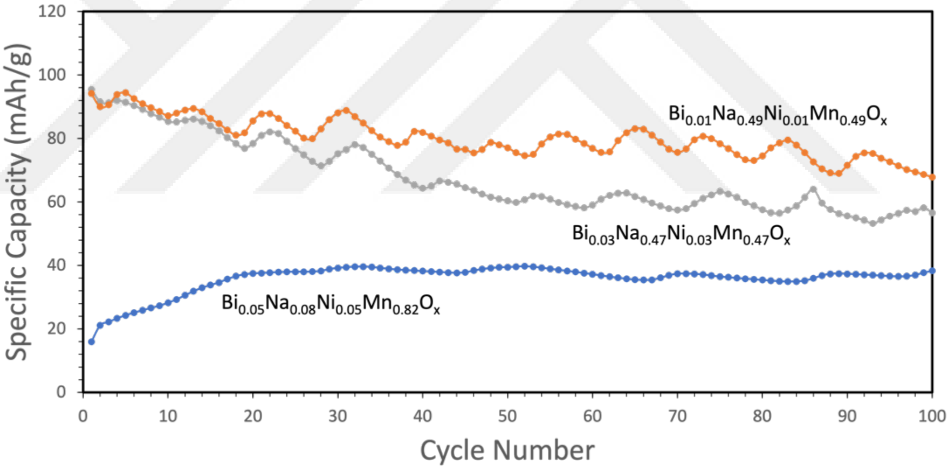

Figure A. 14 Capacity versus cycle number of cells with solid state synthesized (Bi,Na,Ni,Mn)O_x cathodes

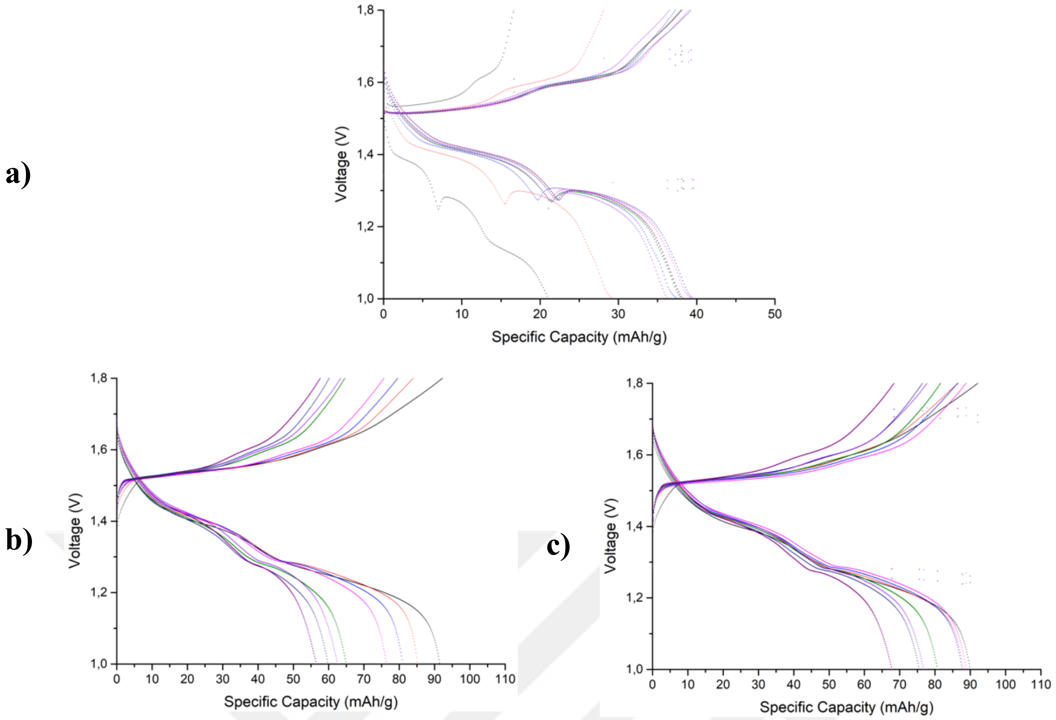

Figure A. 15 Voltage profiles of cells with Bi containing solid state synthesized (Bi, Na,Ni,Mn)O_x cathodes; **a)** $Bi_{0.05}Na_{0.08}Ni_{0.05}Mn_{0.82}O_x$, **b)** $Bi_{0.03}Na_{0.47}Ni_{0.03}Mn_{0.47}O_x$, **c)** $Bi_{0.01}Na_{0.49}Ni_{0.01}Mn_{0.49}O_x$

Capacity versus cycle number of Bi containing cathodes is given in Figure A. 14. It is seen that the capacity varies depending on the composition, but one property which are common to all composition the cells have better cyclic performance. The best cathode is $Bi_{0.03}Na_{0.47}Ni_{0.03}Mn_{0.47}O_x$ which had an initial capacity close to 100 mAh/g. The capacity is quite high with a value close to 70 mAh/g even after 100 cycles. Voltage profile of the cells with Bi containing cathodes are given in Figure A. 15.

So as to prepare a nanocrystalline/amorphous cathode, a separate experiment was carried out using ball milling. As shown in Table A. 2. Two cathodes were prepared which had the compositions of $Bi_{0.05}Na_{0.08}Ni_{0.05}Mn_{0.82}O_2$ and $Bi_{0.04}Na_{0.25}Ni_{0.04}Mn_{0.67}O_2$. These were prepared by mixing Bi_2O_3, NiO MnO_2 and $Na_{0.7}MnO_2$ in stoichiometric proportions and milled for 10 hours.

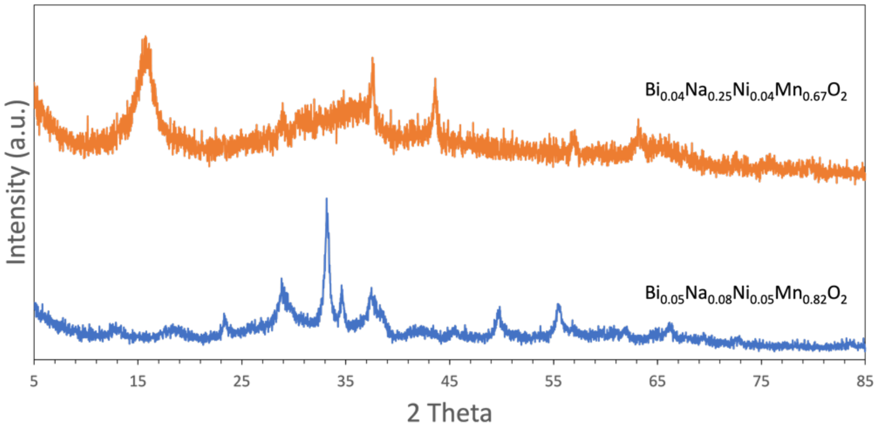

Figure A. 16 XRD pattern of $(Bi,Na,Ni,Mn)O_x$ cathode prepared by ball milling

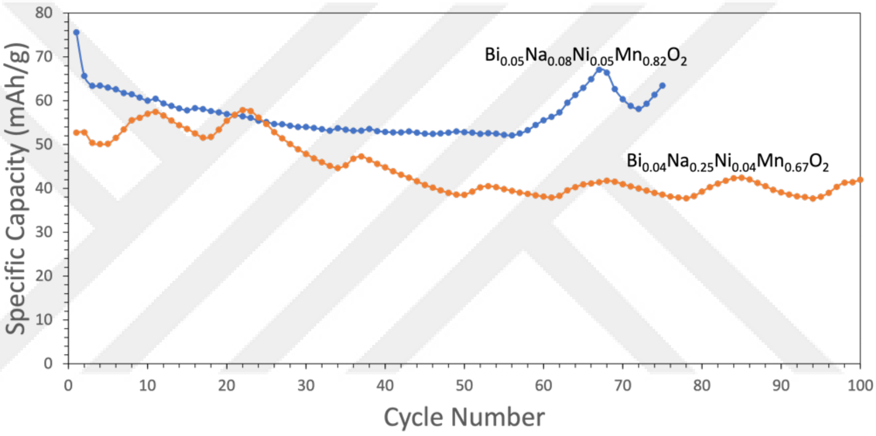

Figure A. 17 Capacity versus cycle number of $(Bi,Na,Ni,Mn)O_x$ cathodes synthesized via ball milling

XRD pattern of the resulting powder, Figure A. 16 were nanocrystalline with broad peaks. Slurries were prepared in ratio of 84:10: 1:5 for active material, carbon black, CMC and Teflon. Capacity versus cycle number of the cells with ball milled cathode are given in Figure A. 17. The capacity retention is quite good but overall level of capacity is not high enough.

A.4. Summary

A study was carried out on (Bi,Na,Ni,Mn)Ox cathodes prepared with slurry method using zinc as anode and 2M $ZnSO_4$+0.1 $MnSO_4$ as electrolyte. The current study has shown that the use of more than one separator, preferably 5, may be needed so as to prevent the short circuit caused by dendritic growth of zinc. As for the additives in cathode, carbon black with 10 or 20 wt.% of the electrode gives similar performance. For binder, CMC added with 10 wt.% of the electrode yielded the best performance as compared to other alternatives PVDF, Teflon, PVA and PVB. Of the compositions studied in this work, best performance was obtained with $Bi_{0.03}Ni_{0.03}NaMnO_x$ with discharge capacity over 70 mAh/g after 100 cycles.

Further work is needed to increase the discharge capacity of the cells using the slurry method.

B. Preparation of Sputter Targets: Fe_2O_3, $NaFeO_2$, Cr_2O_3, CuO, CaO, Mn_3O_4 and TiO_2,

B.1 Powder Synthesis and Target Making

Fe_2O_3

Fe_2O_3 was synthesized from iron nitrate ($Fe(NO_3)_3$, Merck 99%). For this purpose, iron nitrate powders were placed in a crucible and calcined at 725°C for 5 hours in air. In Figure B. 1., XRD pattern shows final powder has both Fe_2O_3 (pdf card no. 01-077-9926, rhombohedral) and Fe_3O_4 (pdf card no. 01-079-0416) phases. Therefore, temperature was increased to eliminate Fe_3O_4 phase. Calcination at 750°C yielded a single phase of Fe_2O_3.

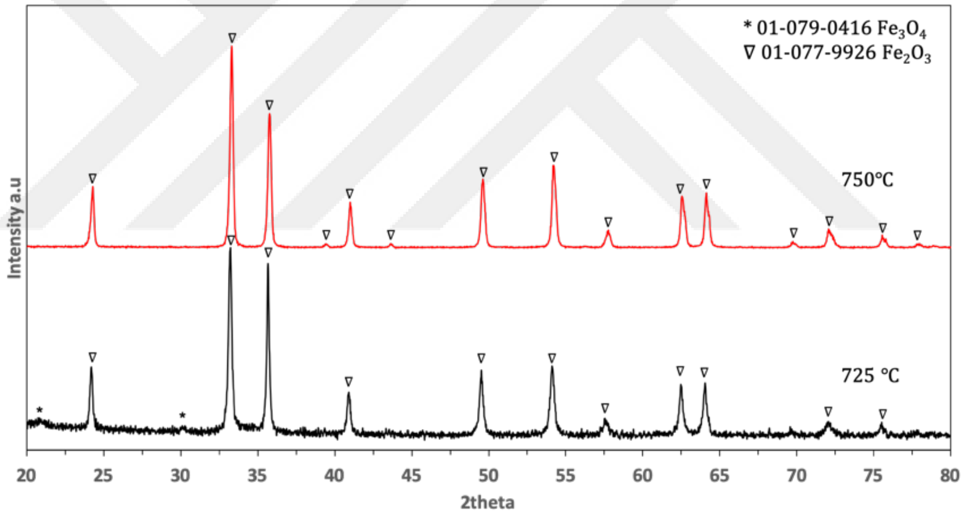

Figure B. 1 XRD pattern of Fe_2O_3 at 725°C and 750°C

Figure B. 2 shows Rietvelt analysis and SEM image of the as-synthesized powder of Fe_2O_3. Analysis showed Fe_2O_3 has cell parameters of a=5.034 Å, c=13.738 Å. SEM images showed that final powder has particle size of few micrometers.

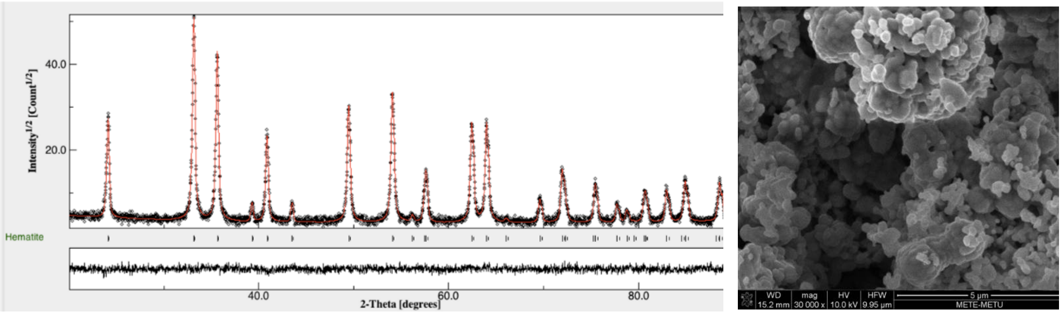

a) **b)**

Figure B. 2 Synthesized Fe_2O_3 powder at 750°C for 5 hours **a)** Rietvelt analysis of the powder **b)** SEM image.

As-synthesized Fe_2O_3 powders were pressed in the 20 mm Teflon rings. Green bodies were sintered at 1250°C for 5 and 15 hours in air. In Figure B. 3 (a) and (b) show the SEM images of sintered samples. There were small pores through the sample, therefore another sintering was made at 1350°C for 15 hours in air, Figure B. 3 (c). At higher temperature, pores were smaller and as a result the target were prepared with these parameters.

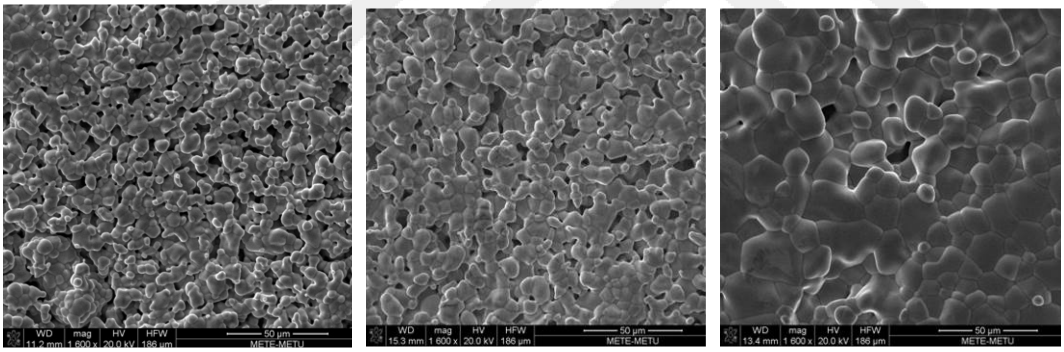

a) **b)** **c)**

Figure B. 3 SEM images of pressed at 100 MPa and sintered Fe_2O_3 (20 mm pellets) at **a)** 1250 °C 5 hours, **b)** 1250 °C for 15 hours and **c)** 1350 °C for 15 hours

Rietvelt refined XRD pattern of sintered sputter target is given in Figure B. 4. Rietveld refinement yielded cell parameters are a=5.034 Å , c=13.738 Å. Photograph of the target is given in Figure 3.4.14

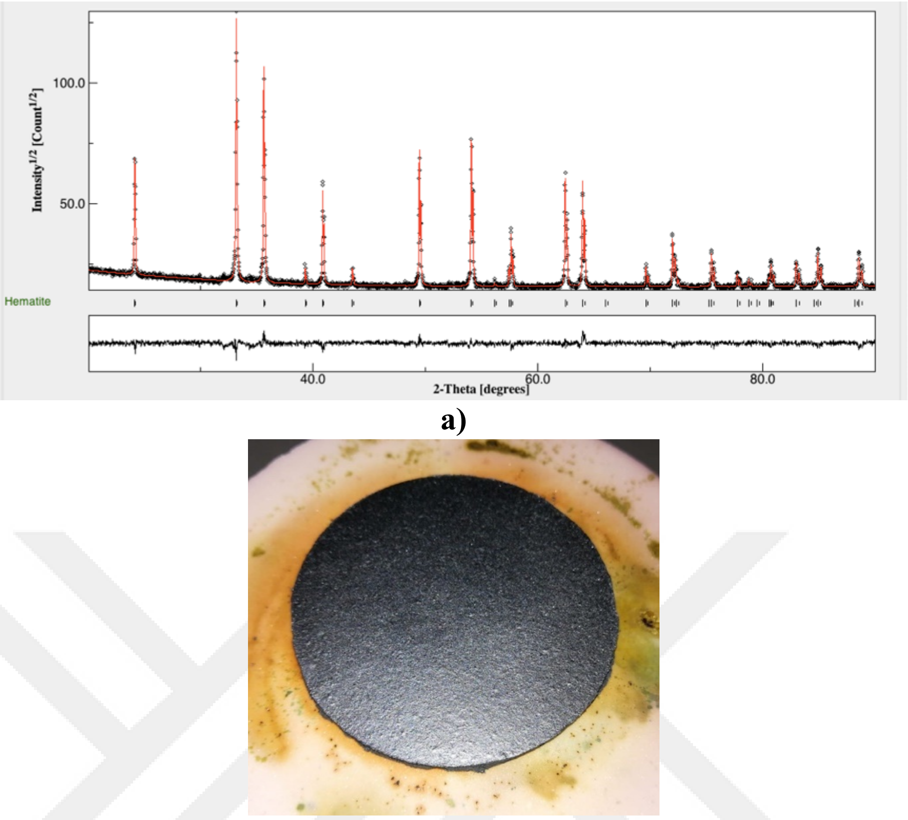

a)

b)

Figure B. 4 Sintered Fe_2O_3 target **a)** Rietvelt refined XRD pattern and **b)** the target

$NaFeO_2$

$NaFeO_2$ was synthesized using stoichiometric mixture of 0.02 mol Fe_2O_3 and 0.02 mol Na_2CO_3. In addition, two more experiments were conducted with 10% and 20% excess Na_2CO_3 to compensate for Na losses. Raw materials were ball milled at 120 rpm for 6 hours. Ball milled powders were calcined at 950℃ for 5 hours under air., XRD pattern of the final product is given in Figure B. 5. Their pattern is consistent with $NaFeO_2$ (pdf card no. 01-074-1351, Orthorhombic). Only the sample with 20% excess Na_2CO_3 has an additional peak at 30° (shown with a star). SEM images of the synthesized powder is given in Figure B. 6. It is seen that the structure is made up of powders with a particle size of 5μm. EDS analysis from as-synthesis powders have Na:Fe ratio as 70:30, 60:40 and 57:43 for stoichiometric, 10% excess and 20% excess samples respectively This implies that there was more Na loss during sintering process. Therefore, composition with 10% excess Na_2CO_3 were selected for sintering of $NaFeO_2$ powder.

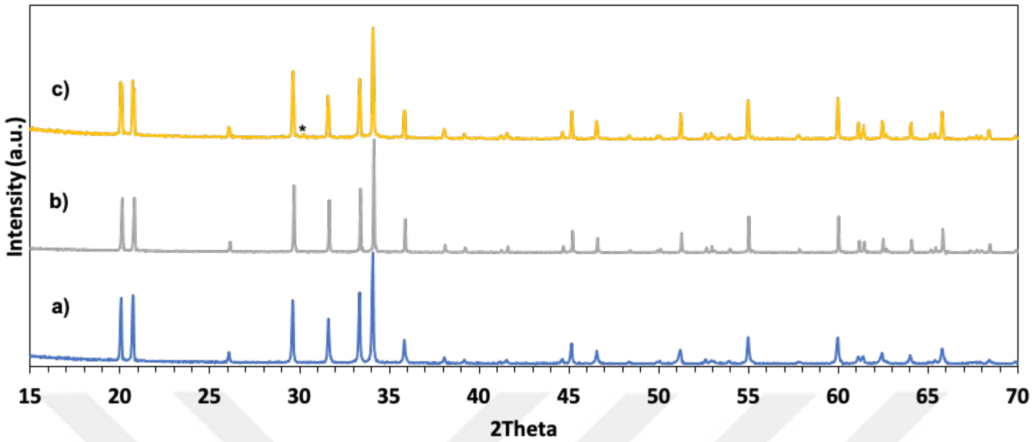

Figure B. 5 XRD pattern of synthesized powders **a)** stoichiometric, **b)** 10% excess, **c)** 20% excess

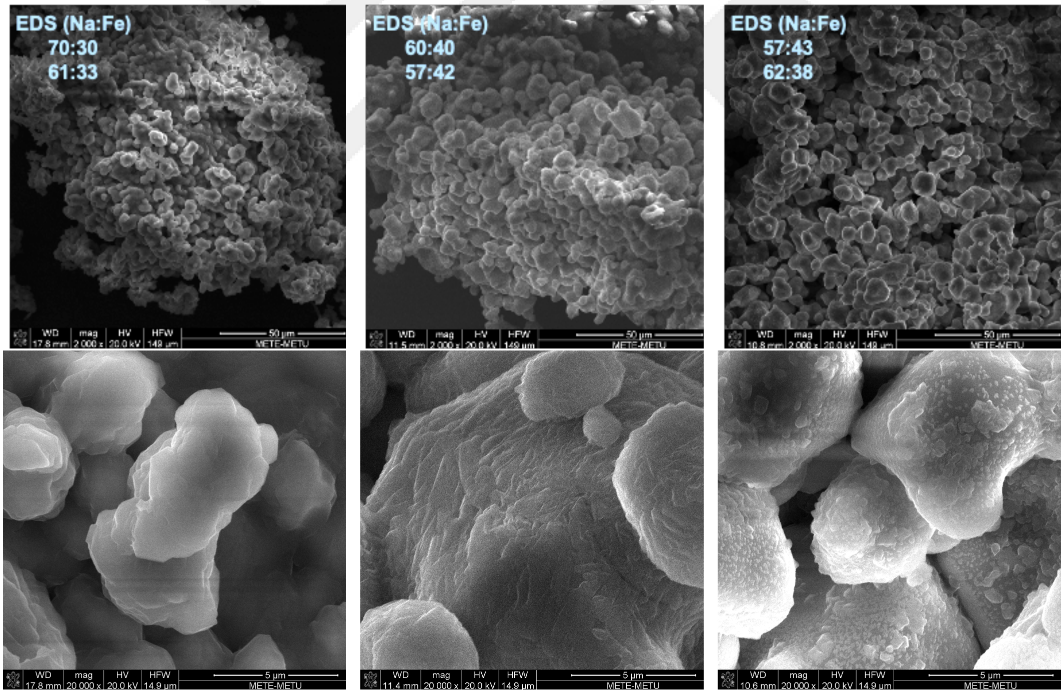

a) **b)** **c)**

Figure B. 6 SEM images and EDS results of synthesized powders **a)** stoichiometric, **b)** 10% excess, **c)** 20% excess

So as to produce the sputter target, As-synthesized powders were mixed with DI water. Then, pressed under 100 MPa in a Teflon ring. Green bodies were first heated to 120°C with 1°/min. Then, waited at 120 for 1 hour to eliminate humidity. Finally, sintered at 1350°C , XRD pattern of sintered $NaFeO_2$ for 5, 10, 15 hours were given in Figure B. 7. Na_2FeO_4 was found as an impurity in the sample with 20% excess Na_2CO_3. Stoichiometric and 10% excess sample formed as orthorhombic $NaFeO_2$ phase., The microstructure of sintered $NaFeO_2$ was given in Figure B. 8. As Na content increased, the compaction was more efficient. Cell parameters as derived from Rietvelt refined XRD pattern are given Table B. 1.

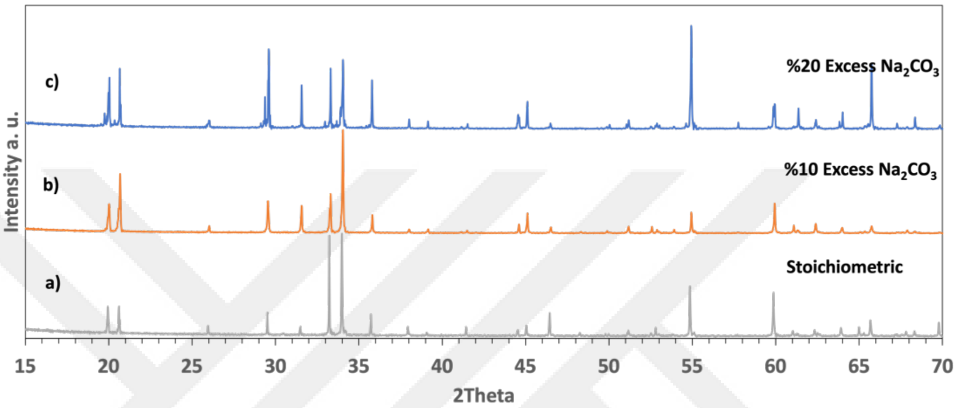

Figure B. 7 XRD pattern of sintered $NaFeO_2$ pellets at 1350°C for 5 hours

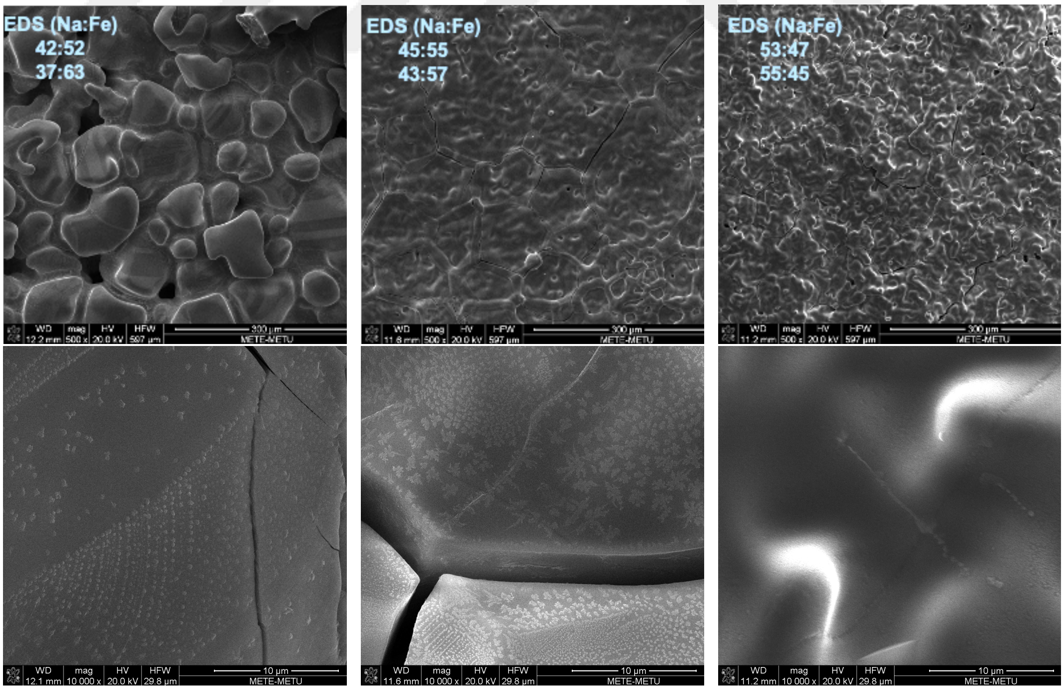

a) b) c)

Figure B. 8 SEM images of sintered $NaFeO_2$ at 1350 for 5 hours **a)** stoichiometric, **b)** 10% excess, **c)** 20% excess

Table B. 1 Lattice parameters of $NaFeO_2$ with different Na content from Rietvelt refinement

Composition	a (Å)	b (Å)	c (Å)	Crystal Size (nm)	Rwp (%)
Stoichiometric	5.67	7.14	5.38	2576 ±29	11.24
10% Excess	5.68	7.15	5.39	2708 ±65	14.47
20% Excess	5.63	7.08	5.34	6945±66	28.11

Synthesized powders are not stable in air. Powders decomposed to NaO_2 (pdf card no. 00-006-0500) and Fe_2O_3 phases. Therefore, powders and the target were stored in Ar filled glovebox to prevent from air and humidity.

Cr_2O_3

Chromium (II) nitrate nonahydrate ($Cr(NO_3)_3.9H_2O$, Merck 98%) were used to synthesize pure Cr_2O_3. Chromium nitrate powders were calcined at 700°C for 4 hours in air. XRD pattern of synthesized powder is shown in Figure B. 9. It matches a single phase of Cr_2O_3 (pdf card no. 00-038-1479).

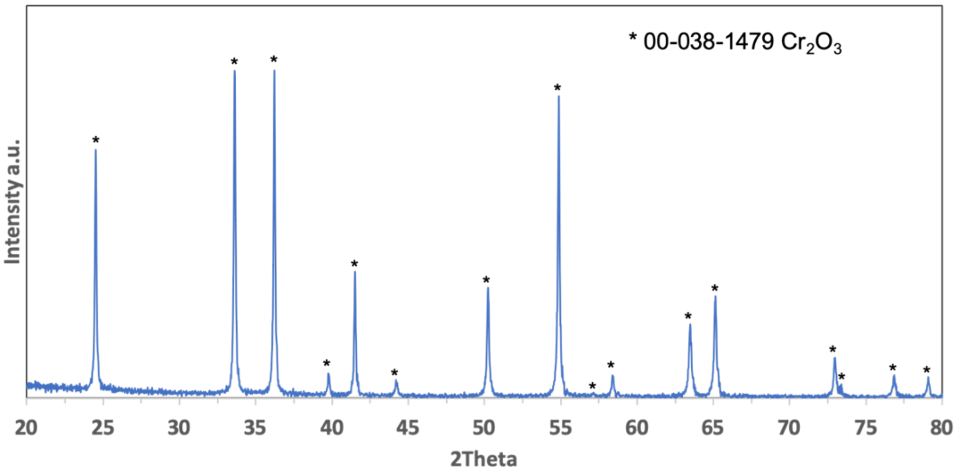

Figure B. 9 XRD pattern of Cr_2O_3 calcined at 700°C for 4 hours.

Rietvelt refined pattern is given in Figure B. 10 (a) which yields cell parameters of a=4.968 Å, c=13.619 Å . SEM image of the as-synthesized powder is given. In Figure B. 10 (b) where particles are few micrometers in size.

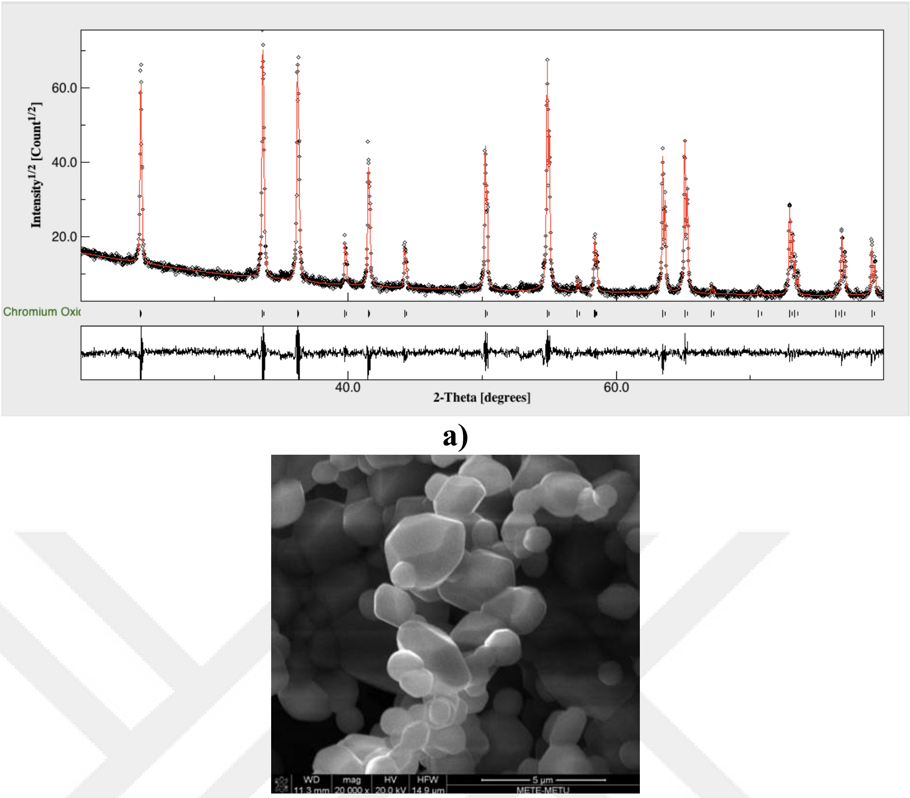

a)

b)

Figure B. 10 Cr_2O_3 powder synthesized at 700°C for 4 hours **a)** Rietvelt refined XRD pattern and **b)** SEM image of the synthesized the powder

So as to fabricate sputter target, as-synthesized Cr_2O_3 powders were mixed with few drops of DI water and pressed under 100 MPa in 20 mm Teflon ring. First, pellets were sintered at 1350°C for 5, 10 and 15 hours in air. The resulting microstructure had a bunch of large pores and thus sample was not dense enough. Therefore, new sintering process was carried out at 1450°C and 1550°C for 15 hours, see Figure B. 11. 1550°C was barely enough to yield a sputter target with acceptable properties. Rietveld refined XRD pattern, Figure B. 12, yielded a=4.968Å, c=13.619 Å.

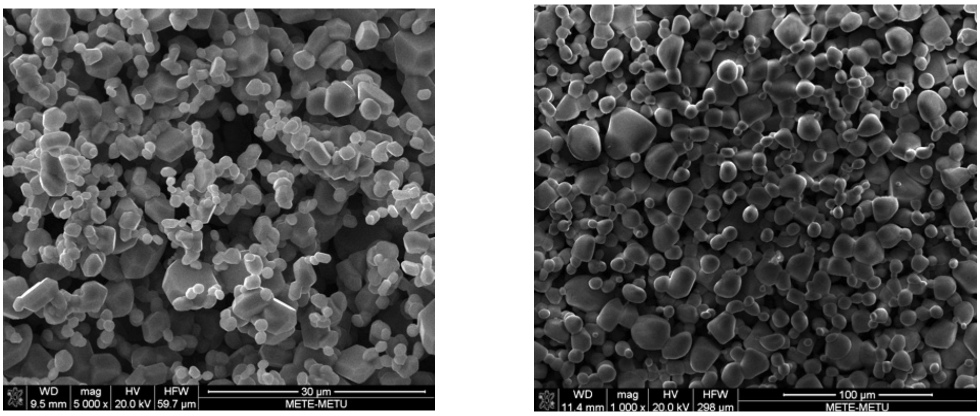

a) **b)**

Figure B. 11 SEM image of sintered Cr_2O_3 in air **a)** 1450 °C for 15 hours, **b)** 1550 °C for 15 hours

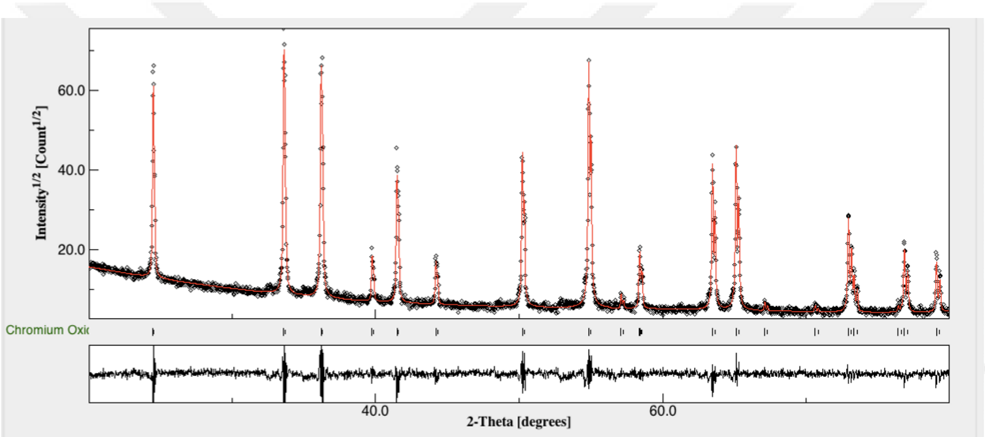

Figure B. 12 Rietvelt refined XRD pattern of sintered Cr_2O_3 at 1550 °C for 15 hours in air

CuO

Copper (II) sulfate pentahydrate ($CuSO_4 \cdot 5H_2O$, Merck 99%) were used to synthesize CuO. Copper sulfate was calcined at 700°C for 5 hours in air. Figure B. 13 shows the XRD pattern of synthesized CuO. The pattern is consistent with monoclinic CuO (pdf card no. 01-073-6023).

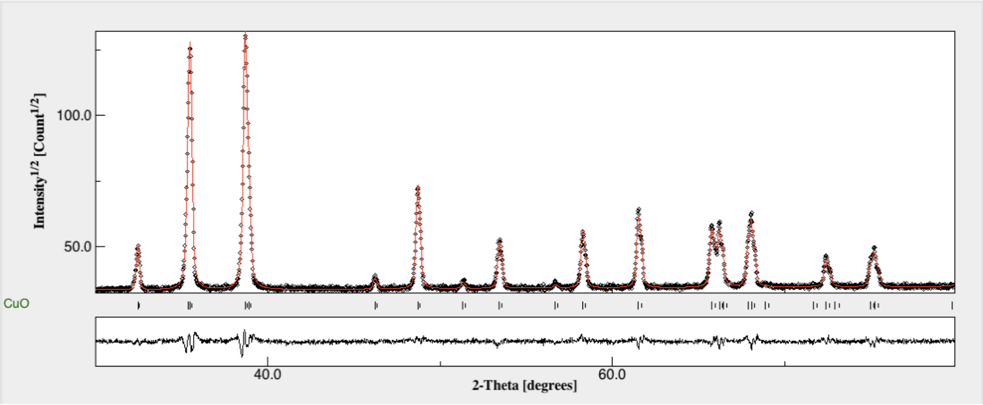

Figure B. 13 Rietvelt refined XRD pattern of as-synthesized CuO powder at 700°C for 5 hours

Rietvelt analysis of the as-synthesized powder yielded cell parameters of a= 4.688 Å, b= 3.426 Å, c=5.134 Å. SEM images showed that the powders were a few micrometers in size with agglomerates as 10-12 μm, Figure B. 14.

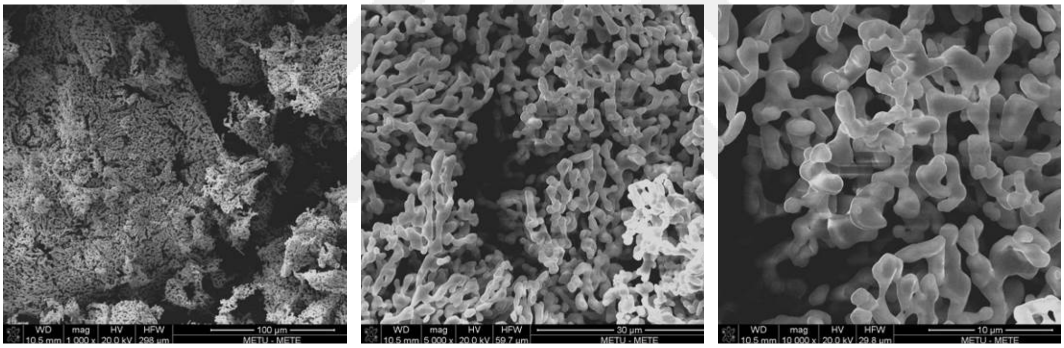

a) **b)** **c)**

Figure B. 14 SEM image of as-synthesized CuO **a)**1000x, **b)** 5000x, **c)** 10000x

To fabricate sputter target CuO powders were pressed under 100 MPa. Green bodies were sintered at 1000°C, 1100°C and 1200°C for 10 hours in air. At 1200°C was however too high which resulted in melting of the sample. XRD patterns of powders synthesized at 1000°C, 1100°C are shown in Figure B. 15. The patterns were made up of two phases Cu_2O (pdf card no. 01-071-3645) and CuO (pdf card no. 01-073-6023, monoclinic). SEM images of synthesized targets are given in Figure B. 16. Rietveld refined pattern, at 1000°C, yielded a=4.699 Å, b=3.445 Å, c=5.137 Å for the major phase CuO. It should be pointed out that the mass fraction of Cu_2O was only

0.53 wt.% in this sample. Accordingly target sintered at 1000℃ may be considered as single phase CuO.

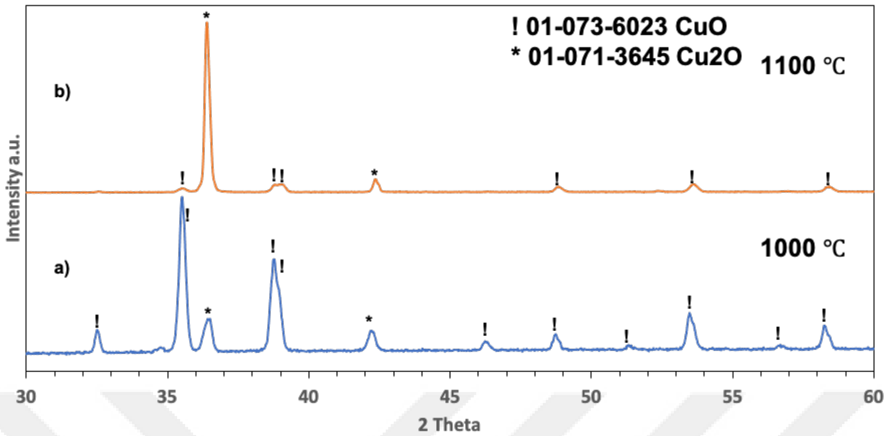

Figure B. 15 XRD pattern of sintered CuO at **a)** 1000℃, **b)** 1100℃

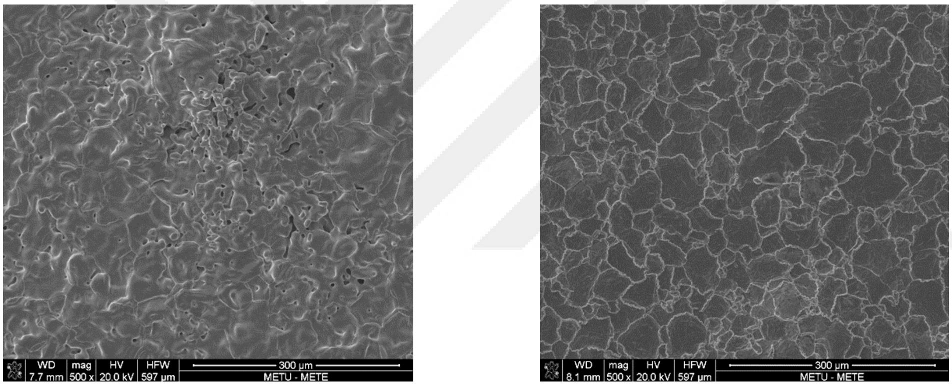

a) **b)**

Figure B. 16 SEM images of sintered CuO at **a)** 1000℃, **b)** 1100℃

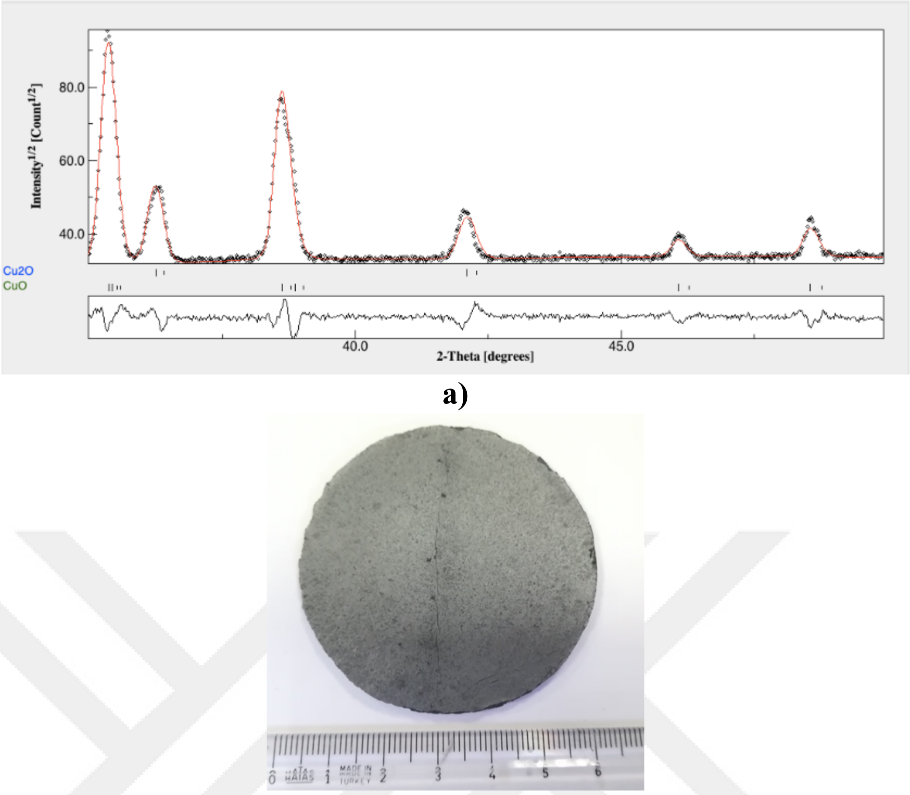

a)

b)

Figure B. 17 CuO target sintered at 1000°C for 10 hours **a)** Rietvelt refined XRD pattern and **b)** sintered CuO target.

CaO

To synthesize CaO, $CaCO_3$ (Sigma-Aldrich, 98.5%) were calcined at 900°C for 5 hours in air. XRD pattern of the resulting powder, in Figure B. 18 (a), matched with cubic CaO (pdf card no. 01-070-4068). Rietvelt refined pattern yielded a cell parameter of a= 4.809 Å. SEM image of the synthesized powder is given in Figure B. 18 (b).

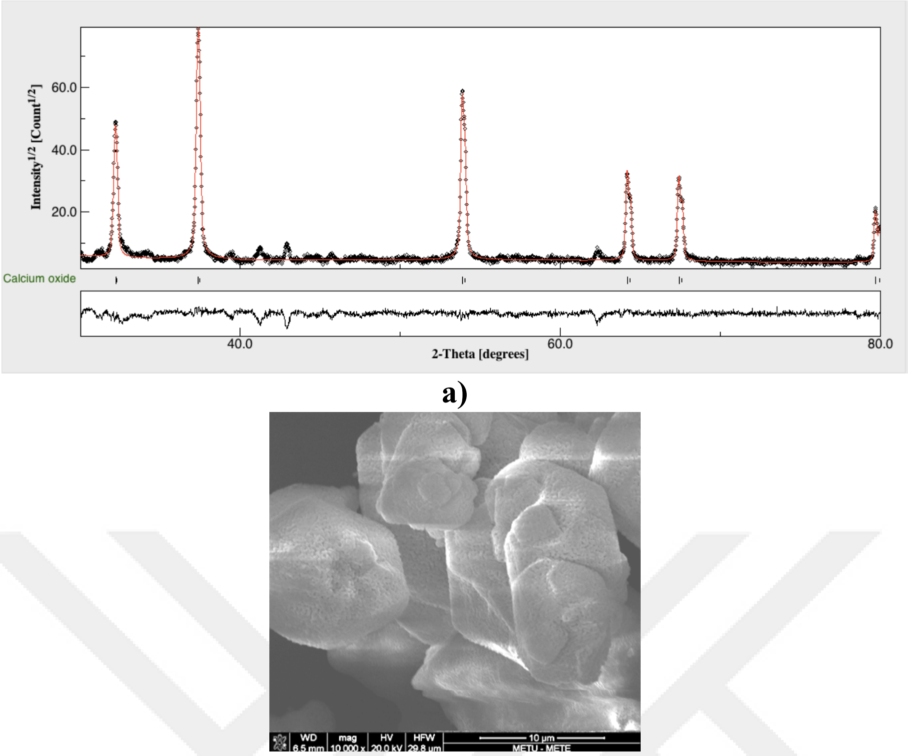

a)

b)

Figure B. 18 CaO powder synthesized at 900℃ for 5 hours **a)** Rietvelt refined XRD pattern and **b)** SEM image of the synthesized the powder

To fabricate sputter target as-synthesized CaO powders were pressed under 100 MPa in 20 mm Teflon rings. Green bodies were sintered at 1000℃, 1100℃ and 1200℃ for 10 hours in air. SEM images of the sintered pellets were given in Figure B. 19. Best densification was obtained at 1200℃. In Figure B. 20, Rietvelt refined pattern at 1200℃ has yielded a=4.809 Å. A photograph of CaO sputter target is given. Figure B. 19. (b)

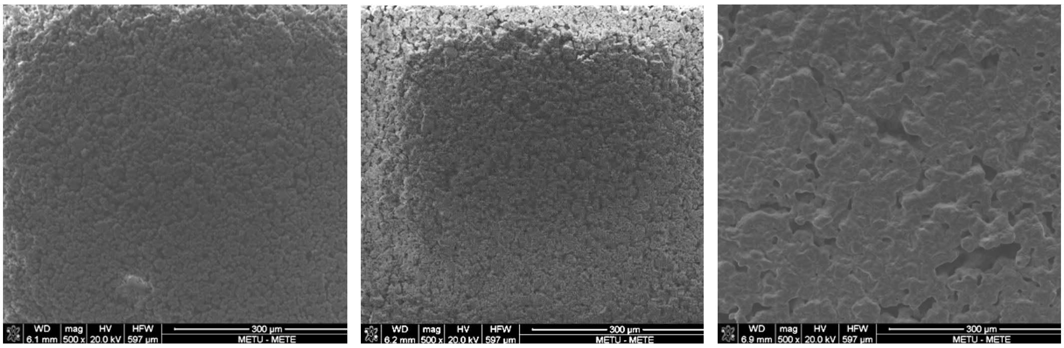

a) **b)** **c)**

Figure B. 19 SEM image of sintered CaO at **a)** 1000℃, **b)** 1100℃, and **c)** 1200℃

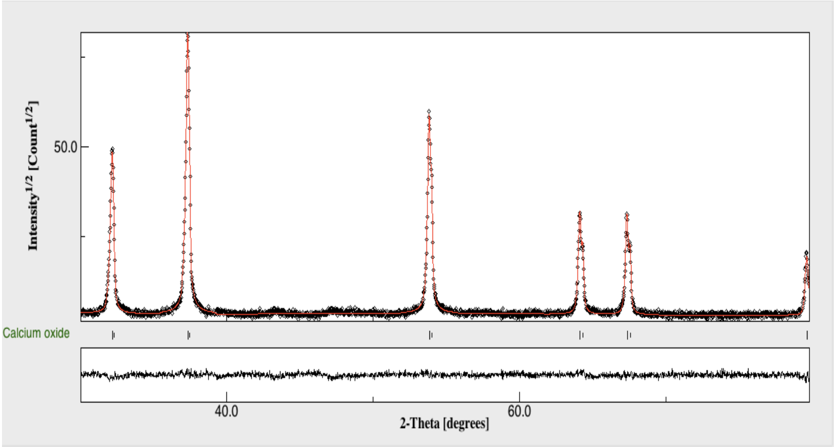

a)

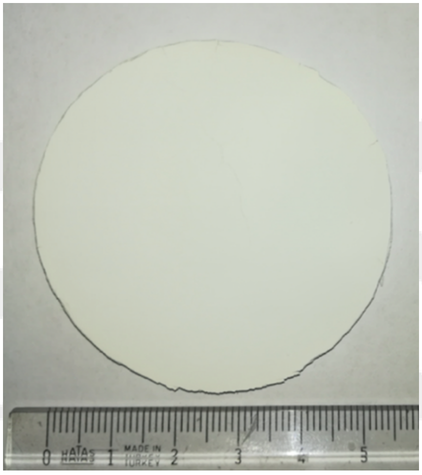

b)

Figure B. 20 Sintered at 1200°C for 10 hours CaO target **a)** Rietvelt refined XRD pattern and **b)** 2-inch CaO target

Mn_3O_4

To fabricate Mn_3O_4 sputter target, MnO_2 (Alfa Aesar, 98%) powder was used directly. They were mixed with few drops of DI water. Then the mixture was pressed in a Teflon ring with 100 MPa pressure. Green body was sintered at 1250°C for 5 hours., XRD pattern of the resulting powder is given in Figure B. 21. The pattern is consistent with Mn_3O_4 (pdf card no. 01-080-0382). The microstructure as shown in Figure B. 21.(b), was not, however, fully dense. Still, it was sufficiently strong to be used as sputter target Figure B. 22.

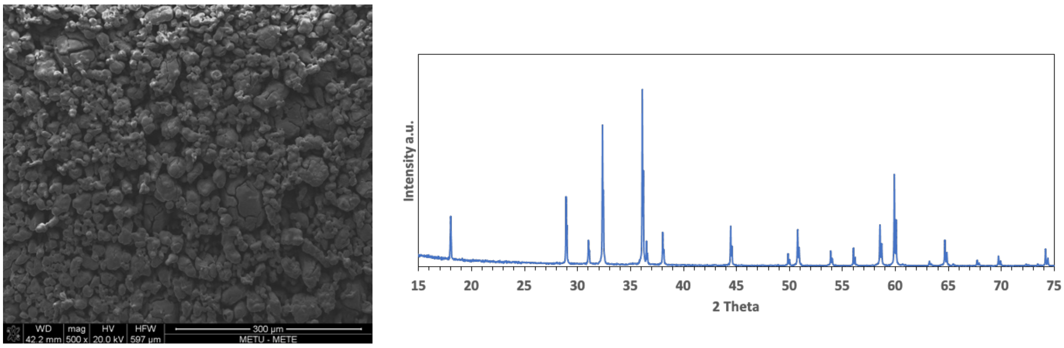

a) **b)**

Figure B. 21 Sintered Mn_3O_4 at 1250 °C for 5 hours **a)** SEM image, **b)** XRD pattern

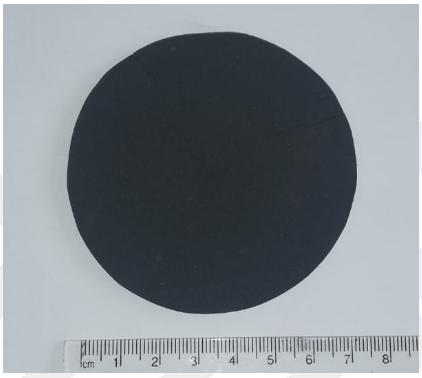

a)

Figure B. 22 Photograph of 3-inch Mn_3O_4 target

TiO_2 Target

To fabricate TiO_2 sputter target TiO_2 (Alfa Aesar, 99.8%) powder were used. The powder was pressed under 100 MPa in Teflon rings with 20 mm diameters. Then, green bodies were sintered at 1300°C, 1400°C and 1500°C for 5, 10 and 15 hours in air. However, the pressing 2-inch diameter target under 100 MPa created small cracks that has grown into larger cracks at the end of the sintering process. Therefore, pressure was decreased to 75 MPa. No phase change was seen after sintering process, (pdf card no. 03-065-0191, tetragonal), Figure B. 23. Sample sintered at 1500°C had the densest structure, Figure B. 25. Therefore, the TiO_2 target was fabricated by compacting 75 MPa pressure and sintering at 1500°C for 15 hours in air. Rietvelt refined XRD pattern yielded rutile TiO_2 has with cell parameters as TiO_2 a=4.589 Å, b=4.597 Å, c=2.963 Å and α=89.886 , β=89.881, γ=90.145, Figure B. 24.

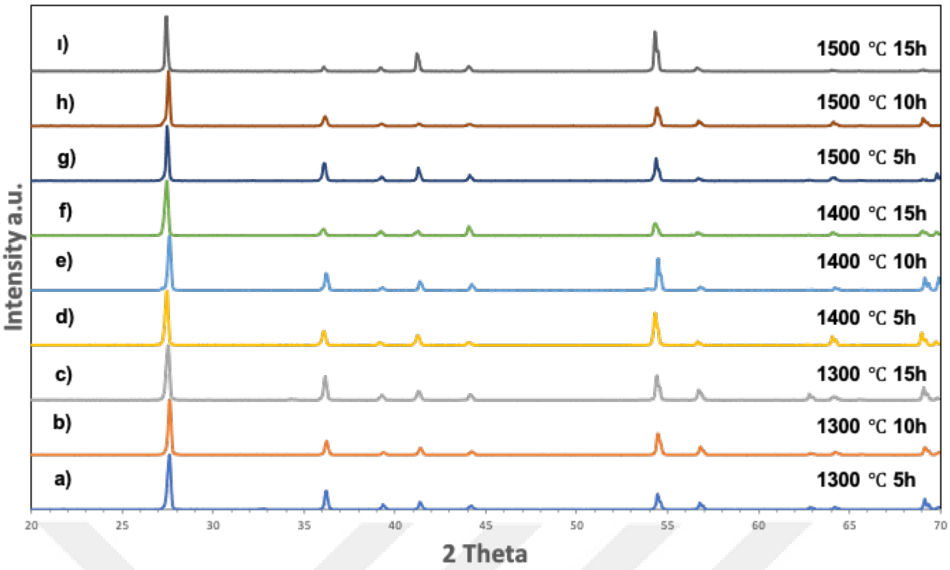

Figure B. 23 XRD pattern of sintered TiO_2 targets at 1300°C for **a)** 5h, **b)** 10h, **c)** 15h, 1400°C for **d)** 5h, **e)** 10h, **f)** 15h, 1500°C for **g)** 5h, **h)** 10h, **i)** 15h

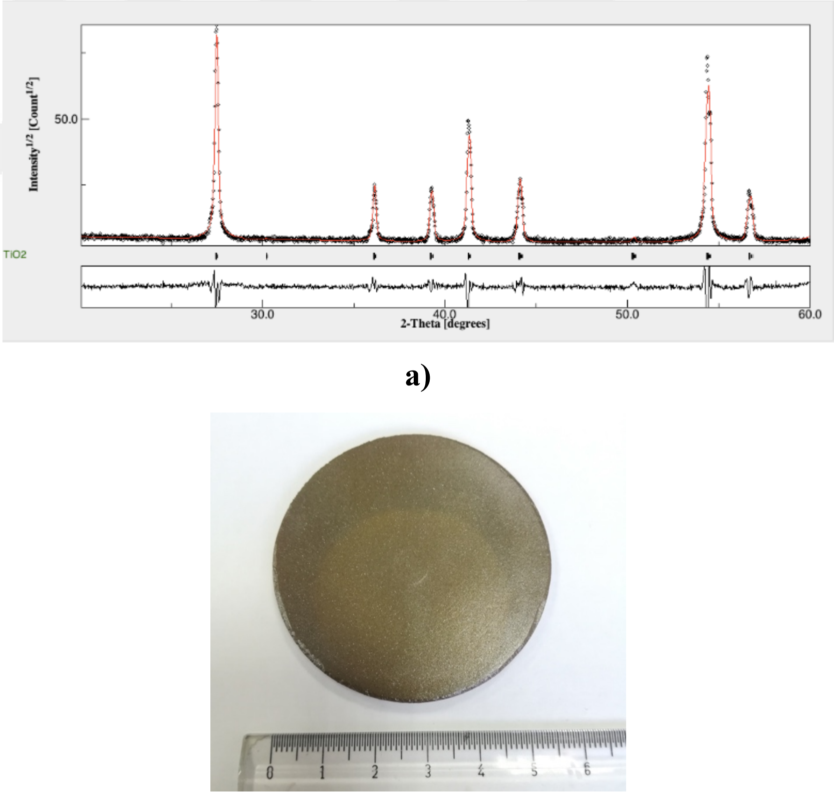

a)

b)

Figure B. 24 TiO_2 target sintered at 1500°C for 15 hours **a)** Rietvelt refined XRD pattern and **b)** TiO_2 target

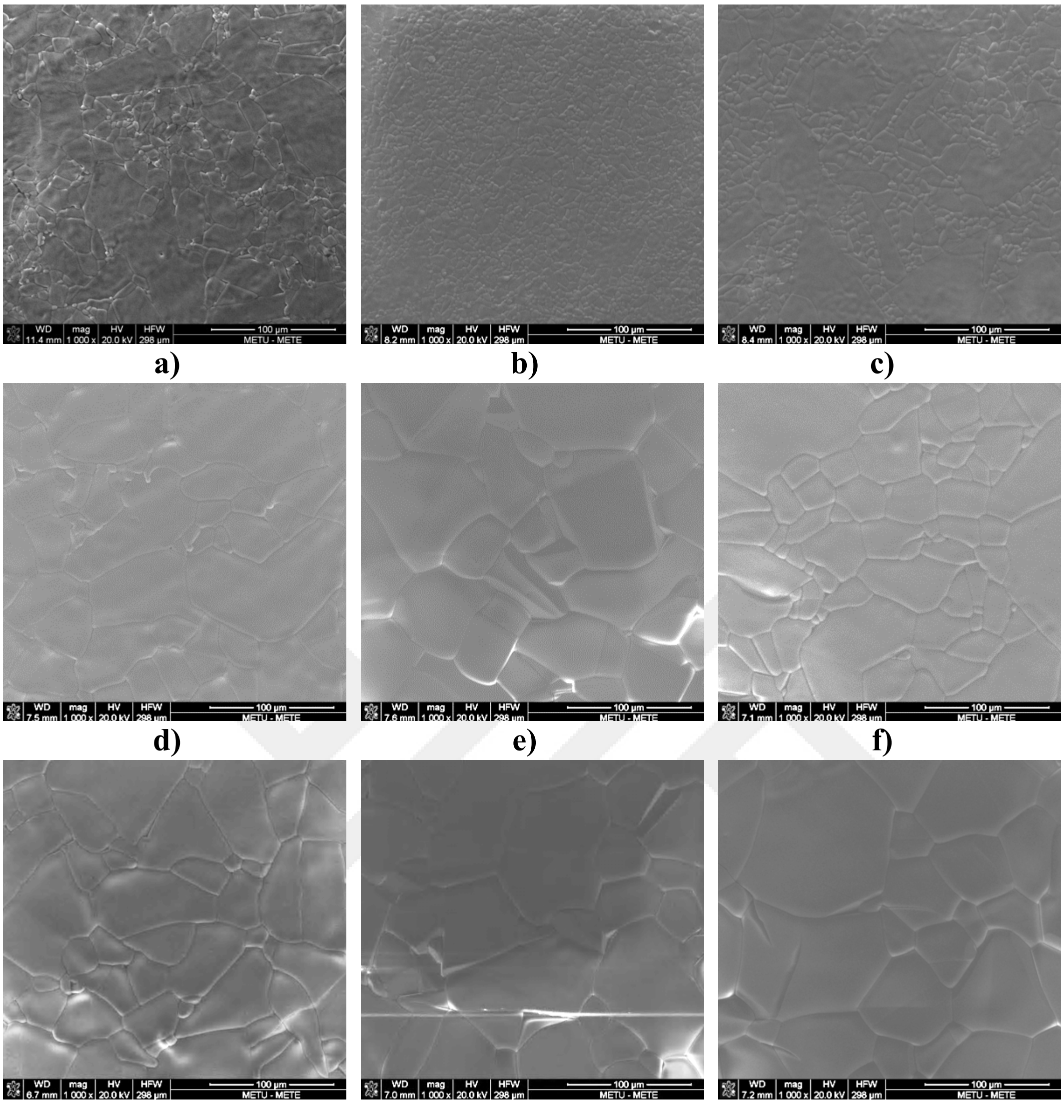

a) b) c)

d) e) f)

g) h) i)

Figure B. 25 SEM images of sintered TiO$_2$ targets at 1300°C for **a)** 5h, **b)** 10h, **c)** 15h, 1400°C for **d)** 5h, **e)** 10h, **f)** 15h, 1500°C for **g)** 5h, **h)** 10h, **i)** 15h, (all with magnification of 1000x)